Master Thesis

A Study of Space Borne Radar Altimetry to Estimate Sea Ice Thickness and Extent

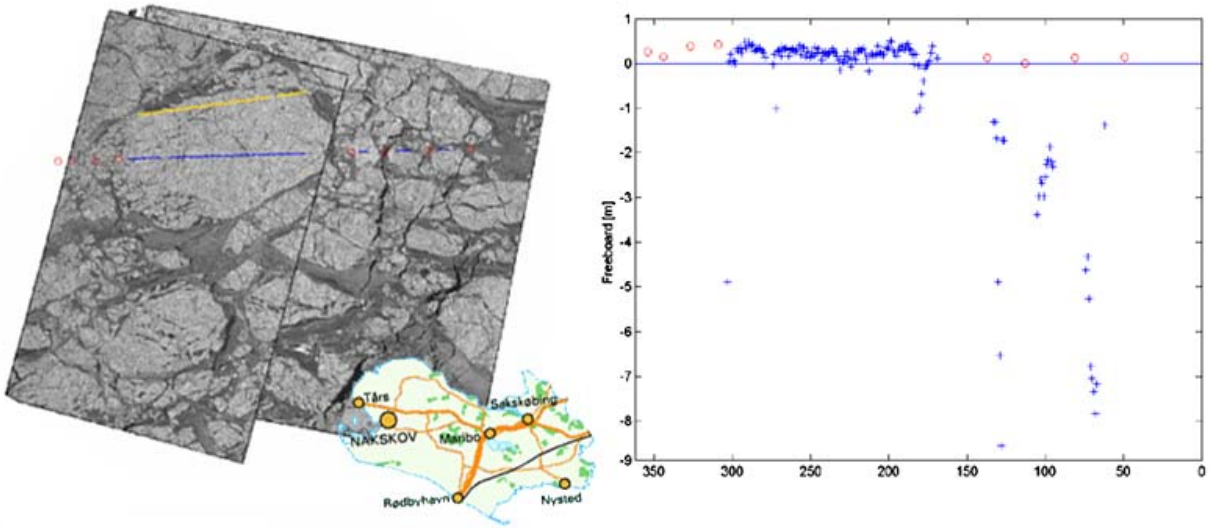

Henriette Skourup

The Department of Geophysics,
University of Copenhagen
March 2004

Supervisors: C.C. Tscherning and R. Forsberg

Preface

This project is my Master Thesis written as a result of my studies at the Niels Bohr Institute of Astronomy, Physics and Geophysics (NBIfAFG), University of Copenhagen. I was inspired by my student job during the past six years at the Danish Meteorological Institute (DMI), where I have become an experienced ice analyst. The major task for an ice analyst is to detect the sea ice extent through thorough interpretation and analysis of remote sensing images. I have gained knowledge of the advantages and limitations of images detected by Synthetic Aperture Radar (SAR), visible and infrared radiometry (AVHRR) and passive microwave radiometry (SSM/I). This project has given me a great opportunity to investigate the potentials of another remote sensing sensor with the purpose of detecting sea ice; the radar altimeter.

Henriette Skourup
30th March 2004

Cover: The image to the left is a SAR image illustrating a large ice floe of approximate dimensions 30x60 km at the same scale as the danish Island called Lolland. The image to the right shows the freeboard of the ice floe.

Acknowledgement

I am very grateful to all the people who have been involved in the process both professionally and in private.

In particular, I give my most devoted thanks to my supervisors C.C. Tscherning and Rene Forsberg for support and inspiration; Rasmus T. Tonboe for assistance and cooperative work with the theoretical model; Henning Hundahl and Niels-Flemming Carlsen for help with the transponder; Sine M. Hvidegaard for sharing knowledge and encouragement; Mads H. Ribergaard for contributing to programming in MATLAB; Jette Miller for proof reading.

I want to thank European Space Agency, especially Pierre Féménias, Jerome Benvenieste and Nicolas Picot, for providing me with altimeter data from ENVISAT; The Danish Meteorological Institute for providing me with Radarsat SAR, ENVISAT ASAR and NOAA images; The National Survey and Cadastre, Denmark, for access to the most recent arctic geoid model and photographies of the sea ice taken during an underflight in northeast Greenland.

Furthermore, I want to thank my dearest friends Torben S. Thomsen, Jaqueline K. Jensen, Thorkild D. Brogaard and Hanne H. Ribergaard for support and tolerance during the process; Keld Q. Hansen for having faith in me, never doubting me to finish my work; and my beloved sister Charlotte Skourup who, despite the long distance, have managed to inspire me not only during the writing of the thesis but during my whole life.

Abstract

This master thesis investigates space borne radar altimetry in order to estimate the sea ice conditions and the sea ice thickness in the Fram Strait and Greenland Sea. The altimeter measures the range of the satellite above the surface and records the shape of the return signal of one pulse, known as the waveform.

The response of the waveforms on different surfaces, for example open ocean and different sea ice covers can be explained by simple considerations of scattering theory. In this study the backscatter coefficient, the peak power and the pulse peakiness have been extracted from the waveform and the variations in these parameters are used to analyze the sea ice conditions. The ice analysis is based on ENVISAT radar altimetry data and validated by NOAA images.

The sea ice freeboard is determined from altimetry measurement of the range and by implementation of a geoid model to approximate mean sea level. In the analysis the sea ice thickness is estimated over a large ice floe of approximate dimensions 30x60 km located in the Fram Strait. The ice thicknesses observed are within reasonable scales and characteristic for first year ice floes (<2 m).

Resume

Dette speciale undersøger mulighederne for at anvende satellitbaseret radar altimetri til bestemmelse af havisens udbredelse og tykkelse. Altimeteret måler afstanden fra satellitten til overfladen samt formen af den reflekterede puls, kaldet pulsformen.

Pulsformens respons på forskellige overfladeforhold, f.eks. åbent hav og områder dækket af havis, forklares via simple betragtninger af spredningsteori. Isforholdene undersøges ved hjælp af backscatter koefficienten, den maksimale effekt af pulsformen samt en parameter der beskriver formen af retur signalet. Til analysen er anvendt data fra ENVISAT's radar altimeter og resultaterne sammenholdes med isobservationer baseret på tolkning af NOAA billeder.

Metoden til at bestemme fribordet af havisen og dermed tykkelsen, er baseret på afstanden målt af altimeteret og en geoide model, der antages at approksimere middel havniveauet. Metoden anvendes til at estimere tykkelsen af en stor isflage på størrelse med Lolland (∼30x60 km) lokaliseret i Fram Strædet nordøst for Grønland. De observerede istykkelser holder sig indenfor en rimelig størrelse svarerende til en isflage bestående af første års is (<2 m).

Abbreviations

ASAR	Advanced Synthetic Aperture Radar
AVHRR	Advanced Very High Resolution Radiometer
CRREL	Cold Region Research and Engineering Laboratory
CSA	Canadian Space Agency
DMI	The Danish Meteorological Institute
ENVISAT	ENVIronmental SATellite
ESA	European Space Agency
F-PAC	French Processing and Archive Center
GLAS	Geoscience Laser Altimeter System
GPS	Global Positioning System
HSRRA	High Spatial Resolution Radar Altimeter
KMS	The National Survey and Cadastre, Denmark
MIZ	Marginal Ice Zone
NOAA	National Oceanographic and Atmospheric Association
PLF	Pulse Limited Footprint
PP	Pulse Peakiness
SAR	Synthetic Aperture Radar
SGDR	Sensor Geophysical Data Record
SSM/I	Special Sensor Microwave Imager

Contents

Chapter 1

Introduction

Sea ice covering the polar regions has long been of human interest primarily to the shipping business and to some extent the oil business. In recent years the extent of sea ice together with ice thickness have become important to climatologists in order to understand, model and predict the climate changes.

Today satellites monitor the sea ice extent. Different sensors have been developed, each having their own advantages and limitations. Passive visible and infrared sensors cover large regions with medium resolution ($\sim$ 1 km), but are dependent of weather and daylight for the visible channels. To achieve a better resolution ($\sim$ 100 m) synthetic aperture radars (SAR/ASAR) are excellent choices. They operate in the microwave region and are independent of daylight and clouds. The major disadvantages using SAR/ASAR are that strong winds make the analysis difficult, or even impossible, due to increased surface roughness. Further, the high resolution puts constraints on the coverage due to the limited data storage onboard the satellite, e.g. an image of approximately 100 m resolution is typically limited to scales about 500 km. On the other hand passive microwave sensors cover large regions and are excellent for an overview such as to estimate effects of climate changes. To estimate sea ice extent by use of passive microwave sensors, problems may arise due to water vapor in the atmosphere and wind induced surface roughness, which may result in false sea ice targets. Extensive research has been conducted to counteract these effects. For a detailed analysis passive microwave products are useless as a result of the coarse resolution ($\sim$ 25-50 km). To summarize, each sensor has its limitations but by mixing the products they complement each other.

Until now only little attention has been paid to satellite based sea ice thickness measurements. The principal reason is the fact that the sea ice cover is thin and there have not been developed the technique to resolve the resolution on such small scales, until recently.

Throughout the years many attempts have been made to monitor the sea ice thickness. The oldest and the most precise method is *bore hole drilling*. As the method demands in situ measurements data collected is very limited in time and space. An-

other useful method is the use of *upward looking sonars* either carried by a submarine or mounted to fast moored buoys. Moored buoys only samples at fixed locations whereas submarines tend to sample limited areas for only a few weeks each year (Wadhams and Comiso, 1992). This is however not sufficient to deduce full regional and seasonal variations. *Airborne laser altimetry* alone (Jacobsen (2001), Forsberg et al. (2003)) or in combination with an *electromagnetic (EM)* induction device has shown to be a successful method to map the sea ice thickness (Haas et al., 1997). These methods are limited similarly to the case of submarines. *Freeboard measurements by satellite* is the only method which can measure sea ice thickness at the time and length of scales that climate investigation demands.

This Study

The main purpose of this thesis is to investigate space borne radar altimeter return signals over sea ice in north east Greenland. The radar altimeter is a nadir looking active sensor operating in the microwave region of the electromagnetic spectrum (0.3-40 GHz) which makes it insensitive to weather and the need of daylight. The altimeter measures heights and the shape of the return signal of one pulse, known as the waveform. The altimeter data evaluated in this thesis were monitored by the ENVISAT satellite altimeter RA-2 operating at 13.575 GHz. The resolution along-track for the RA-2 is about 390 m and the range resolution about 0.5 m.

In particular, the following questions will be discussed in this thesis:

- Is it possible to extract information of the sea ice conditions such as the extent and concentration ?
- Is it possible to estimate the sea ice thickness ?

In order to investigate sea ice extent, the shapes of the waveforms are studied as the shape of the waveform are an indicator of the surface properties. The waveform is dependent on the surface roughness, i.e. rough surfaces generate diffuse scattering, and a sharp ramp at nadir incidence together with a slow decline in power at off-nadir incidence angles characterize the typical waveforms. Plane surfaces on the wavelength scale (less than 3 mm for ENVISAT) show specular or quasispecular reflection. The characteristic waveforms of specular reflection have high peak power at nadir and a rapid decline at off-nadir angles. Waveforms over open ocean generate diffuse scattering (Chelton and McGabe, 1985). Large variations occur in the waveforms over sea ice covered surfaces, both in peak power and shape, reflecting the large variations in sea ice types and settings. High peak power (up to about 48 dB) is believed to originate from open water in the ice cover or newly formed ice in cracks and leads (Drinkwater (1991), Ulander and Carlström (1991), and Ulander (1987)). On the other hand large ice floes or fast ice is believed to generate diffuse scattering (Laxon (1994b) and Drinkwater (1991)).

Data and Parameters

To detect and quantify the sea ice from altimetry data the shape of the waveforms has been parameterized in different ways to discriminate the specular waveforms from the diffuse. The parameters to be extracted here are:

- Backscatter Coefficient
- Peak Power of the Waveform
- Pulse Peakiness Parameter

These parameters are mapped onto respective ground tracks during two periods: 6-13 October 2002 representing the beginning of the *freeze up* and 9-15 April 2003 representing winter conditions. The variations in the parameters are compared to the ice conditions by use of nearly coincident cloud free NOAA images.

The first and only method known to date to determine sea ice thicknesses based on *satellite radar altimetry*, was proposed by Peacock and Laxon (2001). The method has been developed using ERS altimetry data and verified by using *upward looking sonar* measurements. The results are estimated to be accurate to within 50 cm on scales of 100 km.

To estimate the sea ice thickness by space borne altimetry a method used to estimate sea ice thickness by airborne laser altimetry is adapted. The method was first presented by Jacobsen (2001) and Hvidegaard and Forsberg (2002) and later used in ESAG-2002, Forsberg et al. (2003), and most recently during CryoVex April 2003 (personal communication S. M. Hvidegaard). The method is based on the freeboard, combined with a geoid model used to approximate sea level. As the specular waveforms are expected to originate from open water or newly formed ice, the corresponding heights give a correction to the mean sea level approximated by the geoid model. The discrimination of specular and diffuse waveforms are classified regarding the pulse peakiness parameter (Peacock and Laxon, 2001). The freeboard is converted to thickness by knowing the relationship between ice freeboard and draft (Comiso et al. (1985) and Wadhams et al. (1992)). In this thesis the sea ice thicknesses of two subtracks from the 11th and 12th of April 2003 nearly coincident with available SAR/ASAR images, are found.

In the assumptions made above, the range measured by the altimeter is assumed to originate from the snow surface. In the works done by Peacock and Laxon (2001) it is assumed that the range originates from the snow-ice surface. It is unknown whether the reflection originates from the snow surface or the snow-ice surface. This uncertainty may lead to large errors on the sea ice thicknesses. A transponder has shown to be valuable to define the snow surface of the Greenland ice sheets (Haardeng-Pedersen et al., 1998). As a part of this thesis a transponder belonging to the Department of Geophysics, University of Copenhagen, was tested in Rungsted,

Denmark. The test was performed as a part of the preparations for future field works to better understand the scattering mechanisms of the sea ice.

This Report

The contents of this thesis is as follows: Chapter 2 gives a brief introduction to the sea ice environment in north east Greenland, e.g. circulation patterns, ice types and settings. Chapter 3 includes a thorough theoretical background of the altimeter operation, with a particular focus on the ENVISAT altimeter characteristics. This chapter also presents scattering theory at normal incidence and a description of the changes in waveforms expected as the altimeter moves from open ocean into an ice covered area. Chapter 4 introduces the parameters to describe the waveforms followed by the method to estimate the sea ice thickness. Chapter 5 gives a description of the data used in this project. Chapter 6 presents the results and these are discussed in details. Finally chapter 7 contains the conclusion and recommendations for future operations. Appendix F includes the test of the transponder.

Chapter 2

Ice Conditions in North East Greenland

In this project the data analysis is limited to north east Greenland, see figure 2.1. This area is of particular interest to the climatologists as it represent the area of largest outflow of freshwater and sea ice from the Arctic Sea through the Fram Strait. The annual ice flux through the Fram Strait is approximately 3,000 km^3 per year (Schmidt and Hansen, 2003), but varies from year to year as well as from season to season. The southward sea ice flux through the Fram Strait is generally 3-4 times larger during the winter months than in the summer months. An important reason for the seasonal change in the sea ice flux is the intensified sea level air pressure gradients (see figure 2.3), due to the frequent and deep lows near south east Greenland in the winter period. Also, the seasonal changes in freshwater input to the Arctic Ocean and the *East Greenland Current* (EGC) contributes to the variability in the southward ice drift.

In the following, the basic geophysical mechanisms, e.g. circulation patterns and the various sea ice conditions present in north east Greenland, are described.

2.1 Circulation Patterns and Sea Ice Distribution

Figure 2.2 shows the circulation patterns of the upper ocean layers in the Arctic Sea. The circulations are dominated by the anticyclonic *Beaufort Gyre* in the Canadian Basin and a weaker cyclonic circulation in the Eurasian basin separated by the *Transpolar Drift Stream*. Normally, the drift of the sea ice follow these currents. Passing the *Fram Strait* the sea ice is carried southward in the *East Greenland Current* (EGC) forced to follow the Greenland coast by the Coriolis force.

The East Greenland ice extent is at its minimum extent (on average near Scoresbysund) in early September. In the fall the ice rapidly drift south in the EGC and normally reaches the Cape Farewell area in late December. In spring and summer the

Figure 2.1: Map of Greenland. The black box defines the area of interest. The white area bounded by the pink line represents the ice conditions in April 2003 typical winter conditions and the blue line represents minimum ice extent September 2002.

Figure 2.2: The circulation patterns of the Arctic Basin and the North Atlantic Sea (Source: See chapter 8)

sea ice frequently passes Cape Farewell and drift westwards. From time to time the sea ice enters the Labrador Sea drifting northwards along the west coast, sometimes reaching as far as 62°N, where the sea ice dissolves by melting and deterioration by wind and waves. The sea ice extent culminates in one of three months; May, June or July (Schmidt and Hansen, 2003) and retreats to its minimum extent. The length of the South Greenland ice season and the northernmost distribution varies irregularly from year to year.

2.2 Definitions/terminology

The description of the sea ice environment contains a number of terms to describe the sea ice thickness or stage of development. In the table below the definitions

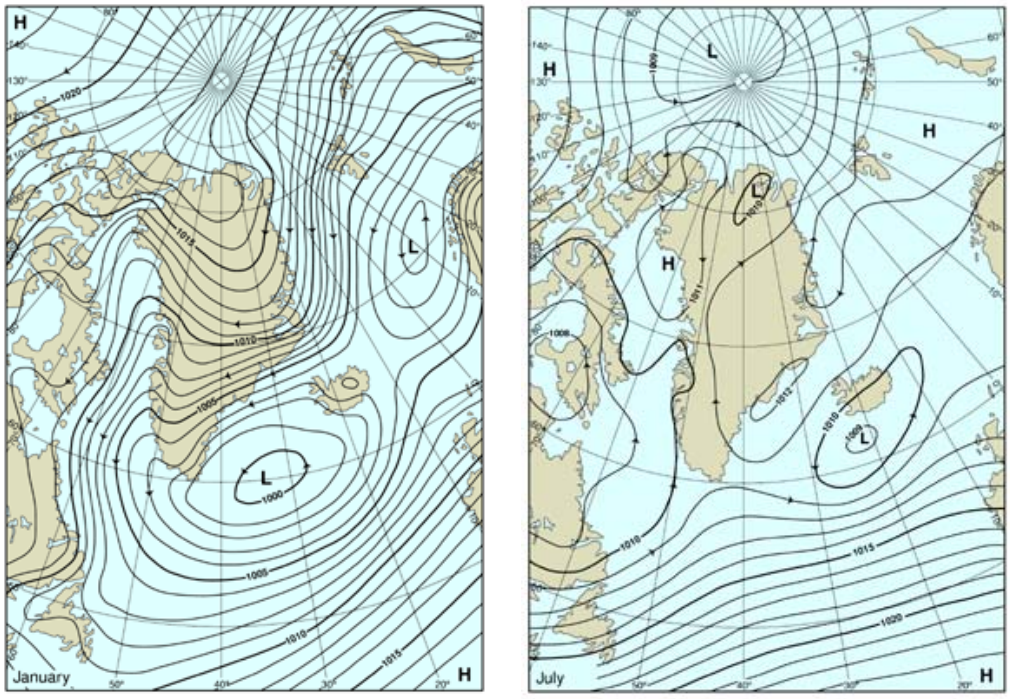

(a) Winter conditions

(b) Summer conditions

Figure 2.3: Mean sea level air pressure (hPa) winter and summer (DMI).

formulated by the World Meteorological Organization (1970) are listed.

Ice Type	Thickness	Comments
New Ice	0-10cm	
Young Ice	10-30cm	
First Year Ice	30-200cm	Sea ice of not more than one winter's growth
Multi Year Ice	> 2m	Sea ice having survived at least one summer's melt

2.3 Sea Ice Types and Settings

The sea ice in north east Greenland may represent one of the areas having the largest variations. The main ice type present all year is multiyear ice, also known as polar ice. The multiyear ice originates from the Arctic Sea and is several years old and the normal thickness is about 3-4 meters. But the area also includes thinner ice types (new ice, young ice and first year ice) depending on time of year. Within these classes ice may appear in different settings (rafted ice, ridged ice, hummocked etc.).

The *Fram Strait* is a very dynamic region where the ice is influenced by winds and currents. In divergent areas the ice is spreading, leaving cracks and leads which refreezes at subzero temperatures, leaving areas of thinner ice. In convergent areas the sea ice is pushed together by convergent wind fields and *ridges* are formed. In this way, the ice becomes thicker than by freezing alone. *Old ridges*, including piled up snow, are referred to as *hummocks* and can easily rise ten meters above sea level and 30 meters below. Many *ridges* and *rubble fields* of first year ice is formed along the edges of multiyear ice. In figure 2.4 (a)-(d) a series of pictures, taken at an underflight the 11th of April 2003 in north east Greenland, represents some of the different types and textures of sea ice described.

The *ice edge* is the demarcation line between open ocean and ice covered waters, and the ice covered area bounding up to the ice edge is known as the *marginal ice zone* (MIZ). The sea ice in the MIZ is exposed to wind and waves and depending on the prevailing wind direction and strength the ice concentration can change in a few days. Northern and eastern wind directions results in packing of the ice leaving high concentrations (9/10) and a well marked ice edge. The ice concentration is defined by World Meteorological Organization (1970) to be expressed in ratios of tenths, describing the amount of the sea surface covered by ice as a fraction of the whole area being considered. Western and southern wind directions causes lower concentrations (1-6/10) arranged in belts of high concentration (9/10) and a diffuse ice edge.

The waters off the multiyear ice edge in the Greenland Sea, north of Jan Mayen, play an important role in the ocean circulation and the climatic variability. One effect of the ocean convection processes and the atmosphere-ocean interaction is the formation of the "Odden" area in the Greenland Sea, see figure 2.1. The strength and timing of the formation of the Odden area varies inter annually and some winters it is weak or non-existing, other years it is present for several months. The Odden area is characterized by relatively thin ice types, i.e. new and young ice.

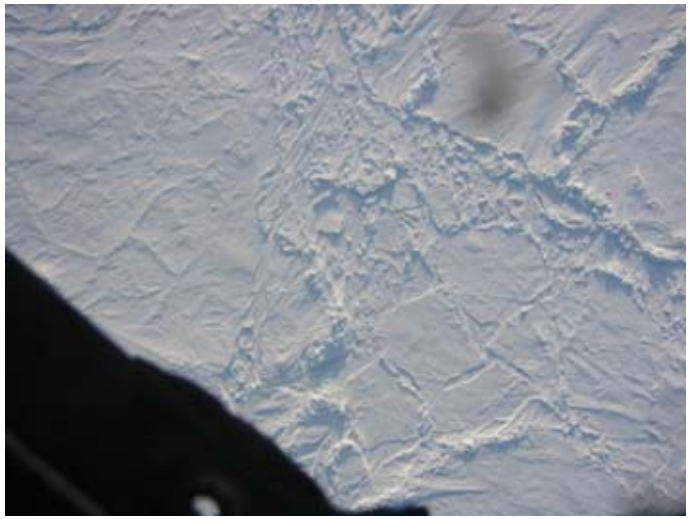

(a) Multiyear icefloes imbedded in ice of less thickness

(b) First year ice floe

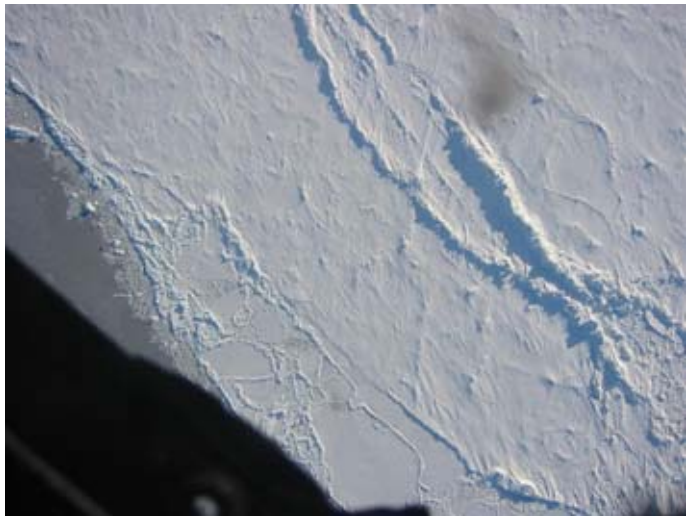

(c) Ridges

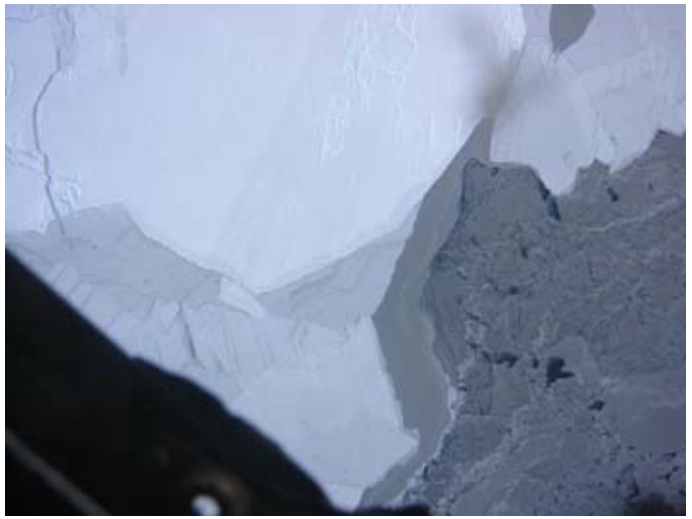

(d) Thin and new ice. In the lower left corner an example of finger rafting (thin ice sheets sliding on top of each other)

Figure 2.4: Photographies taken during underflight 11th of April 2003 (KMS)

Chapter 3

Space Borne Radar Altimetry

The following has been adapted from Fu and Cazenave (2001), chapter 1, unless otherwise stated.

3.1 Basic Principles

The basic principles of an altimeter is very simple. The altimeter transmits an electromagnetic pulse and measures the time it takes the pulse to reach the surface at nadir and return to the altimeter. As electromagnetic radiation travels with the speed of light in vacuum the distance from the satellite to the surface (R_0) is to a first approximation given by:

$$R_0 = c\,(t_0/2) \tag{3.1}$$

where c is the speed of light and t_0 the two-way travel time measured by the altimeter.

The range defined in equation 3.1 is overestimated. This is caused by refraction in the intervening atmosphere, i.e. the atmospheric refraction index is larger than the refraction index of vacuum (n(vacuum)=1, n(atmosphere)>1). According to the relation

$$v = c/n \tag{3.2}$$

a larger refraction index results in a slower speed. Taking refraction into consideration the corrected range (R) is given by

$$R = v\,(t_0/2) = \frac{c\,(t_0/2)}{n} \tag{3.3}$$

or expressed in terms of R_0

$$R = R_0 - \Delta R \tag{3.4}$$

where ΔR represents the correction term due to refraction. The correction due to the atmosphere can be divided into three different categories see figure 3.1. A contribution originating from dry gasses, the main contributor being oxygen (O_2), a contribution from water vapor (H_2O) and one originating from ionospheric jam (primarily electrons). Adding these corrections the range can be expressed by

$$R = R_0 - \sum_i \Delta R_i \tag{3.5}$$

The elevation of the surface observed at nadir above the reference ellipsoid[1], known as the ellipsoidal height (h) is to a first approximation given by

$$h = H - R \tag{3.6}$$

where R is the range and H the altitude or orbital distance of a satellite centre of mass above the reference ellipsoid.

The altitude is determined by *precise orbit determination* (POD). For ENVISAT this is done by use of *precise range and range-rate equipment* (PRARE) and *doppler orbitography and radiopositioning integrated by satellite* (DORIS). Both systems are based on ground to satellite measurements. PRARE is a highly accurate microwave ranging system, supported by a network of mobile ground stations, which are used for orbit determination at decimeter level of accuracy as well as for various geodetic applications. For further information, see links chapter 8.

In addition, different instrument corrections, see figure 3.1, e.g. the doppler-shift caused by the satellite motion compared to the Earth, have to be applied.

[1] The reference ellipsoid is defined as the ellipsoidal surface approximating the mean sea level

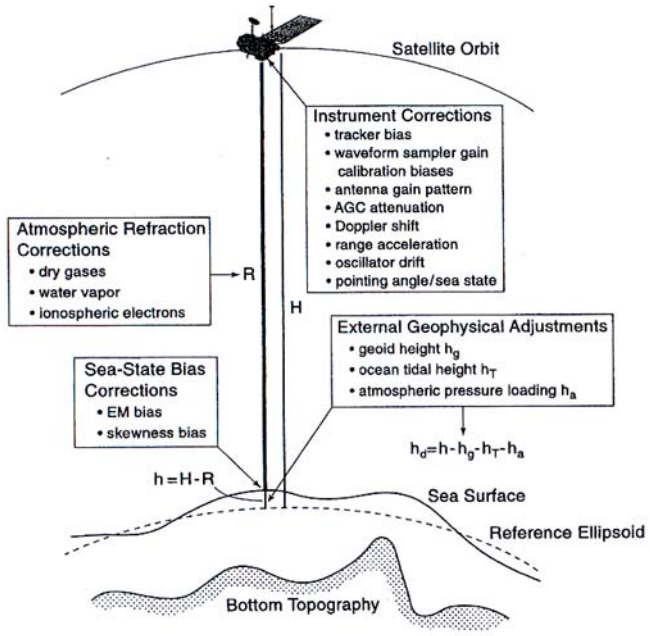

Figure 3.1: Definition of heights and corrections relevant to satellite altimetry (Fu and Cazenave, 2001).

3.2 The Radar Equation

Physically the altimeter measures the strength and shape of the returned signal from which the two-way travel time can be extracted. In the following the power of the return signal is expressed by the radar equation and the shape of the returned signal of one pulse called a waveform will be introduced.

The power of the returned signal measured by the altimeter depends upon the scattering characteristics of the surface, the parameters of the radar system and the two-way attenuation by the atmosphere. The effect of the returned signal (P_r) can be expressed geometrically by the radar equation:

$$P_r = \frac{t_\lambda^2 G_0^2 \lambda^2 A_{eff} \sigma^0}{(4\pi)^3 R^4} P_t \tag{3.7}$$

where t_λ is the attenuation of the electromagnetic waves as they progress through the atmosphere; squared due to the fact, that the waves passes through the atmosphere twice. The parameter G_0 is the maximum antenna gain at nadir incidence angles. For the altimeter the same antenna works as transmitter and receiver and as a consequence the antenna gain must be squared. λ is the wavelength of the altimeter, R the measured distance after correction of the atmospheric refraction,

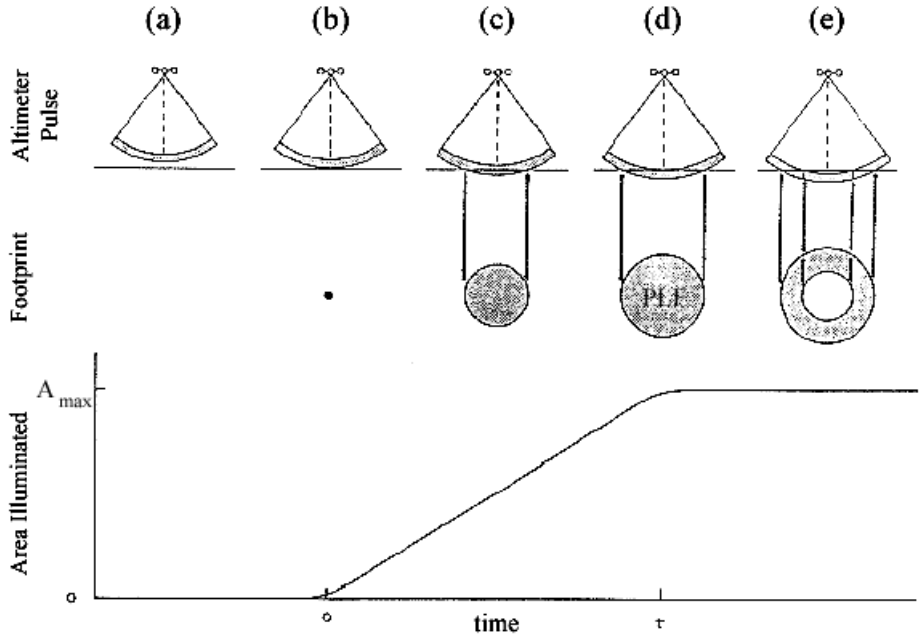

Figure 3.2: Propagation of the pulse and the corresponding footprint shape and illuminated area (Chelton, 1988).

see equation 3.4. A_{eff} is the effective footprint area of the altimeter defined in section 3.2.2, and σ^0 is the effective backscatter coefficient as defined in chapter 3.3. For a detailed review of the radar equation, see Ulaby et al. (1982).

3.2.1 The Footprint Area

The area, by which the pulse intersects the surface, is known as the footprint area of the altimeter and can be explained by examining figure 3.2. It is assumed that the pulse form is a *stepfunction* of width $c\tau$ (c: the speed of light, τ the compressed pulse length) and the surface is plane. The pulse expands as a spherical shell from the altimeter, see figure 3.2 (a), the thickness of the shell being the pulse width. The point of 'first return', figure 3.2 (b), results from reception of the *leading edge* of the pulse at normal incidence from the instant at which the wavefront intercepts the surface. As the *leading edge* proceeds the footprint area becomes an expanding circle, see figure 3.2 (b)-(d), until the point where the *trailing edge* of the pulse reaches the surface, figure 3.2 (d). In the subsequent time the pulse expands as an annulus at the surface, figure 3.2 (e), resulting in a constant footprint area. The maximum footprint area, figure 3.2 (d), is known as the *pulse limited footprint* (PLF). The expansion of the altimeter footprint can be described by simple geometry, for details see appendix A.

3.2.2 Definition of Waveforms

The shape of the return signal from one pulse as a function of time is called the waveform and is to a large extent defined by the footprint area.

For a plane surface the footprint is illuminated 100% at any given time, and the effective footprint area approximates the theoretical footprint area described above. In case of a rough surface, i.e. swells on the ocean, the effective area is the area illuminated at a given moment inside the footprint. The illuminated area fluctuates in time resulting in noise on the individual waveforms. To reduce the noise the waveforms are averaged, see figure 3.3.

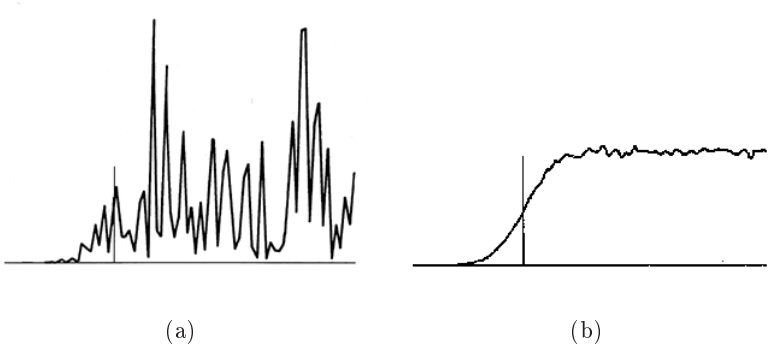

(a) (b)

Figure 3.3: (a) An individual waveform and (b) 1000 individual waveforms averaged (Fu and Cazenave, 2001).

The presence of waves also affects the leading edge of the waveform, which becomes stretched in time, i.e. the 'first return' of the pulse has been replaced half a wave height above mean sea level and the last return of the trailing edge at nadir has been replaced half a wave height below mean sea level, see figure 3.4 (a). The exact two-way travel time (t_0) corresponding to returns from the mean sea surface height is defined as the *half power point*, see figure 3.4 (b).

Figure 3.4 (b) also shows the effect of the drop in the trailing edge, called the *plateau region*. At least two factors influence the decay of the trailing edge of the waveform. That is, the reduction in backscatter with increasing incidence angle and the effect of antenna gain pattern, see appendix A.

Although the illustration of the waveform is correct, e.g. over open ocean, the concept of a slow decline in power after the peak in the return signal is not the only shape of the waveform. Above surfaces, which approach specular reflectors, e.g. sea ice and transponder signals, a more rapid decline in power is registered (Drinkwater, 1991), see also next section 3.3.

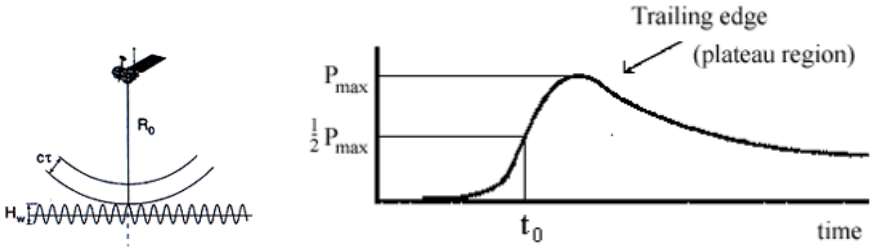

(a) (b)

Figure 3.4: Pulse propagation incident on a wavy surface (a) and the corresponding waveform (b), where the *half power point* defines the return from mean sea level at nadir. The waveform also illustrates the decline in power with increasing incidence angles (Fu and Cazenave, 2001).

3.3 Backscatter at Normal Incidence

The following has been adapted from Ulaby et al. (1982), chapter 2, unless otherwise stated.

The altimeter was originally designed for operation over open ocean, but it was soon realized that the altimeter character changes over sea ice covered regions; Ulander (1987), Drinkwater (1991), Ulander and Carlström (1991), and Laxon (1994b).

On the basis of dielectric characteristics alone the ocean backscatter is expected to be greater than for ice (Fetterer et al., 1992), and for surface measurements of backscatter at nadir this is usually the case. On the other hand the dynamic range of altimeter measurements over ice can not be explained by the variability in the dielectric characteristics of ice alone. Since backscatter for satellite altimeters is dominated by surface rather than volume scattering the nature of altimeter pulse echoes must be primarily determined by surface roughness.

Reflection from a smooth surface is called specular reflection, see figure 3.5 (a), and is described by the Fresnel reflection laws (Elbek, 1995). A monostatic radar (transmitter and receiver at the same location), would, theoretically, receive no return power from a smooth surface except at normal incidence .

No naturally occurring surface is perfectly smooth. A wave incident upon a slightly rough surface is partly reflected in the specular direction and partly scattered in all other directions see figure 3.5 (b). The magnitude of the reflected component is smaller than for the smooth surface. This specular component is often referred to as the coherent scattering component. The scattered component, also known as the

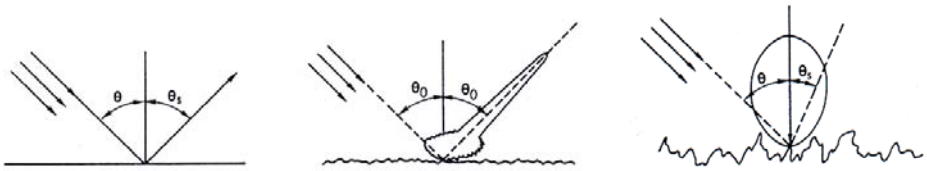

(a) The reflected power is entirely coherent

(b) Scattering pattern consists of large coherent component and small diffuse component

(c) Scattering pattern is composed entirely of diffuse component

Figure 3.5: (a) specular, (b) slightly rough and (c) very rough (Ulaby et al., 1982)

diffuse or noncoherent component, consists of power scattered in all directions, but its magnitude is smaller than that of the coherent component.

As the surface becomes rougher, the coherent component becomes negligible, see figure 3.5 (c). Finally, for the very rough surface, the radiation pattern approaches that of a Lambertian surface which consists of only diffuse scattering.

In terms of altimeter waveforms diffuse scattering are characterized by a low backscatter signal at nadir and a slowly trailing edge, see figure 3.6 (a) and specular returns characterized by large nadir peak power followed by a rapid fall-of, see figure 3.6 (b).

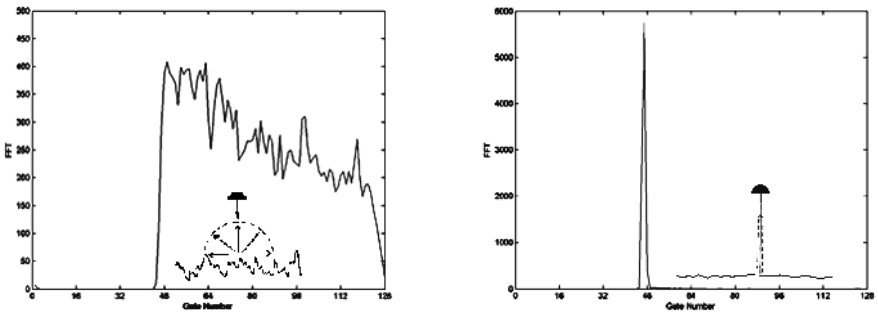

(a) Diffuse waveform

(b) Specular waveform

Figure 3.6: Typical ENVISAT altimeter waveforms acquired from (a) rough surfaces and (b) flat surfaces. These waveforms show received power in FFT versus time. Note: The y-axes are not to scale.

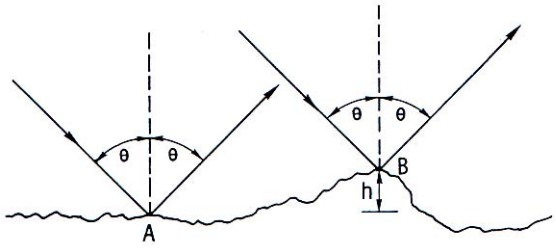

Figure 3.7: The Rayleigh criterion illustrated (Ulaby et al., 1982)

For a surface to be considered smooth the Rayleigh criterion must apply. The geometry is shown in figure 3.7. The Rayleigh criterion states that if the phase difference $\Delta\phi$ between the two reflected rays is less than $\pi/2$ radians, then the surface may be considered smooth. From the geometry, $\Delta\phi = 2khcos\theta$, which, if set $< \pi/2$, leads to

$$h < \frac{\lambda}{8\,cos\theta} \tag{3.8}$$

Reducing to $h < \lambda/8$ for an altimeter (θ=0). The Rayleigh criterion leads to a surface roughness of less than 3 mm for ENVISAT using λ=2.2 cm.

To a first approximation the Rayleigh criterion is sufficient to define the smoothness, but a more stringent criterion is needed in order to apply for microwave radiation. For this purpose the Fraunhofer criterion is introduced. The Fraunhofer criterion requires the maximum phase difference between the rays at nadir to be less than $\pi/8$ compared to the edge of the antenna. Such a requirement leads to the condition

$$h < \frac{\lambda}{32\,cos\theta} \tag{3.9}$$

for a surface to be considered smooth. Equation 3.9 reduces to $h < \lambda/32$ in case of an altimeter. The Fraunhofer criterion restricts the roughness conditions for the surface to be less than 0.7 mm using λ=2.2 cm (ENVISAT). Most naturally occurring surfaces are not smooth on the milimeter scales, at least not for very large areas.

3.3.1 Open Ocean Backscatter

The mechanisms influencing the altimeter return signal over open ocean are well understood. The waveform have only smooth variations in shape for periods of seconds. At normal incidence the backscatter values are in the range 8-15 dB (Chelton

and McGabe, 1985) with a slowly decreasing trailing edge. This waveform is characteristic for incoherent (diffuse) scattering. Actually, the ocean is regarded as a continuous rough surface of specular point scatterers, where the incoherency primarily is a consequence of the random elevation of the specular points. In order to extract geophysical information it is important to have a good theoretical model. The most widely used ocean model was developed by Brown (1977). In addition to a very precise height measurement the shape of the ocean waveform gives information of the waveheights by the slope of the leading edge and the wind speed by the maximum backscatter value.

3.3.2 Sea Ice Backscatter

Contrary to the open ocean the waveform over sea ice exhibits large fluctuations from one waveform to another, both in shape and peak power, reflecting the large variations in ice types and settings. Both waveforms of specular (or quasi-specular) and diffuse scattering are observed.

Typically, specular or quasi-specular waveforms of high peak power up to 48 dB will occur, see chapter 6.1. The likely source of specular echoes in sea ice are reflections from calm water or new ice between floes. These surfaces contribute as plane surfaces and has a higher reflection coefficient than most snow covered sea ice surfaces. The power reflection coefficient for water is typically 11 dB higher than for most snow or firn-covered sea ice surfaces (Drinkwater, 1991). Many scientists have contributed to the registration of the specular signals. To mention a few, Ulander and Carlström (1991) have registered high backscatter over new and young ice in between 15-40 dB and Ulander (1987) has registered 12-40 dB in peak power over new ice.

Even if coherent reflections originate from only a small fraction (less than 1%) of the surface near nadir, they can dominate the return echo (Drinkwater, 1991). This corresponds to the first few Fresnel zones.

To define the Fresnel zones it is assumed that the light incident on the surface to consist of plane wavefronts. This requirement is fulfilled by space borne altimetry as the height of the satellite is large compared to the radius of the inner Fresnel zones. The successive Fresnel zones (concentric circles centered at nadir) alternatively provide constructive and destructive interference. The zone limits are located where the wavelength of the reflected wave has changed by $N\lambda/2$ compared with a reflection from the nadir point. This is expressed by

$$D_N = \sqrt{2NH\lambda} \tag{3.10}$$

The first Fresnel zone for ENVISAT is 188 m and the second 265 m (using H=800 km and λ=2.2 cm).

Diffuse waveforms with peak power comparable to those of open water have been observed and investigated by Laxon (1994b) and Drinkwater (1991). They have, by comparing altimeter data to additional remote sensing products (infrared AVHRR images and photography taken from airplane), found the diffuse waveforms to originate from fast ice and vast floes, where the altimeter footprint is entirely filled with consolidated ice. The diffuse return is a consequence of the less reflective and rougher sea ice floe surface. Ulander (1987) the peak power to be 12-30 dB for multiyear ice.

3.4 Pulse Compression

Space borne altimeters use a technique called *pulse compression*. This is done to circumvent some basic problems arising, requiring a large energy to gain a high *signal-to-noise ratio* (SNR). An effective instrument is characterized by a high SNR. The energy contained in a pulse is given by the following relation:

$$E = P\,\tau \tag{3.11}$$

here E is the energy, P the power and τ the transmitted pulse length. A large energy implies either the power to be large or the pulse length to be long. A large power will put a strong requirement on the space borne system and thereby limit the lifetime of the satellite. On the contrary a long pulse length is achieved on the expense of a lower range resolution, as the range resolution is proportional to the pulse length.

The *pulse compression technique* solves this problem by keeping a low power by emitting a relatively long (on the order of microseconds) pulse. The pulse echo is processed in a way equivalent to measuring the travel time to the surface and back of a much shorter pulse only a few nanoseconds long, resulting in high resolution.

Technically, the pulse compression is accomplished by transmitting a *linear frequency modulated* (LFM) pulse, called a chirp, see figure 3.8. The returned signal is composed of many chirps each reflected from a different facet of the surface. Each of the returned chirps is subtracted from a delayed replica of the transmitted signal, resulting in a frequency constant in time. Each of the intermediate frequencies corresponds to a given height on the surface. By *fast fourier transform* (FFT) the intermediate frequencies are transformed from the frequency to the time domain resulting in the waveform.

The time domain of the waveform is sampled into a limited number of time intervals (128 for ENVISAT). The duration of the time intervals, called *one bin* or *range gates*, are given by the *compressed pulse length* (τ), which is inversely proportional to the bandwidth (B) of the transmitted pulse length:

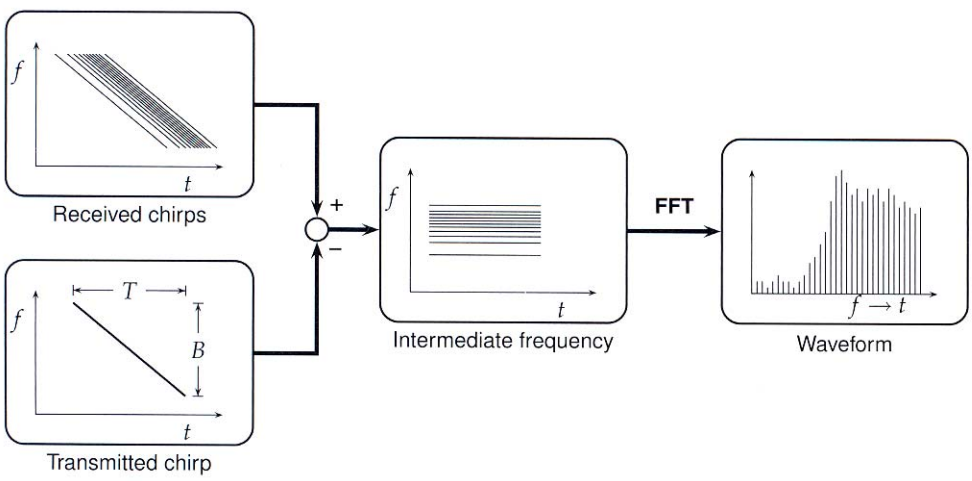

Figure 3.8: Illustration of the pulse compression technique (Scharroo, 2002).

$$1\,\mathrm{BIN} = \tau = 1/\mathrm{B} \tag{3.12}$$

The entire bins contained in the waveform is called the *range window*.

It is very important to be aware of the differences in the pulse length actually transmitted and the pulse length after compression. In the literature the pulse length after compression is called the *effective pulse length*, the *compressed pulse length* or simply the *pulse length*. To avoid confusion the pulse length after compression will be termed the *compressed pulse length* throughout this thesis. In the above the *transmitted pulse* length should be used to calculate the energy in equation 3.11 and the *compressed pulse length* in equation 3.12 should be used to calculate the resolution.

3.5 The ENVISAT Radar Altimeter

ENVISAT was launched the 28th of February 2002 as follow up to the ERS-1/2 satellites. The two ERS satellites each carried a radar altimeter (RA-1) and ENVISAT carries the improved radar altimeter (RA-2). The RA-2 has a higher pulse repetition frequency (1800 Hz), compared to RA-1 (1020 Hz). Both radar altimeters operate in the ku-band (see appendix A), for ENVISAT the frequency is 13.575 GHz corresponding to a wavelength of 2.2 cm.

The orbit is sun synchronous with a mean altitude of 800 km covering 81.5°N/S. A 35 days repeat cycle covers the same groundtracks within 1 km of accuracy and is defined as one cycle. During one cycle the satellite orbits the Earth 501 times

corresponding to an orbit period of approximately 100 minutes' duration. Since the spacings of the orbit tracks vary with latitude, the density of revisiting is significantly higher at high latitudes than near the equator, see figure 3.9.

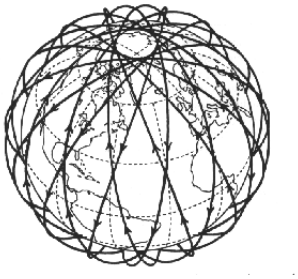

Figure 3.9: The distribution of polar orbits.

Instrument parameter	Range
Frequency Ku-band	13.575 GHz
Wavelength	2.2 cm
Pulse Repetition Frequency	1795.33 Hz
Transmitted pulse length	20 μsec
Compressed pulse length	3.125 nsec
Orbit Period	100 min

Figure 3.10: Characteristics of the ENVISAT radar altimeter RA-2.

The transmitted pulse length is 20 μsec. The compressed pulselength (τ) depends upon the bandwidth (B) of the chirped pulse, see equation 3.12. ENVISAT is operating with three bandwidths (320 MHz, 80 MHz and 20 MHz) each having a different bin interval, e.g. the widest bandwidth (320 MHz) has compressed pulse length τ=3.125 ns and a range window (128 bins) 400 ns wide. The range gates corresponds to the two-way travel time resulting in a range resolution given approximately by

$$\Delta R = c\,(\tau/2) \tag{3.13}$$

in this way τ=3.125 ns has a range resolution about 0.5 m. The entire range window can thus measure height variations up to approximately 60 m. The lower bandwidths (80 MHz and 20 MHz) correspond to coarser resolutions, see table 3.1. The reasoning to work with three different bandwidths is to gain the best possible resolution. Over open ocean surfaces, where the waveform have only smooth variations for periods of seconds, RA-2 always uses its highest resolution. Over coastal zones, ice and land, where the tracking could be lost due to the unpredictable and fast-changing waveforms, RA-2 can autonomously switch to a coarser resolution.

Bandwidth [MHz]	1 bin [ns]	Range resolution [m]	Range window [ns]	Height variations [m]
320	3.125	0.5	400	60
80	12.5	2	1600	240
20	50.0	8	6400	960

Table 3.1: The range resolutions and range windows corresponding to the three bandwidths available. The largest bandwidth corresponds to the best resolution, but put constraint on the height variations.

RA-2 transmits pulses every 557 μsec (corresponding to 1800 Hz). Averaging of 100 individual pulse waveforms results in an integrated footprint smeared in the along-track direction and corresponds to a resolution of approximately 390 m. The geometric resolution (cross-track) is represented by the *half power beam width* (HPBW) 1.3° corresponding to a footprint 18 km in diameter and a *pulse limited footprint* (PLF) area of 1.6 km, see appendix A.

In appendix A is also given a chronological review of space borne radar altimeter missions.

Chapter 4

Method

4.1 Parametrization of Altimeter Waveforms

Many attempts have been made to detect and quantify the sea ice from altimetry data. Most authors have parameterized the shape of the waveform in different ways in order to discriminate specular waveforms from diffuse, see appendix E.

In this project three parameters have been selected to use in the analysis of altimeter data over sea ice, see chapter 6. These are the:

- Backscatter Coefficient
- Peak Power of the Waveform
- Pulse Peakiness Parameter

4.1.1 The Sea Ice Backscatter Coefficient

The backscatter coefficient is contained in the SGDR product. In this thesis the backscatter coefficient is in the *sea ice mode* which is a tracking mechanism adapted to sea ice used in the data processing. The method to extract the backscatter shall not be mentioned here but the reader is referred to the ENVISAT RA2/MWR Product Handbook (2002). The evaluation of the backscatter coefficient has been included in this thesis, due to the fact that it is an easy parameter to access as it is a part of the data product directly delivered by ESA.

4.1.2 The Peak Power of the Waveform

The peak power is simply the maximum value contained in the waveform.

4.1.3 The Pulse Peakiness Parameter

The pulse peakiness (PP) dependens only on the waveform. It was introduced by Laxon and Rapley (1987) to permit filtering of anomalous data over open ocean, including sea ice. Assuming the waveform is roughly centered at the *tracking point*

in the range window (bin 44.5 for ENVISAT), PP is effectively a measure of the ratio of the peak power to the average power in the waveform. Thus, a high PP value represents a specular return and a low PP value represents a diffuse return.

For ENVISAT PP is given by

$$PP = \frac{44.5 \cdot P_{max}}{\sum_{i=10}^{128} P_i} \tag{4.1}$$

where P_{max} is the peak power and P_i the power in the i'th bin of the range window. The first ten bins are excluded since they contain aliased power.

Originally PP was used to filter data over open ocean using PP=1 as a limit, although noise, resulting from speckle in the altimeter return, results in a value closer to 1.5 (Laxon and Rapley, 1987). Knudsen et al. (1992) used PP less than 1.7 to remove sea ice. Strawbridge and Laxon (1994) use PP for quality flagging over land surfaces, where the altimeter is likely to loose track (keeping the *tracking point* in the range window). By accepting values of PP $\geq$ 1.1, up to 43 % of poorly tracked data is removed, with only 4.3 % loss of good data. The first to propose the use of PP for sea ice applications was Laxon (1994b).

4.2 Sea Ice Thickness using Space Borne Altimetric Data

4.2.1 Method to Estimate the Freeboard

In this thesis the technique to estimate the sea ice thickness from satellite altimetry is based on a method used by the National Survey and Cadastre, Denmark, in connection with laser altimetry measurements from airplane. The method was first presented by Jacobsen (2001) and Hvidegaard and Forsberg (2002) and later on used in ESAG-2002, Forsberg et al. (2003), and most recently during CryoVex April 2003 (personal communication S. M. Hvidegaard).

The altimeter scans the surface measuring the range from the altimeter to the surface. Knowing the exact altitude of the altimeter and the sea surface height it is possible to find the freeboard of the sea ice. To a first approximation the sea surface is assumed to match the geoid. The principle can be expressed as:

$$F = H_{POD} - R_{alt} - N - \Delta h \tag{4.2}$$

where F is the freeboard, H_{POD} is the height of the altimeter above the reference ellipsoid, R_{alt} is the range of the altimeter to the surface, N is the geoid height above the reference ellipsoid and Δh is deviations of the sea surface from the geoid caused by errors on the geoid model and changes in the sea surface topography due to tides

and permanent sea surface topography.

The mean sea level is defined where specular returns occur, as these are expected to originate from the open water in between the floes, see section 3.3.2. To discriminate diffuse waveform data from specular waveform data the Pulse Peakiness (PP) parameter (see section 4.1.3) is used as limit, i.e. waveforms with a peakiness of less than or equal to 1.8 is processed as diffuse (originating from either open ocean or ice floe surfaces), and those with a peakiness greater than 1.8 is processed as specular (Peacock and Laxon, 2001).

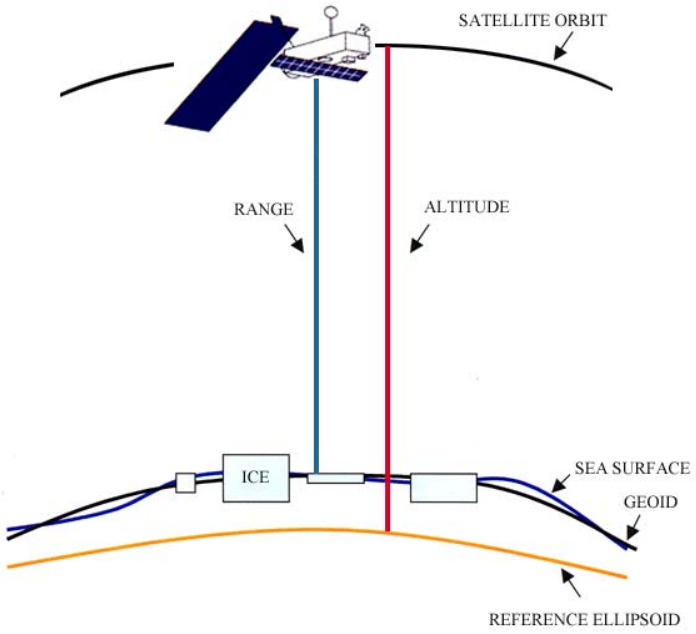

Figure 4.1: Illustration of the different heights and reference surfaces used to find the sea ice freeboard (Jacobsen, 2001).

4.2.2 Conversion of Freeboard to Thickness

To convert freeboard estimates to sea ice thicknesses, Comiso et al. (1985) and Wadhams et al. (1992) have shown that the ice freeboard can be converted to a draft value by simply multiplying the freeboard by a factor R. The surveys to estimate the value of R has been conducted by comparing *upward looking sonar* (ULS) with laser profiles at almost identical tracks. The thickness is thus related to the freeboard by the factor (1+R):

$$T = (1 + R)F \tag{4.3}$$

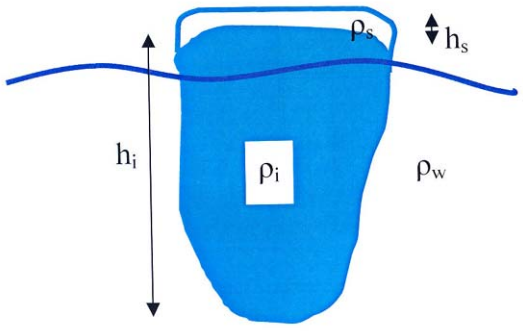

Figure 4.2: Sea ice floe in isostatic equalibrium (Forsberg et al., 2003).

where T is the ice thickness, F the freeboard and (1+R) the conversion factor. The measurements used in the survey done by Wadhams et al. (1992) gives an average R-value of 7.89.

The R-factor depends on the properties of snow, ice and water. Assuming isostatic equilibrium between sea ice including snow, and water, R is given by

$$R = \frac{\rho_i h_i + \rho_s h_s}{h_i(\rho_w - \rho_i) + h_s(\rho_w - \rho_s)} \tag{4.4}$$

where ρ is the density, h the height and the subscripts (i), (s) and (w) are that of ice, snow and water. The parameters involved are defined in figure 4.2.

Due to the snow load there is a large seasonal variation in R. In the work done by Wadhams et al. (1992) to estimate the R-factor the seasonal snow variations are based on field studies conducted in the 1960's (Maykut and Untersteiner, 1971). According to the field studies, the R-factor takes its highest value at the start of the snow season (with bare ice) on August 20th. Then, R falls rapidly during September and October, when the surface is covered by snow, and diminishes slowly between November until the end of April, when little snow falls. A further onset of spring snow brings R to its lowest level at the beginning of June. As soon as the snow melt begins, R rises rapidly until the end of June at which point it rises almost to its August value. The major uncertainty for the R-factor is the presence of snow.

In this project, data is taken on April the 11th and 12th, and R is chosen to be 4.89 valid from April 30th to May 31st (Wadhams et al., 1992). A sea ice freeboard F=20 cm gives approximate 120 cm in thickness or almost 6 times the freeboard.

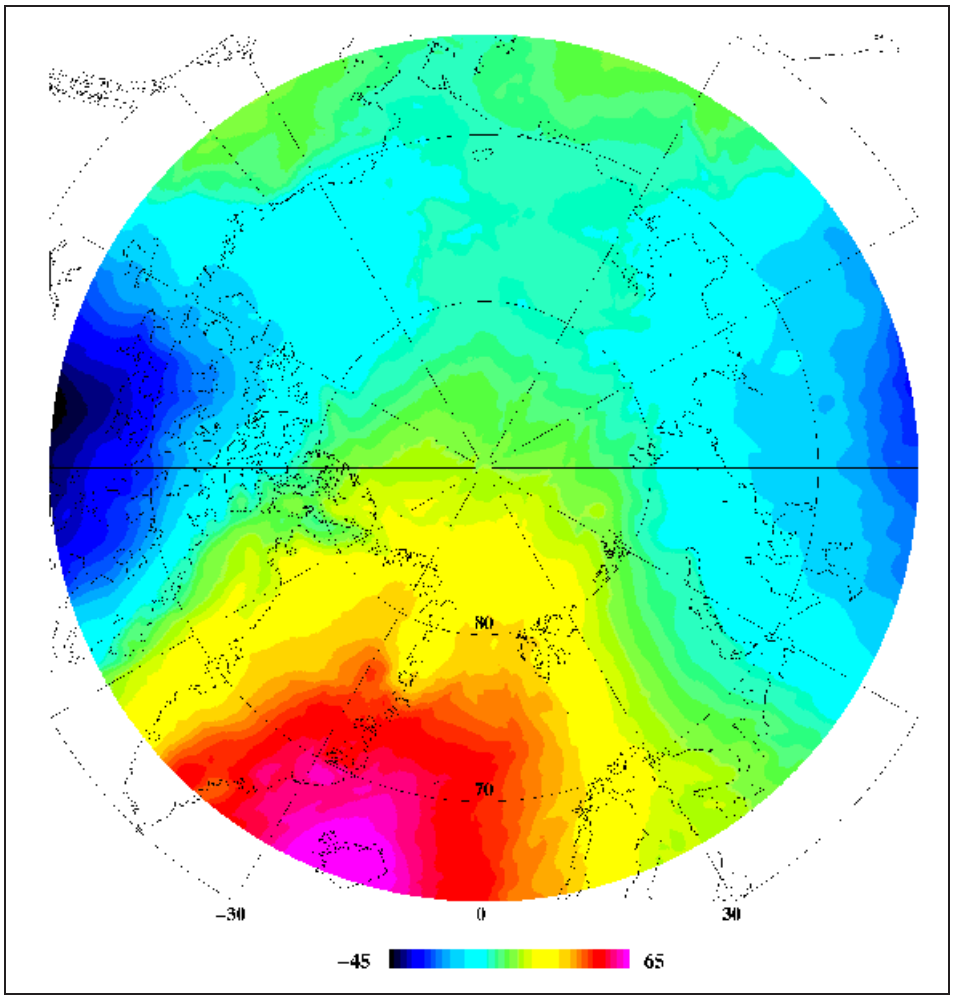

Figure 4.3: The Arctic geoid model (Source: See chapter 8).

4.2.3 The Geoid Model

A geoid model is used to approximate mean sea level. The most recent geoid model for the area of interest is a model developed from airborne as well as surface and submarine data under The Arctic Gravity Project (ArcGP), see figure 4.3. The data have been prepared by a working group under the International Gravity and Geoid Commission, International Association of Geodesy chaired by National Survey and Cadastre of Denmark (KMS) in cooperation with National Imagery and Mapping Agency (NIMA), and published as grid values.

The geoid is found using the program GEOIP from the GRAVSOFT package. Values in the individual points are obtained by bilinear interpolation.

Chapter 5

Description of Data

5.1 Data Availability

The data set available for this study comprises ENVISAT RA-2 altimeter data. For validation purposes additional remote sensing data (Radarsat SAR, ENVISAT ASAR, NOAA AVHRR and high resolution aerial photography) have been used to identify specific ice conditions and ice types.

The altimetry data set was kindly received from the European Space Agency (ESA). The raw data was processed at the French Processing and Archiving Center (F-PAC) in Toulouse, France, and saved in ENVISAT standard format. The data received is categorized as level 2b Sensor Geophysical Data Record (SGDR). For further description and overview of the different data products available see appendix B. The SGDR data record includes 18 Hz data corresponding to a resolution of about 390 m in the along-track direction, see chapter 3.5.

The data products used in this project is comprised of:

- Averaged Waveforms
- Range
- Altitude
- Groundtrack position latitude and longitude
- Sea ice backscatter

The RA-2 data used in this analysis spans two weeks; one week from 6-13 October 2002 (cycle 10), the other week from 9-15 April 2003 (cycle 15). Groundtracks covering north east Greenland during these periods are presented in figure 5.1 and 5.2. Three to five orbits pass the area daily assuming there are no interruptions due to instrument failures. In appendix B is listed a review of available orbits among which four tracks (11th October 2002, 10th April 2003 (two tracks) and 13th April

2003) are not complete due to lack of data.

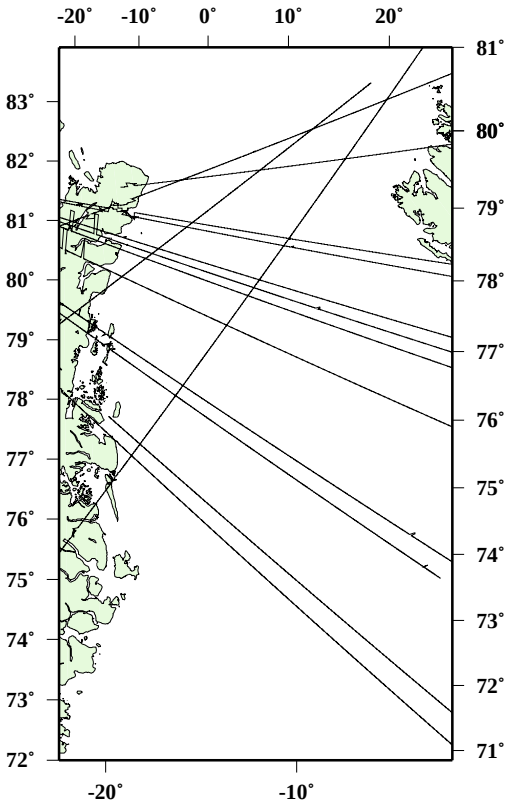

Figure 5.1: 6-13 October 2002

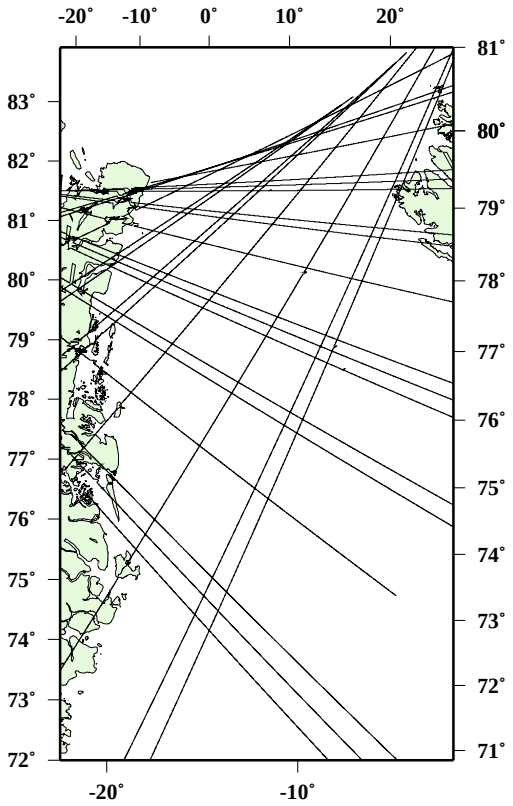

Figure 5.2: 9-15 April 2003

Cycle 10 has been selected for analysis as it was the first unofficial data set available. During cycle 10 the satellite was still in the commission phase resulting in frequent instrument and processing failures. This is the reason of the less dense spaced orbits of cycle 10 compared to cycle 15. Cycle 15 was the first cycle of ENVISAT RA-2 sensor data to be officially released to the users in the beginning of December 2003. Another crucial factor for focusing on this cycle is that during April 2003 many field activities to study the sea ice were conducted in north east Greenland. The surveys were primarily accomplished in favor of the CryoSat[1] validation experiment CryoVex to provide pre-launch reference data sets over sea ice. In particular, the aim was to understand sources of error such as snow loading, ice density, preferential sampling and freeboard measurements.

The 11th of April 2003 an underflight was conducted by KMS from Station Nord

[1]CryoSat is a radar altimetry mission to be launched in 2004. The first satellite to be realized in the framework of the Earth Explorer Opportunity Missions of ESA's Living Planet Programme. The main is to focus on the ice masses, including measurements of high precision icesheet elevations and sea ice thicknesses.

Data Type	Satellite	Period	# tracks
Altimetry RA-2	ENVISAT	9-15 April 2003	27
		6-13 October 2002	14
ASAR	ENVISAT	11 April 2003	2
SAR	Radarsat	11-12 April 2003	3
AVHRR	NOAA	9-16 April 2003	57
visible/infrared		5-15 October 2002	81
Photos	Airplane	11 April 2003	971

to Longyearbyen, Svalbard, in order to meassure sea ice thickness by use of laser altimetry. In addition, pictures were taken every 5th second corresponding to an approximate along-track interval on 610 m between successive pictures. The surface coverage of the images is about 250 m depending on the altitude, pitch, and roll of the airplane.

In favor of CryoVex two Radarsat SAR images and one ENVISAT ASAR image were available (DMI). The SAR images are from the 11th of April 2003 06.58 UTC and the other from the 12th of April 2003 16.29 UTC. The Radarsat images are all in a single beam standard mode, covering areas of approximately 110x100 km of approximately 100 m resolution. The ENVISAT ASAR image is monitored the 11th of April 2003 11.17 UTC. It is in dual polarization mode, covering 110x70 km with a resolution about 100 m.

NOAA advanced very high resolution radiometer (AVHRR) images were available during the whole period of consideration. On average 10 passes were monitored each day covering north east Greenland. The AVHRR operates in the visible (two channels) and infrared (three channels) spectra with a resolution of approximately 1 km.

In addition, model based meteorological charts from NCEP Operational Dataset were used. These charts contain information about strength and direction of the surface winds and surface temperatures.

5.2 Ice conditions based on NOAA AVHRR

In the periods under consideration, 6-13 October 2002 and 9-13 April 2003, only a few cloud free NOAA scenes were available. A NOAA image from the 5th of October 2002 and one from the 15th of April 2003 are analyzed below.

October 5th 2002

Figure 5.3 (a) shows the NOAA AVHHR image (visible channel) from October 5th 2002, 12.29 UTC. The image has been analyzed and divided into three classes (MIZ,

consolidated ice, and OW) characterizing different ice conditions. The magenta boundary represents the ice edges marking the transition from open ocean to ice covered waters. Analysis of the cloud covered parts are based on passive microwave image (SSM/I). The coarse resolution ($\sim$ 50 km) of the SSM/I image results in an estimated ice edge and ice boundaries marked by dashed lines. October is in the beginning of the *freeze up* season (see chapter 2) and represents minimum ice extent. Actually, 2002 was a unique year in terms of sea ice extent, as it represents the minimum extent observed in the months August and September during the last 110 years (Skourup, 2002).

The northernmost area of consolidated ice is composed of ice of high concentration (7-9/10). The floes are large, up to about 30 km in diameter, and are a mixture of multiyear ice embedded in new and thin ice. In the ice covered parts subzero temperatures, see figure 5.4 (b), cause thin ice classes (new and young ice) to be formed. The deep red color in figure 5.3 (a) confirms the presence of new ice.

The sea ice in the *marginal ice zone* (MIZ) is highly concentrated (5-7/10) arranged in belts of high concentration (9/10). The ice in the MIZ is exposed to wind and waves leaving small floe sizes less than 2 km in diameter.

October 2002 was characterized by medium wind speeds (5-10 m/s) from south, see figure 5.4 (a), which prevents the ice from drifting south in the *East Greenland Current* (EGC). Wind directions from south is actually seldom for the area at this time of year. Under normal conditions (see chapter 2) a high pressure is situated at the *Arctic Basin*, and deep lows are located south of Svalbard, causing northerly winds. But in this case there is a low pressure placed over the Artic Ocean and a weak high pressure south of Svalbard.

North east off the coast of Greenland an area of open water a *Polynya* is identified.
.

April 15th 2003

Figure 5.3 (b) shows a NOAA AVHHR image (visible channel) from April 15th 2003, 14.38 UTC. The ice covered parts are divided into four different regions (MIZ, consolidated ice, fast ice and the Odden area). Seasonally, April represents the month of maximum occurrence of sea ice, see chapter 2. The ice represents typical winter conditions and a well defined Odden area has been formed in the Greenland Sea.

Figure 5.5 (a) shows calm conditions (less than 7 m/s) in the area averaged over a week (9-15 April). The dominating wind direction is from south resulting in relative low concentration (4-6/10) in the *marginal ice zone* (MIZ) packed in high concentrated belts (9/10).

The area of consolidated drift ice is characterized by sea ice of high concentration (7-9/10) and large ice floes (up to 50 km in diameter). The ice types are a mixture of first year and multiyear ice floes embedded in younger ice classes.

During *freeze up*, fast ice has formed along the coast covering large areas of relative homogeneous ice. The mean temperature for April is subzero, see figure 5.5 (b), indicating that new ice is continuously forming in open leads and meltponds are refrozen.

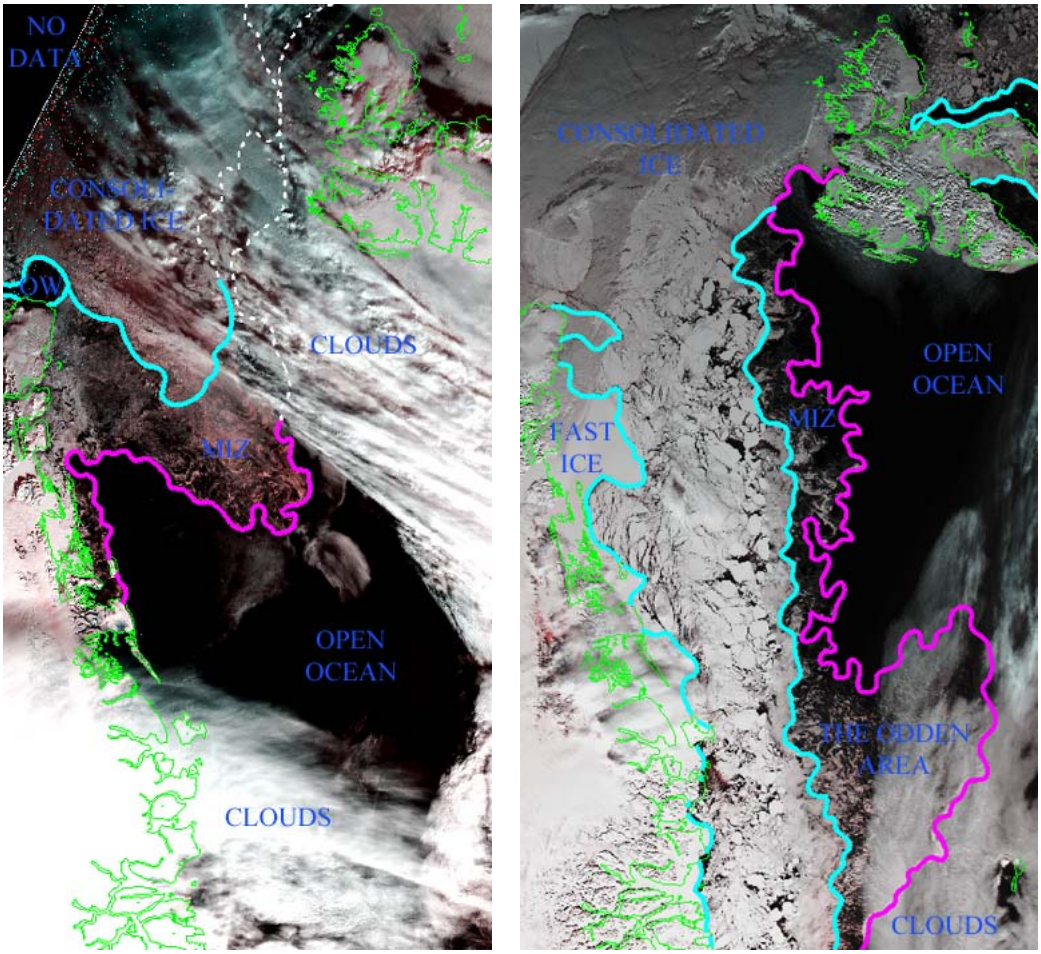

(a) 5th October 2002, 12.29 UTC (b) 15th April 2003, 14.38 UTC

Figure 5.3: NOAA visible AVHRR images including ice analysis (DMI)

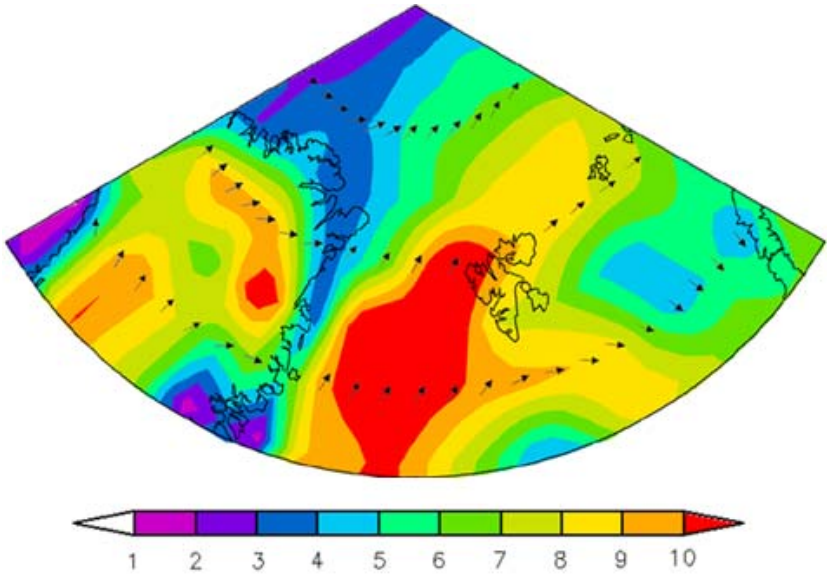

(a) Surface Winds (m/s) 7-days mean

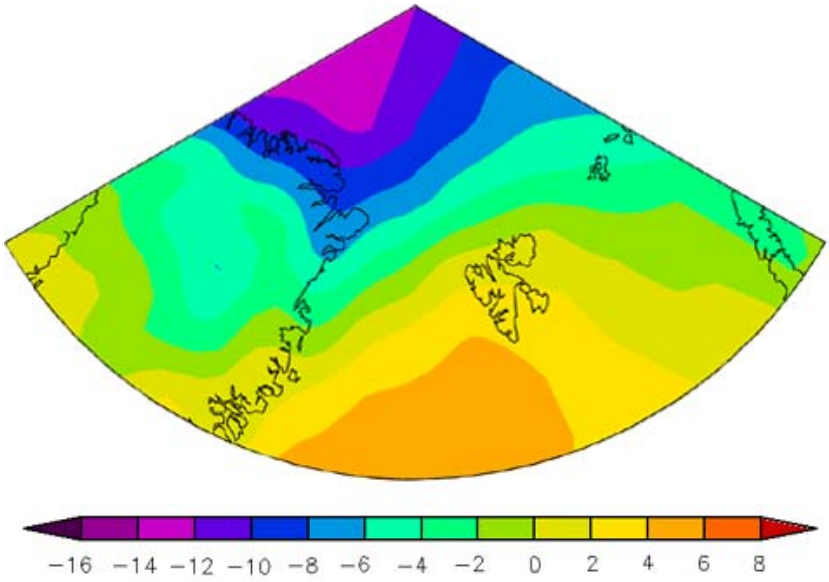

(b) Surface Temperatures (°C) 7-days mean

Figure 5.4: 6-13 October 2002 (NCEP Operational Dataset)

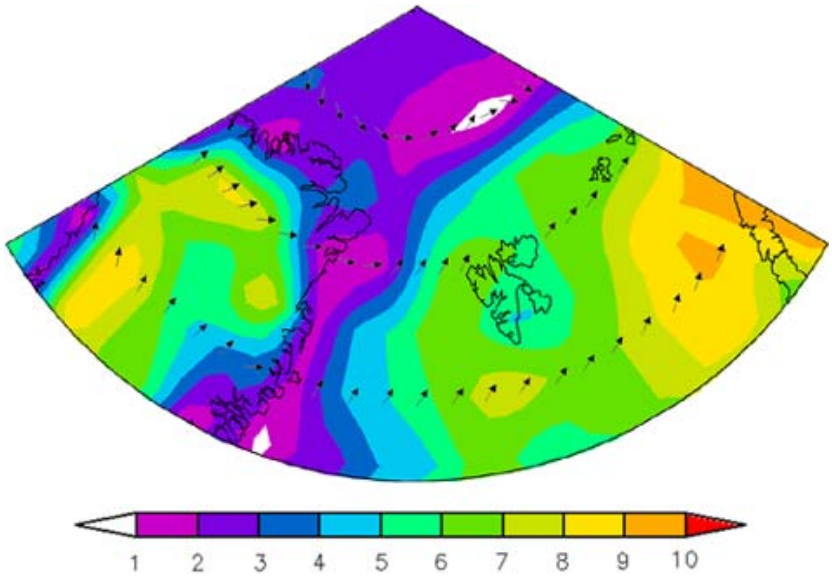

(a) Surface Winds (m/s) 7-days mean

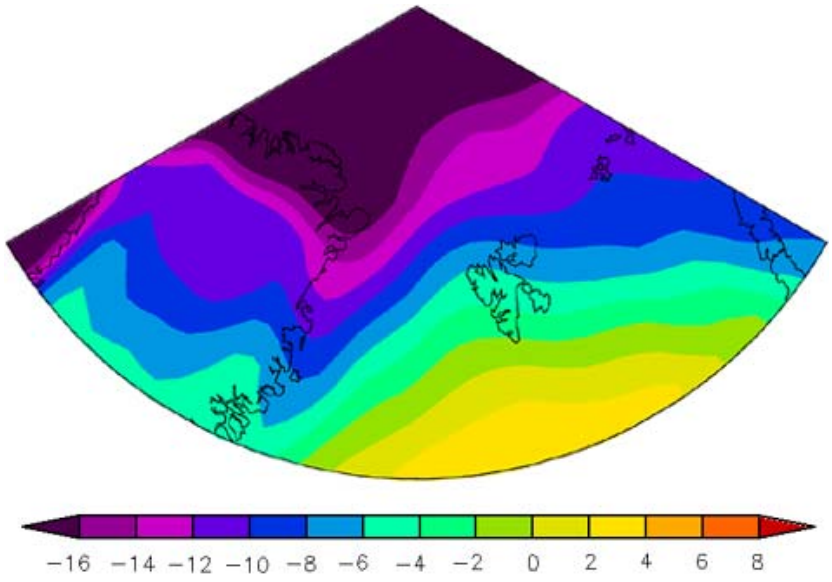

(b) Surface Temperatures (°C) 7-days mean

Figure 5.5: 9-15 April 2003 (NCEP Operational Dataset)

Chapter 6

Results

6.1 Ice Parameters Extracted from Radar Altimetry

In this section the backscatter coefficient, the peak power and the pulse peakiness are investigated, in order to see the variations over open ocean and different sea ice conditions.

Six RA-2 ground tracks are validated nearly coincident with the respective ice analyzes, see chapter 5.2. This includes, track (84) from the 6th of October 2002, tracks (97+98) from the 7th of October 2002 and tracks (312, 313 and 314) from the 15th of April 2003. The backscatter, peak power and pulse peakiness (PP) defined in chapter 4 are mapped along the respective ground tracks. Figure 6.1 maps the parameters along ground track 84, 97 and 98. In the same way, the parameters is mapped along groundtrack 312, 313 and 314 in figure 6.2. In order to compare the different parameters for a given day the maps of the different parameters have been placed next to each other. In addition, the ice edges and ice boundaries, as analyzed and described in the previous chapter 5.2, have been added to the maps.

To illustrate the characteristic scales of the parameters representative for the different areas (open ocean, MIZ, the Odden area, consolidated ice and fast ice), see chapter 5.2, they have been quantified in the tables in appendix D. The tracks have been resolved into the respective ice regimes by taking the position from the crossing points of the ice boundaries in the ice analysis and the altimeter groundtrack. Across the boundary 50 averaged waveforms is removed (25 on each side) due to the uncertainty of the ice boundaries, i.e. the NOAA image might be distorted during the processing procedure. For each parameter the mean value, the minimum value and maximum value have been calculated. In addition, the tables include the ratio of specular and diffuse waveforms expressed in percentages of the total number of waveforms. The specular and diffuse waveforms are classified using the criteria defined in chapter 4.2 ($PP \leq 1.8$ diffuse, $PP > 1.8$ specular). Track 312 contains only a small belt of open water and is not included in the analysis of open ocean, see map figure 6.2.

The analysis below are supported by additional maps, covering the periods 8-13 October 2002 and 9-14 April 2003, presented in appendix E. In these cases the ice analysis are only meant as a guide, as the ice conditions are expected to change during one week.

From the tables in appendix D it is noticed that the open ocean returns are characterized by an average backscatter coefficient 8.7 dB in October 2002 with a larger average value 11.0 dB in April 2003. In each case the interval spans about 15 dB. The difference in average backscatter is probably a result of the different wind conditions, which changes the roughness of the surface. The average peak power is the same 26.4 dB for both months, spanning a narrow interval in both cases about 3 dB, reflecting the homogeneous features of the ocean surface. The average pulse peakiness is 0.9 for both months and consists of 100% diffuse waveforms.

The *marginal ice zone* MIZ is characterized by large backscatter and peak power compared to open ocean. The average backscatter in October 2002 is 32.1 dB and a little less 25.3 dB in April 2003. The maximum backscatter is 50.4 dB in October 2002 and 45.7 dB in April 2003 both spanning large intervals, in the order 35-40 dB. The peak power in October 2002 is 47.9 dB with large spans 40.9 dB and a little less in April 2003 38.1 dB with interval on 23.5 dB. The increase in backscatter and peak power compared to open ocean is caused by the sharp contrast in scattering and reflection properties between open sea and water surfaces in the MIZ (Drinkwater, 1991). The larger backscatter values and peak power in October 2002 compared to April 2003 are probably due to the presence of new ice in October month. New ice is characterized by a smooth surface compared to older ice classes, resulting in higher nadir return signals. The ice edge does not seem to match the change in parameters in track 97 and 98, figure 6.1 (a), but the time lag between the altimeter tracks and the NOAA based ice analysis is almost 2 days. In addition, the ice analysis was based on SSM/I in that area due to clouds in the NOAA image.

The specular returns dominate the *marginal ice zone*. In October 72-100% of the return waveforms are specular. In track 84 where only 87% of the waveforms are specular returns, there is an area of low pulse peakiness near the coast, see map figure 6.1 (c). This area could be an area of less ice concentration (1-3/10) giving the wind a chance to roughen the surface, resulting in diffuse waveforms. The specular returns of the MIZ in April comprise 79-93%.

Unfortunately, only one track in figure 6.2 covers the Odden area. The average backscatter is 31.3 dB. The maximum backscatter (38.3 dB) and variability (20 dB) are less than the corresponding values of the MIZ and area of consolidated ice. The peak power for the Odden area is only slightly higher (27.8 dB), than for the open ocean, and the position of the ice edge is difficult to define based on the peak power alone, see the map in figure 6.2 (c). Even the variation of the peak power (9 dB) in the Odden area is narrow compared to the area covered by consolidated ice (see

below). The distribution of specular and diffuse waveforms is almost fifty-fifty, and the maximum pulse peakiness 7.08 is low compared to the other ice covered areas, which have maximum pulse peakiness values about 20-40. The internal ice boundary between the Odden area and the high concentrated area is very sharp. These features are also observed in the tracks covering the Odden area, see appendix E figure E.6 and E.9. The backscatter is the best indicator for the presence of the Odden area.

In the area covered by consolidated ice the average backscatter is high 35.6 dB in October 2002 and lower 25.3 dB in April 2003. The maximum backscatter for both cases is approximate 53 dB and has a large span, in the order of 50 dB. The seasonal variation in the average backscatter was also observed in the *marginal ice zone*. Once again, it can be explained by the presence of new ice in the beginning of October, but also reflects the scattering properties of the snow present on the ice in April. Experiments show a reduction in backscatter at normal incidence from 20 to 5 dB by adding 2.5 cm snow (Beaven et al., 1995). The features of the area of consolidated ice and the *marginal ice zone* is difficult to distinguish from each other in the altimeter parameters. The peak power for October and April is almost identical with average value 28.0 dB, maximum value 48.0 dB and a large variation about 40 dB.

The pulse peakiness parameter from the area covered by consolidated ice exhibited 100% specular returns in October 2002 and a little less, 87-92%, in April 2003. The differences can be explained by the floe sizes. In October 2002 the floes present are of less size than the floes in April 2003. As most of the diffuse waveforms in areas of high concentration originates from large floes, large enough in the sense to contain successive altimeter footprints, the seasonal variation in the number of diffuse waveforms can be explained by floe sizes. The seasonal variation in diffuse waveforms was also identified in the works of Peacock and Laxon (2001). The pulse peakiness is highest in track 312 (the northernmost track) and lower in track 313 and 314 located more to the south, see figure 6.2, reflecting the effect of the reduced size of the ice floes with decreasing latitude, i.e. due to inter floe collisions. This is also reflected in the maps of April 2003 in appendix E. The ice floe to be included in the analysis in section 6.2 is identified in the maps, figure E.8 and E.9.

Only two of the three tracks in figure 6.2 maps areas of fast ice. All three parameters originating from the fast ice are comparable with the values of open ocean. The areas of fast ice are bounding up to areas covered by consolidated ice and the ice boundaries are easy to define.

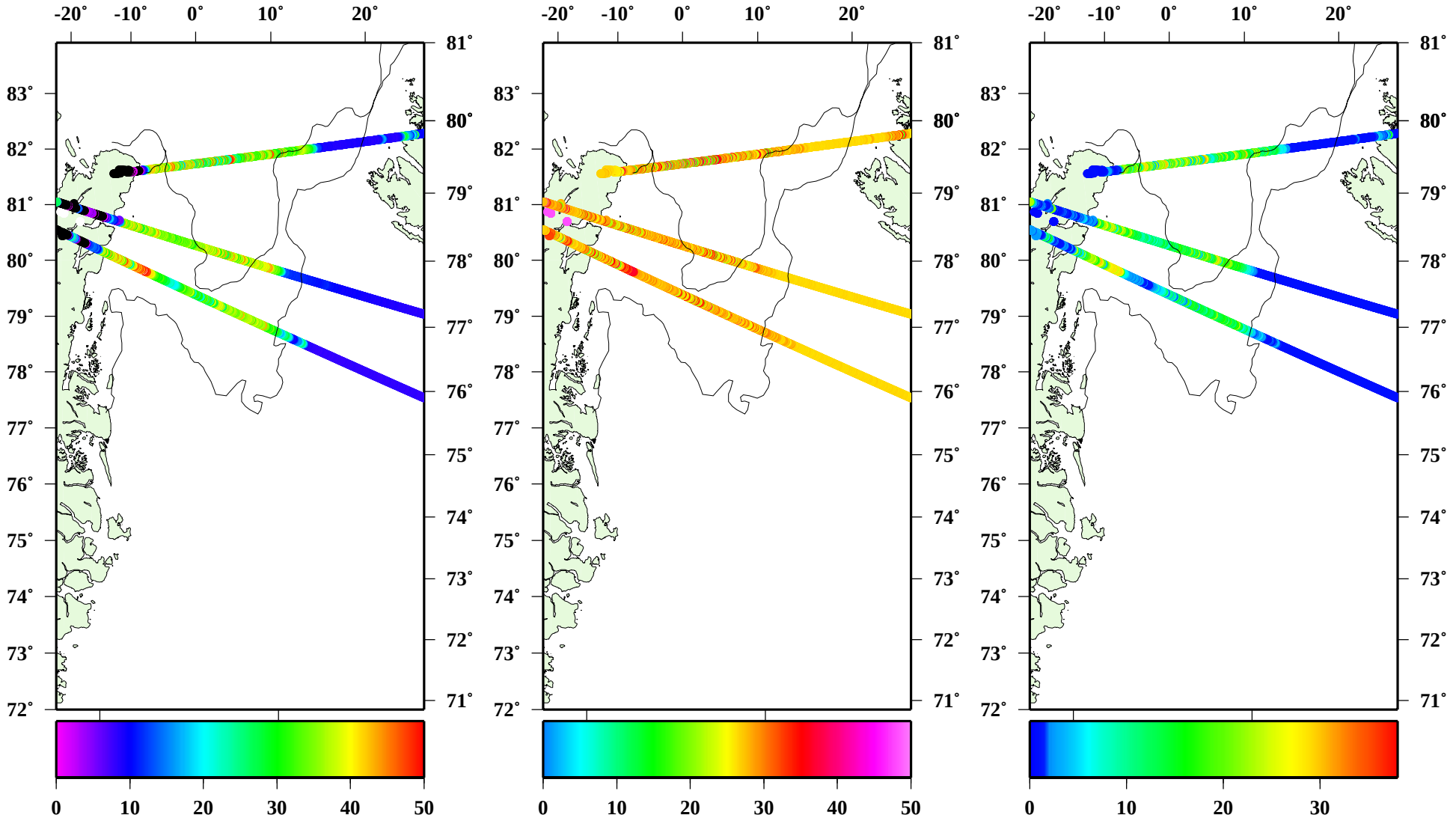

(a) Backscatter (b) Peak Power (c) Pulse Peakiness

Figure 6.1: ENVISAT altimeter groundtracks the 6th and the 7th of October 2002. The northernmost track is orbit 97, the track in the middle is orbit 98 and the southernmost track is orbit 84. The ice analysis is based on NOAA data from October the 5th, 2002.

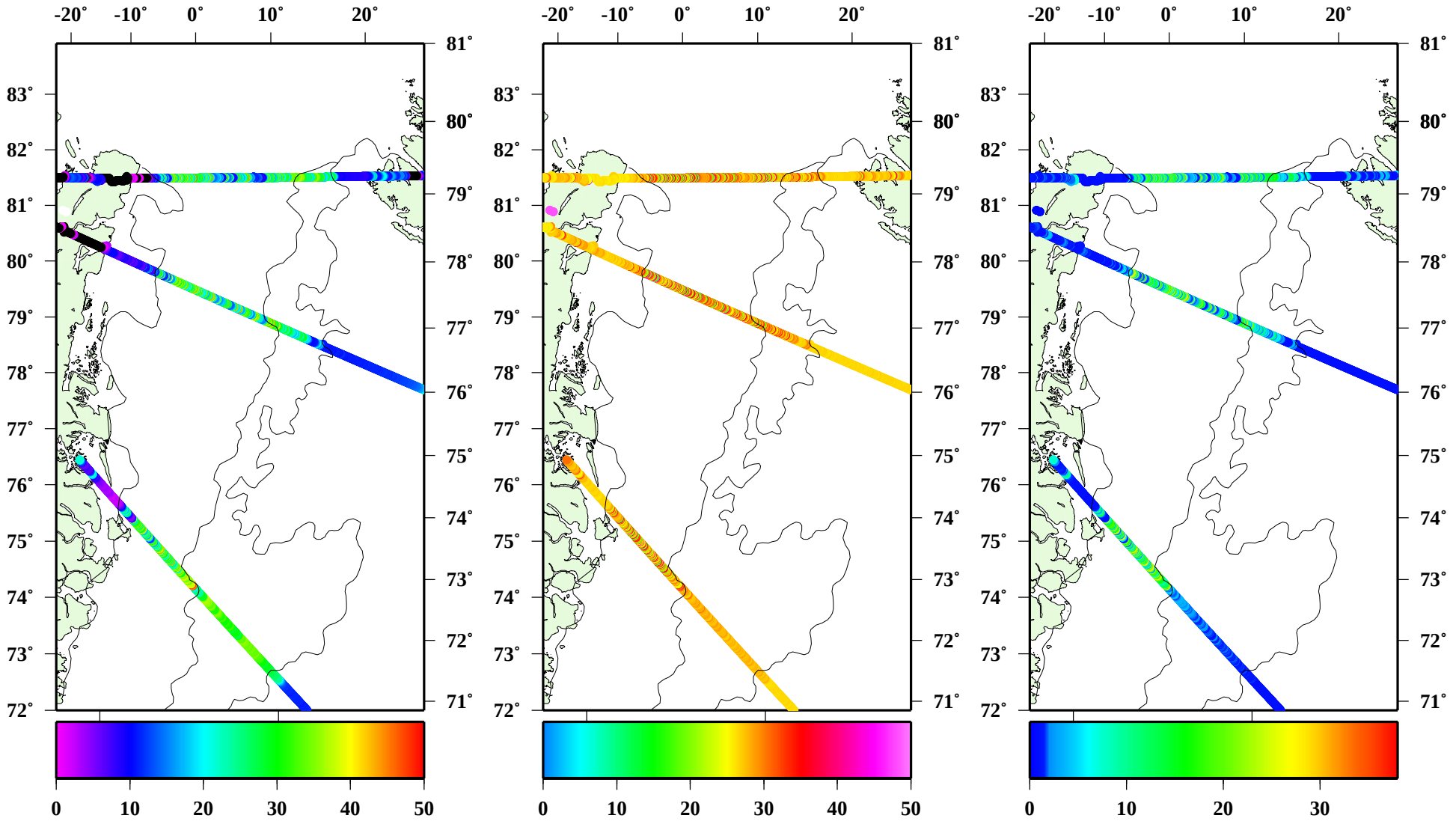

(a) Backscatter (b) Peak Power (c) Pulse Peakiness

Figure 6.2: ENVISAT altimeter groundtracks the 15th of April 2003. The northernmost track is orbit 312, the track in the middle is orbit 313 and the southernmost track is orbit 314. The ice analysis is based on NOAA data also from April the 15th, 2003.

6.2 Sea Ice Thickness

In the following, the method to estimate sea ice thicknesses using satellite altimetry, as described in chapter 4.2, is used.

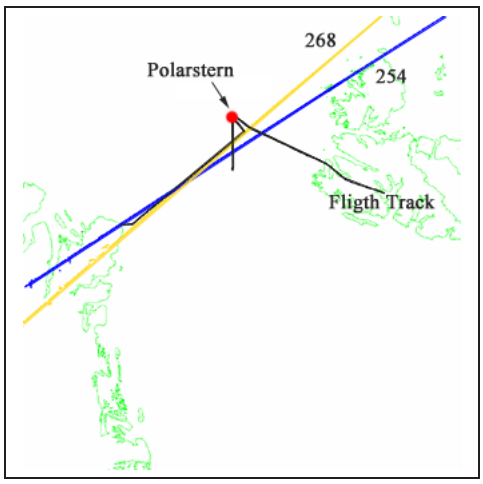

Figure 6.3: Groundtracks of ENVISAT the 11th of April (blue) and the 12th of April (yellow). Flight track the 11th of April (black). Position of Polarstern the 11th of April (red dot)

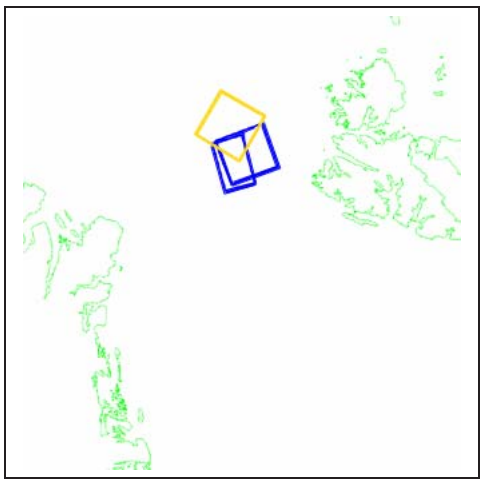

Figure 6.4: Position of SAR/ASAR frames the 11th of April (blue) and the 12th of April (yellow)

The analysis is based on two altimeter groundtracks, orbit 254 (the 11th April 2003, 16.16 UTC) and 268 (the 12th April 2003, 15.44 UTC). Groundtack 268 is almost identical to the flight track from the 11th April 2003, where freeboard measurement by laser altimetry was conducted by the National Survey and Cadastre (KMS), see figure 6.3. In favor to identify the ice types present, the SAR/ASAR scenes described in chapter 5 are used. The altimeter tracks investigated are reduced to the areas overlapped by the SAR/ASAR frames, see figure 6.4.

The ice condition in the area is of high concentration (7-9/10) and consists of large floes, (larger than 20 km) embedded thin ice types (new and young ice). These conditions are confirmed by photographs taken during the underflight. In the frames of SAR/ASAR a large ice floe, 60 km long and 30 km across, is situated, see figure 6.5 (a) and 6.6 (a). As the floe is large enough to contain successive footprints of the altimeter (about 150 averaged waveforms), the optimal conditions are set for altimeter studies of the ice thickness.

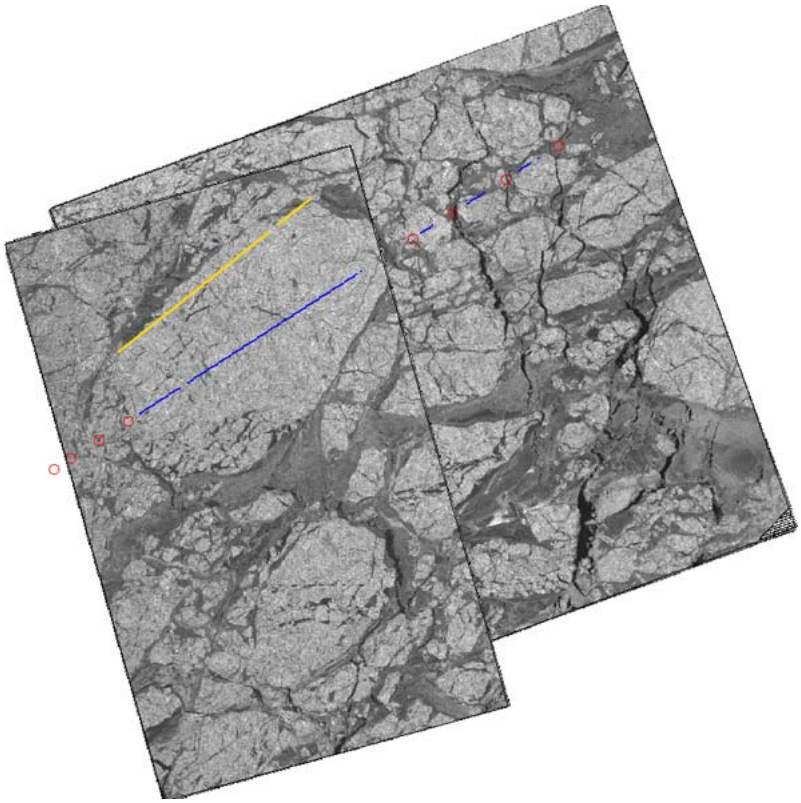

(a) ENVISAT ASAR image 11.17 UTC placed on top of Radarsat SAR image 06.58 UTC and altimeter ground track 254 16.16 UTC (blue lines and red circles). Underflight yellow line. (Source: Radarsat CSA, ENVISAT ESA and DMI).

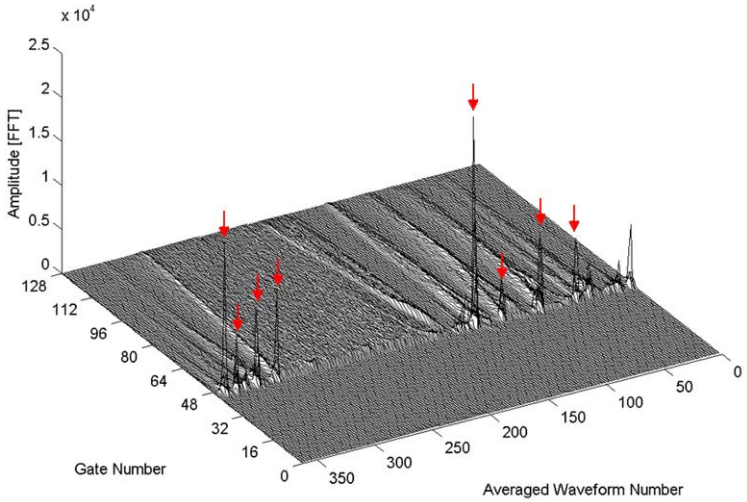

(b) Stacked waveforms of groundtrack 254 16.16 UTC

Figure 6.5: Presentation of nearly coincident ASAR/SAR images (a) and averaged altimeter waveforms stacked in the along-track time domain (b), 11th of April 2003

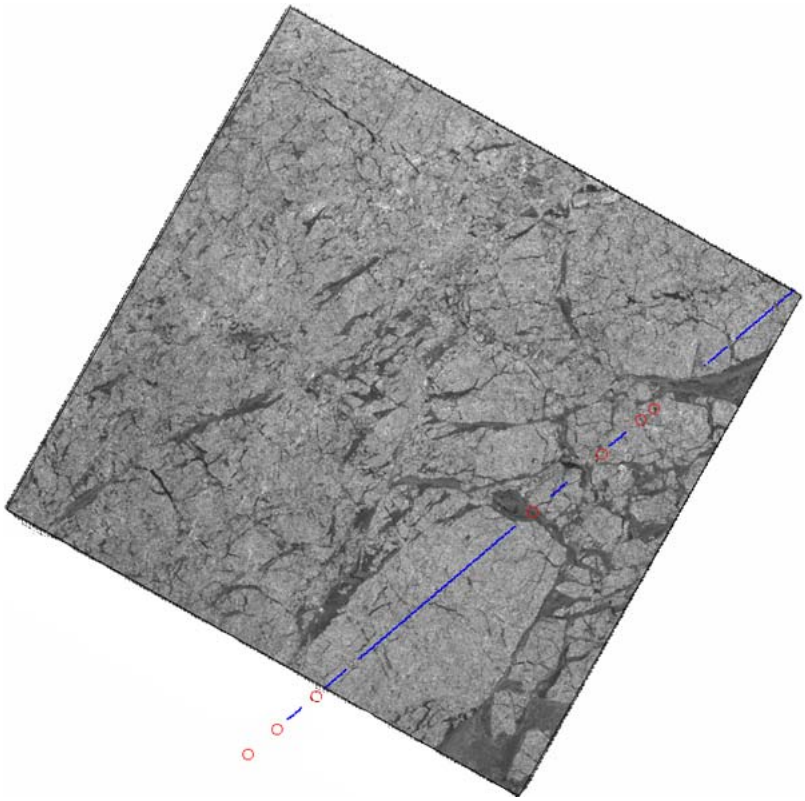

(a) Radarsat SAR image 16.29 UTC and altimeter ground track (blue line and red circles) 268 15.44 UTC (Source: Radarsat CSA and DMI).

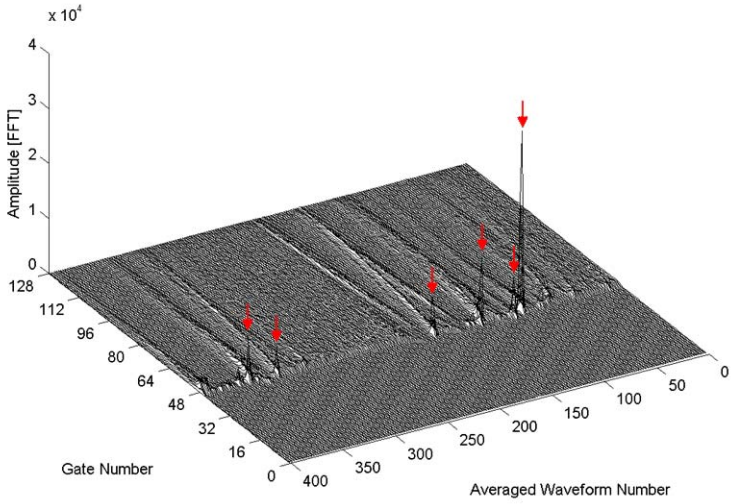

(b) Stacked waveforms of groundtrack 268 15.44 UTC

Figure 6.6: Presentation of nearly coincident ASAR/SAR images (a) and averaged altimeter waveforms stacked in the along-track time domain (b), 12th of April 2003

In figure 6.5 (b) and 6.6 (b) the averaged waveforms are stacked in the along-track time domain and corresponds to the ground tracks in figure 6.5 (a) and 6.6 (a). It is observed that the waveforms over the ice floe are diffuse. In the vicinity of the ice floe thinner ice types and open water result in specular returns. The average peak power over the ice floe is about 27 dB spanning over the range 26-30 dB, a mean value and interval just slightly above that of open ocean, see chapter 6.1. 83% of the averaged waveforms from the ice floe track 254, and 90% of the averaged waveforms from track 268 have a pulse peakiness less than or equal to 1.8. The maximum peak power observed along the entire subsection of both tracks are 42.3 dB.

6.2.1 Estimation of sea ice thickness

The freeboard is calculated as a function of averaged waveform number using the method described in chapter 4.2. Figure 6.7 (a) and (b) show the freeboard and corresponding pulse peakiness from groundtrack 254 and 268.

The freeboard takes a negative value. This is explained by the deviations of the sea surface from the geoid (Δ h in equation 4.2). As the peaked signals (PP>1.8) are assumed to originate from open water or new ice, see chapter 3.3, in between the ice floes the value of the freeboard taken at the peaked signals should represent the sea level. In this manner, a mean sea level can be found and the freeboard can be corrected for the deviations from the geoid.

In the illustrations large negative values of the freeboard is seen in the order of -5 to -25 m, primarily in the vicinity of the ice floe. The tracker is locked at the peaked targets and results in large fluctuations and false heights in the altimeter return signal known as snagging. To correct for the effect of snagging a reprocessing of data is necessary (Peacock and Laxon, 2001) and has not been possible within the frames of this project.

The processing failure makes the task to estimate the sea ice thickness difficult, as it is difficult to locate the true heights for the peaked waveforms. To circumvent the problems concerning the tracking failure, the most peaked signals in the vicinity of the floe, were manually selected. These signals should match the true heights and not be affected by false heights due to the *peaked signal locking*. In figure 6.5 and 6.6 the selected peaked signals are shown. In the lower illustrations, the peaked waveforms are marked by red arrows. In the upper images, the footprints of the peaked waveforms are marked by red circles scaled to the approximate size of the *footprint limited area* (1.6 km in diameter). As observed in the SAR image the peaked waveforms are located above thin ice types (new and young ice). From the SAR image it seems as only one of the peaked signals contains open water, which happens to be number 113 along track 254 and 132 along track 268. These two peaks also correspond to the lowest freeboards, see tables 6.8 and 6.9, and is defined to represent the mean sea level.

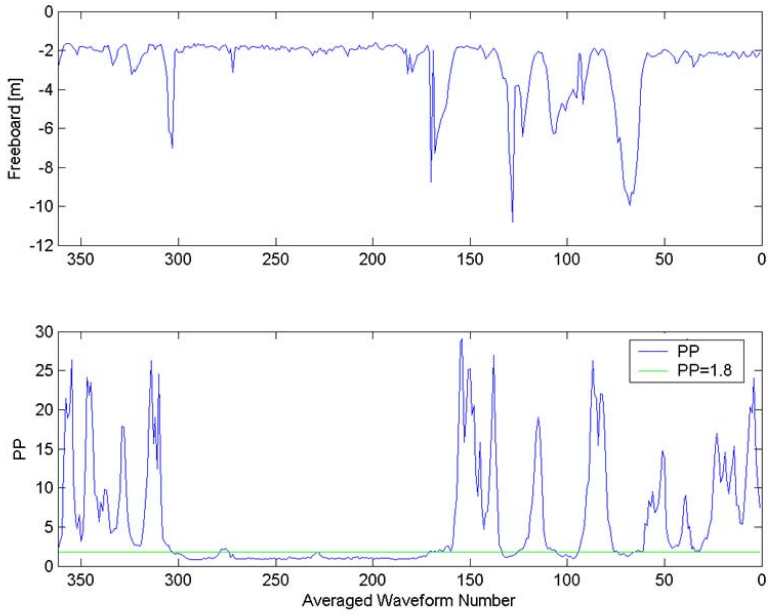

(a) Groundtrack 254

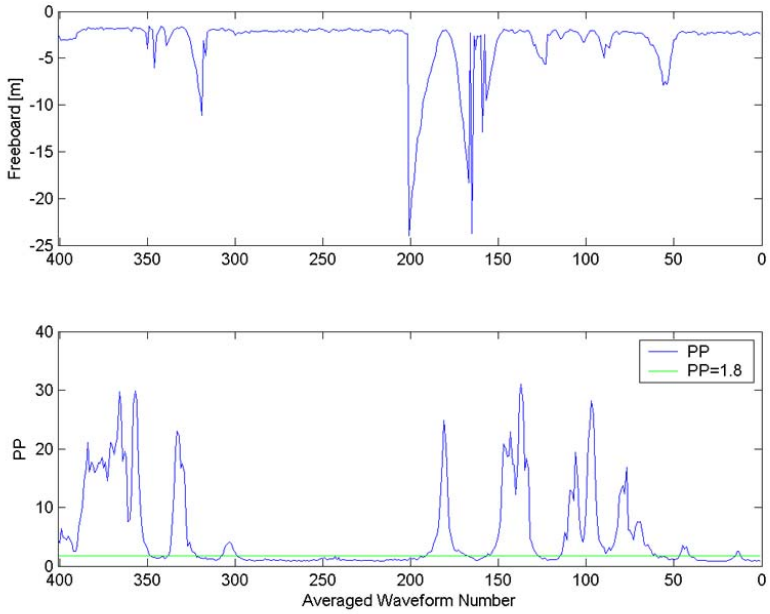

(b) Groundtrack 268

Figure 6.7: Plots of the freeboard and corresponding pulse peakiness parameter (PP)

Track 254	
Peak	Freeboard [m]
49	-1.997
81	-2.008
113	-2.125
137	-2.000
309	-1.707
327	-1.743
344	-1.980
354	-1.875

Figure 6.8: Freeboard of peaked signals of RA-2 subtracks 254

Track 268	
Peak	Freeboard [m]
96	-2.044
105	-2.211
132	-2.285
179	-2.211
328	-1.973
355	-1.818
375	-1.947

Figure 6.9: Freeboard of peaked signals of RA-2 subtracks 268

The freeboard for the diffuse signals are subtracted from the mean sea level giving a mean freeboard. The diffuse waveforms along the subtracks are sorted using the criteria of the pulse peakiness to be less than or equal to 1.8. The results of the freeboards are plotted in figure 6.10 (a) and (b) as a function of the along-track averaged waveforms. The red circles represent the peaked signals and blue pluses refer to the freeboard of the diffuse returns. Unfortunately, some of the erroneous locked signals is interpreted as diffuse returns and there is still a false height present in the data set. This has been filtered out requiring the freeboard to be larger than zero. By implementing this criteria the mean freeboard of the diffuse waveforms are 0.26 m for track 254 and 0.22 m for track 268. Converting the freeboard to thicknesses, by use of equation 4.3 with R=4.89, the results are

- 1.53 m for track 254
- 1.30 m for track 268

To compare the results with the laser altimeter measurements made the 11th of April 2003, a subtrack covering the same ice floe (see the yellow line in figure 6.5) has been selected. The average freeboard of the subtrack is 0.45 m corresponding to a thickness of 2.65 m.

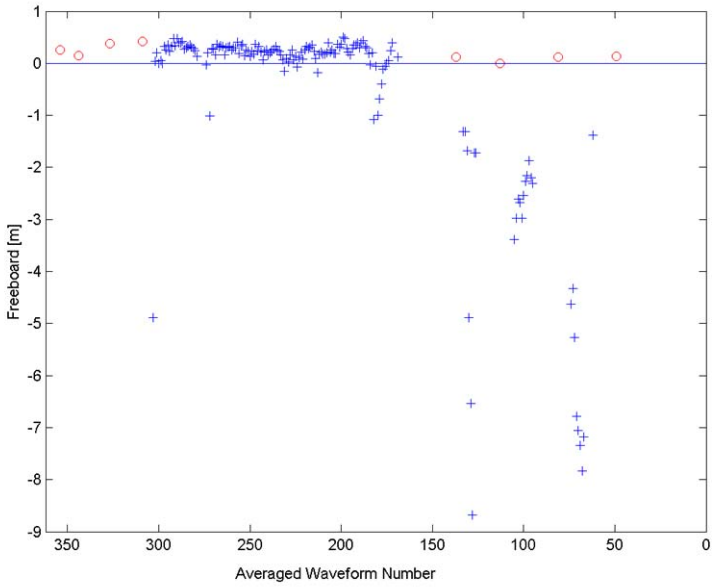

(a) Groundtrack 254

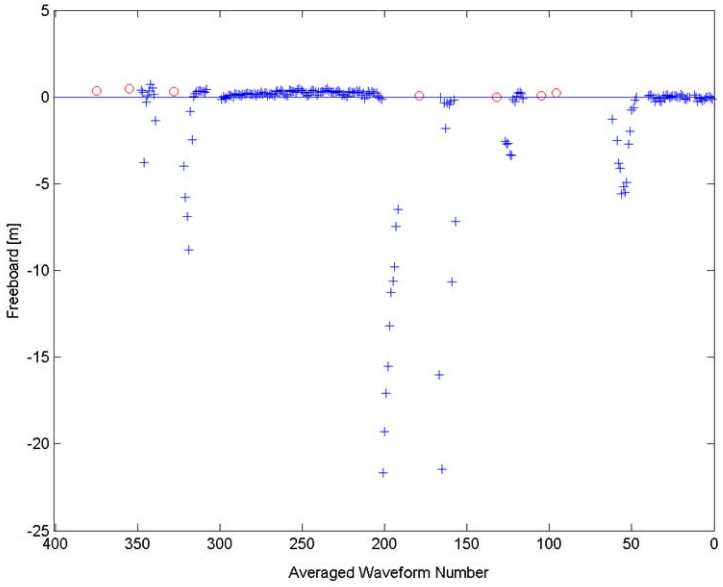

(b) Groundtrack 268

Figure 6.10: Plots of freeboards where the red circles represent the peaked signals and blue pluses refer to the freeboard of the diffuse returns.

6.3 Discussion of Sea Ice Thickness

The ice thicknesses observed above are all within reasonable scales. The results based on the radar altimeter are characteristic for first year ice floes. The differences in freeboard and thicknesses between the space borne radar altimeter and the airborne laser altimeter seem to be large. The freeboard measured by laser altimetry is almost twice as large as the freeboard measured by radar altimetry. It is though difficult to compare the thicknesses, as the RA-2 ground tracks are not coincident to the flight track, see figure 6.3. The reason to compare is due to the fact that all tracks cover the same ice floe.

In the method used to find the sea ice thickness there are some uncertainties to take into consideration. Some of these are discussed in the following.

First of all, the thicknesses are based on freeboard measurements. Thus, the error estimate from the freeboard results in even larger errors on the thicknesses, i.e. 2 cm error on the freeboard corresponds to 12 cm error on the thickness.

The mean sea level estimated by the peaked waveform is based on a very sparse amount of data due to *signal locking*. This results in errors on the mean sea level, affecting the freeboards and ice thicknesses. The mean sea level could be new ice, and not open water as assumed, adding another 5-10 cm to the thickness.

Another subject to be taken precautionary is the influence of snow layers upon the ice. Two important factors have to be taken into consideration; the radar interaction with surface and the mechanical snow load.

In the assumptions made in chapter 4.2 the return echo is believed to originate from the snow surface. Actually, this is the case for airborne laser altimetry (personal communication: S. M. Hvidegaard). In case of space borne radar altimetry it is unknown whether the backscatter originates from the snow surface or snow-ice interface. If the thicknesses are calculated based on the wrong assumption it may result in large errors on the sea ice thickness.

In the work carried out by Peacock and Laxon (2001) the reflection is assumed to originate from the snow-ice boundary outside the melt season. The assumption is based on experiments made in a tank of saline ice at the Cold Region Research and Engineering Laboratory (CRREL) (Beaven et al., 1995). By adding 21 cm snow to the bare ice the backscatter was shown to be dominated by the snow-ice interface.

According to general scattering theory the surface scattering depends on the dielectric properties of sea ice (salinity and temperature), the snow thickness, the dielectric properties of the snow, the snow grain size, the snow density and the water volume content in the snow. Volume scattering is neglected in the total scattering budget at nadir incidence angles. Theoretical models indicate that nadir volume scattering is

-10 to -5 dB in multiyear ice and even less in first year ice (Personal communication: R. Tonboe).

In order to investigate the scattering mechanisms over snow covered sea ice floes a transponder could be used to define the exact ice surface including the snow and ice. The transponder has already shown to be valuable to define the snow surface of the Greenland ice sheets (Haardeng-Pedersen et al., 1998).

But also a further knowledge to the seasonal and regional changes in snow thickness is needed to improve the results. In the model used in this thesis the snow thickness is implemented in the R-factor, see chapter 4.2. The R-factor is based on snow conditions in the *Arctic Basin* (Wadhams et al., 1992) and the seasonal variations included. The R-factor used here corresponds to snow depths of about 35 cm. On a cruise in north east Greenland in April 2003 Polarstern observed snow depths ranging from 0.05 to 0.30 m on thick ice (Haas et al., 2003). Due to Wadhams et al. (1992) a snow thickness less than 35 cm using the same snow density corresponds to a large R-factor, e.g. a snow thickness of 10 cm have R=7.07 corresponding to increased ice thicknesses. The corrected thicknesses from the previous section is for track 254 2.10 m and for track 268 1.78 m.

Adding all the above contributions to the error estimates it appears that the sea ice thicknesses in this study are underestimated.

Chapter 7

Conclusions

The variations of the three parameters (sea ice backscatter, peak power, and pulse peakiness) was studied in order to determine the extent of sea ice. Over the ocean all three parameters are homogeneous and represented by diffuse waveforms. The backscatter takes its average value in the range 8-11 dB and the average peak power is 27 dB. In this study all three parameters show large variability and a large maximum value over the *marginal ice zone* and areas covered by consolidated ice. The maximum backscatter is 53 dB and the maximum peak power 48 dB. In case of small ice floes another identified feature, is the fact that the pulse peakiness and backscatter coefficient can be used to distinguish areas of low ice concentration from areas of higher concentrations. In areas of high ice concentrations the pulse peakiness reflects the presence of large ice floes by the percentage of diffuse waveforms, in that a high percentage reflects the presence of many large ice floes. Over fast ice the waveform is diffuse and ocean-like. The backscatter coefficient proves to be a good indicator for the ice edge, specifically in the Odden area, where the other parameters fail.

In particular, the sea ice backscatter, included in the geophysical data record (GDR), turns out to be sensitive to the ice edge and other features within the ice such as large ice floes and areas of fast ice. Altimetry data has the potential to detect sea ice, but is not recommended for operational use when only based on ENVISAT data. The radar altimeter is only a one dimensional reproduction of the surface and the daily coverage is sparse. In north east Greenland only 3-5 satellite passes occur per day. If the tracks are summed over a week or a cycle (35 days) it may be worthwhile to use for an ice analysis. On the other hand for such long time spans the sea ice has drifted and the information is outdated. To produce useful maps, a more dense spaced net of ground tracks is needed, for example by use of other altimeter borne satellites.

Radar altimetry may contribute additional ice information to other remote sensor data, where they fail. Particularly ice information extracted by radar altimetry could be integrated with passive microwave images to remove false sea ice targets due to water vapor in the atmosphere and wind induced surface roughness. The

altimetry data may also be used to fill in where NOAA AVHRR images fail due to cloud cover or where SAR/ASAR images can not be interpreted due to wind roughened surfaces.

The sea ice thicknesses of two subtracks, from the 11th and 12th of April 2003, have been estimated. The ice thicknesses observed are within reasonable scales and in the order of the thickness characteristic for first year ice (<2 m). As a result of error estimations, the thicknesses are expected to be underestimated. The ENVISAT sea ice tracker is successful to keep the leading edge of the waveform within the range window, but the tracking system generates large erroneous height errors due to peaked signal locking. In future work a reprocessing of data is recommended (Peacock and Laxon, 2001). In addition, the method demands areas of large floe sizes, that are large enough to contain successive altimeter footprints, to generate diffuse waveforms. This is impossible in the Fram Strait in October, where few large ice floes are present.

Additional information of the scattering mechanisms which influence the radar interaction with the snow covered ice floe surfaces, is needed to improve the model to estimate the sea ice thickness. In particular, it is essential to know if the dominating scattering originates from the snow surface or the snow-ice surface. This can be investigated in future field studies in the sea ice environment by use of a transponder, which was tested twice during this study. From the data analysis, it is unsure whether the transponder worked. If the transponder is taken to the sea ice, it is recommended to place the transponder in the middle of a large floe, for example a floe large enough to contain successive altimeter footprints, in order to see the transponder signal in the return signal.

The results of the sea ice thickness are very important. It is not possible on the basis of this study to monitor the thickness over large spatial or time spans. But it is the only method known to date to determine sea ice thicknesses based on *space borne radar altimetry* (Peacock and Laxon, 2001).

Chapter 8

Epilogue

This master thesis has been very challenging and interesting to accomplish. Especially the variety of the work and to be in front of the science has been very engaging to me. There are so many interesting aspects to the field and during the process it was necessary to exclude parts of the work.

One topic I found necessary to exclude from this thesis was the implementation of a theoretical backscatter model which main purpose was to study the scattering mechanisms at normal incidence generated by the snow surface and the snow-ice surface. The model was developed for a snow layer added on top on an ice layer to see how the surface scattering of the snow and snow-ice surfaces depend on the dielectric properties of sea ice (salinity and temperature), the snow thickness, the dielectric properties of the snow, the snow grain size, the snow density and the water volume content in the snow. The project turned out to be too ambitious and demanded at least 2-4 weeks full time work to produce some useful results.

Another ambition was to implement the processing of the sea ice thickness over larger spatial and time scales. This was not possible as I first received the data from ENVISAT in early December. To summarize, I have gained an insight into the techniques by use of radar altimetry to study the sea ice and I am looking forward to future works in the field.

Bibliography

Beaven, S., Lockhart, G., Gogineni, S., Hosseinmostafa, A., Jezek, K., Gow, A., Perovich, D., Fung, A., Tjuatja, S., 1995. *Laboratory measurements of radar backscatter from bare and snow-covered saline ice sheets.* Int. J. Remote Sensing, 16 (5), 851–876.

Brown, G., 1977. *The Average Impulse Response of a Rough Surface and Its Applications.* IEEE Journal of oceanic Engineering, 25 (1), 67–74.

Chelton, D., McGabe, P., 1985. *A review of satellite altimeter measurement of sea surface wind speed: with a proposed new algorithm.* Journal of Geophysical Research, 90, 4707–4720.

Chelton, D. B., 1988. Woce/nasa altimeter algorithm workshop. U.S. WOCE Technical Report 2, U.S. Planning Office for WOCE, College Station, TX 1988.
URL `oceanesip.jpl.nasa.gov/sealevel/wocealt87.pdf`

Comiso, J., Whadams, P., Krabill, W., Swift, R., Crawford, J., III, W. T., 1985. *Top/Bottom Multisensor Remote Sensing of Arctic Sea Ice.* Journal of Geophysical Research, 96, 4707–4720.

Drinkwater, M., 1991. *K_u Band Airborne Radar Altimeter Observations of Marginal Sea Ice During the 1984 Marginal Ice Zone Experiment.* Journal of Geophysical Research, 96 (C3), 4555–4572.

Dwyer, R., Godin, R., 1980. Determining sea ice boundaries and ice roughness using geos-3 altimeter data. Contractor Report 156862, NASA.

Elbek, B., 1995. *Optik.* Niels Bohr Institutet.

ENVISAT RA2/MWR Product Handbook, 2002. European Space Agency, 1st Edition.
URL `www.envisat.esa.int/dataproducts`

Fetterer, F., Drinkwater, M., Jezek, K., S.W.C.Laxon, Onstott, R., Ulander, L., 1992. *Sea Ice Altimetry.* Geophysical Monograph, 68, 111–135.

Forsberg, R., Keller, K., Hvidegaard, S., Olesen, A., 2003. Esag-2002: European airborne gravity and lidar survey in the arctic ocean. Technical Report 21, National Survey and Cadastre, Denmark.

Fu, L. L., Cazenave, A., 2001. *Satellite Altimetry and Earth Sciences: A Handbook of Techniques and Applications*. Academic Press.

Haardeng-Pedersen, G., Keller, K., Tscherning, C., Gundestrup, N., 1998. *Modeling the signature of a transponder in altimeter return data and determination of the reflection surface of the ice cap near the GRIP camp, Greenland*. Journal of Glaciology, 44 (148), 625–633.

Haas, C., Alexandrov, V., Kern, S., Lieser, J., Lobach, J., Martin, T., Pfaffling, A., Willmes, S., 2003. Sea ice remote sensing, thickness profiling, and ice and snow analyses during polarstern cruise ark 19/1/cryovex2003 in the barents sea and fram strait, february 28 - april 24, 2003: Cruise report. Tech. rep.
URL `www.awi-bremerhaven.de/Modelling/SEAICE/Ark19/CruiseReport.pdf`

Haas, C., Gerland, S., Eicken, H., Miller, H., 1997. *Comparison of sea-ice thickness measurements under summer and winter conditions in the Arctic using a small electromagnetic induction device*. Geophysics, 62 (3).

Hawkins, J., Lybanon, M., 1989. *GEOSAT Altimeter Sea-Ice Mapping*. IEEE Journal of Oceanic Engineering, 14 (2).

Hvidegaard, S. M., Forsberg, R., 2002. *Sea-ice thickness from airborne laser altimetry over the Artic Ocean north of Greenland*. Geophysical Research Letters, 29 (20).

Jacobsen, S. M., 2001. Kinematisk gps og laseraltimetri til bestemmelse af havisens tykkelse i et område nord for grønland. Speciale, Københavns Universitet, Geofysisk Afdeling.

Knudsen, P., Andersen, O., Tscherning, C., 1992. *Altimetric gravity anomalies in the Norwegian-Greenland sea - preliminary results from the ERS-1 35 days repeat mission*. Geophysical Research Letters, 19 (17), 1795–1798.

Laxon, S., 1990. *Seasonal and inter-annual variations in Antarctica sea ice extent as mapped by Geosat altimetry*. Geophysical Research Letters, 17 (10), 1553–1556.

Laxon, S., 1994a. *Sea ice altimeter processing scheme at the EODC*. Int. J. Remote Sensing, 15 (4), 915–924.

Laxon, S., 1994b. *Sea ice extent mapping using the ERS-1 radar altimeter*. EARSel Advances in Remote Sensing, 3 (2 - XII), 112–116.

Laxon, S., Rapley, C., 1987. *Radar Altimeter Data Quality Flagging*. Advances in Space Research, 7 (11), 315–318.

Maykut, G. A., Untersteiner, N., 1971. *Some Results from a Time-Dependent Thermodynamic Model of Sea Ice*. Journal of Geophysical Research, 76 (6), 1550–1575.

Peacock, N., Laxon, S., 2001. *Determination of Sea Ice Thickness in the Arctic Ocean from ERS Altimetry*. submitted to Journal of Geophysical Research.

Roca, M., Jackson, H., Celani, C., 2002. Ra-2 sigma-0 absolute calibration. In: Proceedings of ENVISAT Validation Workshop. p. 16.

Scharroo, R., 2002. A decade of ers satellite orbits and altimetry. Ph.D. dissertation, DELFT University of Technology.

Schmidt, T., Hansen, C., 2003. *Fram Strait ice export during the 19th and 20th centuries reconstructed from a multi-year sea-ice index from Southwestern Greenland.* Journal of Climate, 16, 2782–2791.

Skourup, H., 2002. *En undersøgelse af havisens udbredelse på Grønlands Østkyst i august og september måned for perioden 1893-2002*, 3.
URL `www.gfy.ku.dk/ hsk`

Strawbridge, F., Laxon, S., 1994. *ERS-1 Altimeter fast delivery data quality flagging over land surfaces.* Geophysical Research Letters, 21 (18), 1995–1998.

Ulaby, F. T., Moore, R., Fung, A., 1981. *Microwave Remote Sensing, Vol. II: Radar Remote Sensing and Surface Scattering Theory.* Vol. I: Fundamentals and Radiometry. Artech House Int.

Ulaby, F. T., Moore, R., Fung, A., 1982. *Microwave Remote Sensing.* Vol. II: Radar Remote Sensing and Surface Scattering Theory. Artech House Int.

Ulander, L. M., 1987. *Interpretation of Seasat radar-altimeter data over sea ice using near-simultaneous SAR imagery.* Int. J. Remote Sensing, 8 (11), 1679–1686.

Ulander, L. M., Carlström, A., 1991. Radar backscatter signatures of baltic sea ice. In: Proceedings of the IGARSS'91. European Space Agency, pp. 1215–1218.

Wadhams, P., Comiso, J. C., 1992. *The Ice Thickness Distribution Inferred Using Remote Sensing Techniques.* Geophysical Monograph, 68, 375–383.

Wadhams, P., III, W. T., Krabill, W., Swift, R., Comiso, J., Davis, N., 1992. *Relationship Between Sea Ice Freeboard and Draft in the Arctic Basin, and Implications for Ice Thickness Monitoring.* Journal of Geophysical Research, 97 (C12), 20,325–20,334.

World Meteorological Organization (1970), 1970. Wmo sea-ice nomenclature. TP 145 259, World Meteorological Organization.

Web Links

The links have been updated the 26nd of March 2003.

CryoSat:
www.esa.int/export/esaLP/cryosat.html

CryoVex:
www.cryovex.dk

Currents:
carto.eu.org/article2412.html

DORIS:
www.jason.oceanobs.com/html/doris

ENVISAT:
www.envisat.esa.int

Arctic Gravity Project (ArcGP):
earth-info.nima.mil/GandG/agp

NCEP Operational Dataset:
www.cdc.noaa.gov/HistData

PRARE:
op.gfz-potsdam.de/prare/index_PRARE.html

Appendix A

Characteristics of ENVISAT

- **Electromagnetic Spectrum - The Microwave Region**
- **Footprint Area - Plane Surface**
- **Antenna Gain Pattern**
- **Altimeter Borne Missions**

Electromagnetic Spectrum - The Microwave Region

The wavelength of microwaves are in the range 1 mm to 1 m. Microwaves are further divided into different frequency (wavelength) bands:

- P band: 0.3 - 1 GHz (30 - 100 cm)
- L band: 1 - 2 GHz (15 - 30 cm)
- S band: 2 - 4 GHz (7.5 - 15 cm)
- C band: 4 - 8 GHz (3.8 - 7.5 cm)
- X band: 8 - 12.5 GHz (2.4 - 3.8 cm)
- Ku band: 12.5 - 18 GHz (1.7 - 2.4 cm)
- K band: 18 - 26.5 GHz (1.1 - 1.7 cm)
- Ka band: 26.5 - 40 GHz (0.75 - 1.1 cm)

Footprint Area - Plane Surface

The following have been adapted from Fu and Cazenave (2001), chapter 1.

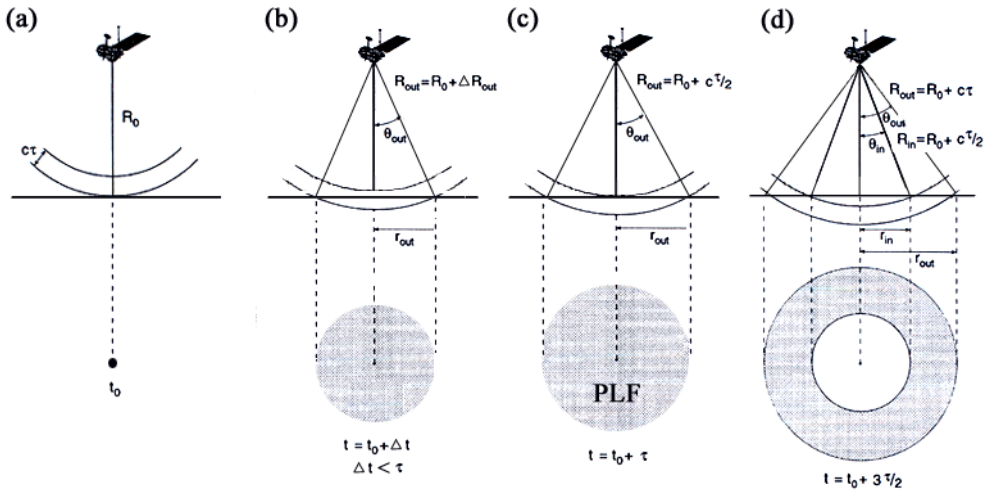

Figure A.1: The expansion of the pulse and the corresponding footprint area (Fu and Cazenave, 2001).

The footprint area for one pulse on a plane surface is given by simple geometry, see figure A.1. By use of Pythagora's equation the outer radius (r_{out}) of the circle is

expressed by:

$$r_{out} = \sqrt{2R_0\Delta R_{out} + \Delta R_{out}^2} \tag{A.1}$$

using $R_{out}=R_0+\Delta R_{out}$, where R_0 is the height of the altimeter above the surface at nadir. For a satellite borne altimeter $\Delta R_{out} \ll R_0$ and approximation for near-nadir incidence angles result in:

$$r_{out} \approx \sqrt{2R_0\Delta R_{out}} \tag{A.2}$$

Taking into consideration the sphericity of the earth, which is the flat earth approximation for $R_e=\infty$:

$$r_{out} = \sqrt{\frac{2R_0\Delta R_{out}}{1 + R_0/R_e}} \tag{A.3}$$

The time passed after the point of 'first return' (Δt) is given by:

$$\Delta t = t - t_0 = \frac{2\Delta R_{out}}{c} \tag{A.4}$$

resulting in a radius of the footprint

$$r_{out} = \sqrt{\frac{c\Delta t R_0}{1 + R_0/R_e}} \tag{A.5}$$

and corresponding footprint area

$$A_{out} = \pi r_{out}^2 = \frac{\pi c\Delta t R_0}{1 + R_0/R_e} \tag{A.6}$$

At the time the trailing edge of the pulse reaches the surface at nadir, the area of the footprint reaches its maximum value called the pulse limited footprint (PLF), see figure A.1 (c). At this point Δt equals the compressed pulselength ($\Delta t = \tau$) and thus the outer radius and footprint area are given by:

$$r_{PLF} = \sqrt{\frac{c\tau R_0}{1 + R_0/R_e}} \tag{A.7}$$

$$A_{PLF} = \pi r_{PLF}^2 = \frac{\pi c \tau R_0}{1 + R_0/R_e} \tag{A.8}$$

For $\Delta t > \tau$ an annulus expands at the surface, see figure A.1 (d). The inner radius of the annulus (r_{in}) and corresponding area (A_{in}) is given by:

$$r_{in} = \sqrt{\frac{c(\Delta t - \tau)R_0}{1 + R_0/R_e}} \tag{A.9}$$

$$A_{in} = \pi r_{out}^2 = \frac{\pi c(\Delta t - \tau)}{1 + R_0/R_e} \tag{A.10}$$

Finally, it is shown that the area of the annulus is constant in time and given by the area of the pulse limited footprint:

$$A_{annulus} = A_{out} - A_{in} = \frac{\pi c \tau R_0}{1 + R_0/R_e} = A_{PLF} \tag{A.11}$$

Using equation A.7 the diameter of the pulse limited footprint area for ENVISAT becomes 1.6 km, using τ=3.125 ns, H=800 km and R_e = 6,371 km.

Antenna Gain Pattern

The following equations have been adapted from Ulaby et al. (1981), chapter 3.

The gain pattern of an antenna is best described by taking starting point in an isotropic antenna. An isotropic antenna is a hypothetical antenna, radiating equally in all directions. Real antennas are different and do not have an ideal radiation distribution. On the contrary, energy varies with angular displacement and losses occur due to side and back lobes. The angular radiation pattern is known as the antenna gain pattern. The most efficient antennas are characterized by a wide main lobe, small side and back lobes.

The antenna of the RA-2 altimeter is a dual-frequency parabolic antenna, see figure A.2 (a). To a first approximation the antenna can be modelled as a circular aperture in the far-field approximation, known as Fraunhofer diffraction. In the far-field approximation the wavefront may be considered plane without appreciable error. By solving the problem for a circular aperture, the antenna gain pattern is

given by:

$$G(x) = G_0 \left(\frac{2J_1(x)}{x} \right)^2 \tag{A.12}$$

here J_1 is the first order Bessel function of first kind, G_0 the maximum antenna gain and the variable x is given by:

$$x = \frac{\pi D}{\lambda} sin\theta \tag{A.13}$$

where D is the diameter of the antenna, λ the transmitted wavelength and ϕ the angle of boresight.

The RA-2 altimeter antenna has an antenna diameter spanning 1.2 m, a maximum gain $G_0 = 41.6$ dBi, where dBi is taken relative to a hypothetical isotropic antenna, and the wavelength 2.21 cm (ENVISAT RA2/MWR Product Handbook, 2002).

Figure A.2: The ENVISAT radar altimeter is a parabolic antenna (Source: See chapter 8).

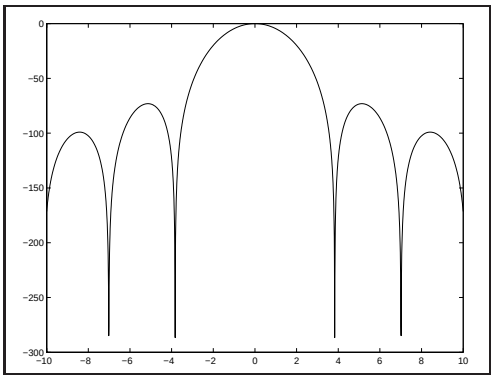

Figure A.3: Antenna gain pattern of a circular aperture as a function of x, see equation A.12.

Mission	Operation	Organization	Altitude [km]	Footprint [m]	Compr. pulse length [ns]	PRF [Hz]	Frequency [GHz]	Coverage N/S	Cycle (days)
SKYLAB	1973	NASA	435	8000	100	100			
GEOS-3	1974	NASA	840	3600	12.5	100	13.9	72	
SeaSat	1978	NASA	800	1700	3	1020	13.5	72	17
GEOSAT	1985-1989	US Navy	800	1700	3	1020	13.5	72	17
ERS-1	1991-1996	ESA	800	1700	3	1020	13.5	81.5	35 (C+G)
Topex/Poseidon	1992-2002	CNES/NASA	1300	2200	3	4000/1700	13.6/5.3	66	10
ERS-2	1995-2003	ESA	800	1700	3	1020	13.5	81.5	35
GFO	1998-	US Navy	800	1700	3		13.5	72	17
JASON-1	2001-	CNES/NASA	1300	2200	3		13.5/5.3	66	10
ENVISAT	2002-	ESA	800	1600	3	1800	13.6/3.2	81.5	35
ICESat	2003-	NASA	600	60	4	40	1064ns/532ns		183
CryoSat	2004	ESA	720					86	369(30)
JASON-2	2005	CNES/NASA	1300	2200			13.6/5.3	66	

Appendix B

ENVISAT Data

- **Data Products**
- **Orbits - Cycle 10 and Cycle 15**

level 0	raw	Unprocessed data as it comes from the satellite
level 1b	engineering	Data converted to engineering units (no re-tracking)
level 2b	geophysical	Data converted to geophysical units with re-tracking

RA-2 Level 2 Product			
< 3 hours	FGDR	Fast Delivery Data Record	Products for weather forecasting Sea-state and ocean-circulation applications
< 3 days	IGDR	Interim Geophysical Data Record	FGDR-data with more precise analysis, and the preliminary orbit with an improved orbit solution
30-50 days	GDR	Geophysical Data Record	The most precise low-rate (1.11 sec) product including Geophysical corrections Instrument corrections Precise Orbit Determinations
30-50 days	SGDR	Sensor Geophysical Data Record	GDR data including Averaged waveforms (high-rate 18 Hz) Individual waveforms (1800 Hz) for selected orbits

Cycle10 October 2002		
Date	Orbit	Time [UTC]
6	84	19.02
7	97	16.56
	98	17.53
	99	19.33
8	112	18.03
	113	19.02
10	139	13.47
	141	18.39
	142	19.39
11	154	14.56
	155	17.27
	156	19.07
12	168	15.15
	169	16.05
13	184	18.10

Cycle15 April 2003		
Date	Orbit	Time [UTC]
9	226	17.12
	227	18.10
	228	19.50
10	239	13.27
	240	15.07
	240	15.58
	241	17.38
	242	19.19
11	253	12.55
	254	14.36
	254	15.26
	255	16.16
	255	17.07
	256	18.47
12	268	14.04
	268	14.54
	269	15.45
	269	16.35
	270	18.16
	271	19.56
13	283	15.13
14	296	13.01
	297	14.41
	297	15.32
	298	16.22
	298	17.12
	299	18.53
15	312	17.29
	313	18.21
	314	20.02

Appendix C

Review of Sea Ice Parameters

- **Chronological Review of Sea Ice Parameters**

Author	Altimeter	Parameters
Dwyer and Godin (1980)	GEOS-3/Seasat	Index=((100+AGC)/100xAASG)-10 AGC=Antenna Gain Control AASG=average attitude/specular gate signal
Ulander (1987)	Seasat	peak backscatter extrapolating the plateau intensities to the position of the peak intensity
Hawkins and Lybanon (1989)	Geosat	Index=((100+AGC)/100xVATT)-10 AGC=Antenna Gain Control VATT=(ATTG-ATTGE)/(AGCG-ATTGE) ATTG=mean of least eight bin gates ATTGE=mean of first eight bin gates AGCG=mean of center 48 samples (not incl. the track point gate) Index=0.6-0.7 open ocean, Index >1 Sea Ice
Laxon (1990)	Geosat	Standard Deviation of Surface Height Antenna Gain Control (AGC) Sea Wave Heights (SWH)
Drinkwater (1991)	RAL (airborne)	pulsewidth peak backscatter waveform integral
Laxon (1994b)	ERS-1	Pulse Peakiness Standard Deviation of Surface Height (SDALT)
Laxon (1994a)	ERS-1	peak backscatter 3 gates defining the shape of the trailing edge 2 gates defining the shape of the leading edge
Peacock and Laxon (2001)	ERS-1/2	Pulse Peakiness

Appendix D

Tables of Characteristic Sea Ice Parameters

6-7 October 2002 and 15 April 2003

- **Backscatter**
- **Peak Power**
- **Pulse Peakiness**

Backscatter [dB]	**6-7 October 2002**			
Parameter	orbit	average	maximum	minimum
Open Ocean	84	8.0	9.0	7.3
	97	8.8	9.9	7.9
	98	9.3	12.4	7.7
Marginal Ice Zone	84	32.4	50.4	8.8
	97	28.0	32.6	22.1
	98	35.9	44.9	24.4
Consolidated Ice	84	-	-	-
	97	34.1	52.2	16.9
	98	37.0	48.9	25.4

Backscatter [dB]	**15 April 2003**			
Parameter	orbit	average	maximum	minimum
Open Ocean	312	8.8	10.1	7.7
	313	13.3	21.9	10.3
	314	11.0	19.8	9.1
Marginal Ice Zone	312	27.5	37.3	16.1
	313	23.1	45.7	10.1
The Odden Area	314	31.3	38.3	18.2
Consolidated Ice	312	23.6	48.5	8.0
	313	25.2	53.9	5.4
	314	28.3	45.0	4.1
Fast Ice	312	-	-	-
	313	7.7	11.2	5.3
	314	3.0	5.4	1.1

Peak Power [dB]	**6-7 October 2002**			
Parameter	orbit	average	maximum	minimum
Open Ocean	84	26.4	27.3	25.8
	97	26.4	27.5	25.7
	98	26.4	27.5	25.7
Marginal Ice Zone	84	28.3	43.6	9.0
	97	27.7	47.9	7.0
	98	27.7	40.3	16.5
Consolidated Ice	84	-	-	-
	97	28.3	48.0	7.0
	98	27.7	41.0	15.4

Peak Power [dB]	**15 April 2003**			
Parameter	orbit	average	maximum	minimum
Open Ocean	312	26.4	27.3	25.8
	313	26.5	28.3	25.6
	314	26.4	27.7	25.7
Marginal Ice Zone	312	28.6	35.0	21.0
	313	28.6	38.1	14.6
The Odden Area	314	27.8	31.4	22.4
Consolidated Ice	312	28.1	47.3	16.5
	313	28.3	48.0	7.0
	314	27.7	48.0	4.8
Fast Ice	312	-	-	-
	313	27.2	30.3	25.9
	314	26.6	27.3	25.6

Pulse Peakiness	**6-7 October 2002**			
Parameter	orbit	average	maximum	minimum
Open Ocean	84	0.89	1.08	0.78
	97	0.89	1.11	0.75
	98	0.89	1.17	0.77
Marginal Ice Zone	84	0.90	30.53	0.74
	97	4.53	7.67	1.88
	98	12.85	29.84	1.77
Consolidated Ice	84	-	-	-
	97	17.43	31.44	2.26
	98	16.43	30.55	2.87

Pulse Peakiness	**15 April 2003**			
Parameter	orbit	average	maximum	minimum
Open Ocean	312	0.90	1.10	0.74
	313	0.91	1.38	0.75
	314	0.90	1.20	0.68
Marginal Ice Zone	312	7.53	20.50	1.10
	313	5.62	28.12	0.81
The Odden Area	314	2.03	7.08	0.86
Consolidated Ice	312	9.41	31.27	0.76
	313	10.22	37.46	0.99
	314	13.90	30.50	0.74
Fast Ice	312	-	-	-
	313	1.18	2.65	0.80
	314	0.93	1.13	0.72

Pulse Peakiness	**6-7 October 2002**		
Parameter	orbit	diffuse (PP≤1.8)	specular (PP>1.8)
Open Ocean	84	100.0	0.0
	97	100.0	0.0
	98	100.0	0.0
Marginal Ice Zone	84	11.4	88.6
	97	28.3	71.7
	98	0.4	99.6
Consolidated Ice	84	-	-
	97	0.0	100.0
	98	0.0	100.0

Pulse Peakiness	**15 April 2003**		
Parameter	orbit	diffuse (PP≤1.8)	specular (PP>1.8)
Open Ocean	312	100.0	0.0
	313	100.0	0.0
	314	100.0	0.0
Marginal Ice Zone	312	6.9	93.1
	313	20.8	79.2
The Odden Area	314	55.7	44.3
Consolidated Ice	312	11.8	88.2
	313	12.2	87.8
	314	7.9	92.1
Fast Ice	312	-	-
	313	94.4	5.6
	314	96.9	3.1

Appendix E

Maps of Sea Ice Parameters

8-13 October 2002 and 9-14 April 2003

- **Backscatter**
- **Peak Power**
- **Pulse Peakiness**

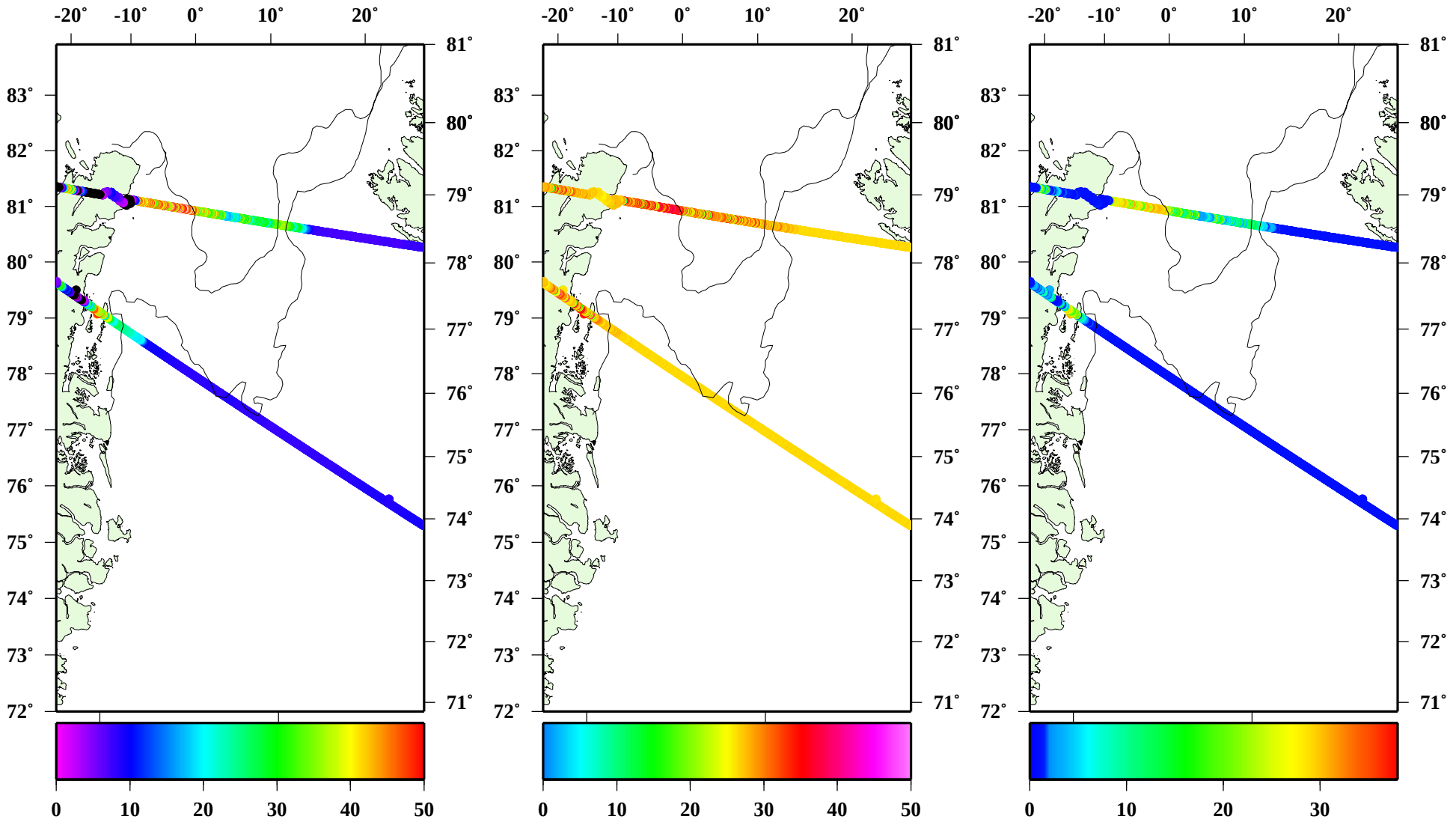

(a) Backscatter (b) Peak Power (c) Pulse Peakiness

Figure E.1: Groundtracks the 8th of October 2002. Ice analysis based on data from the 5th of October 2002

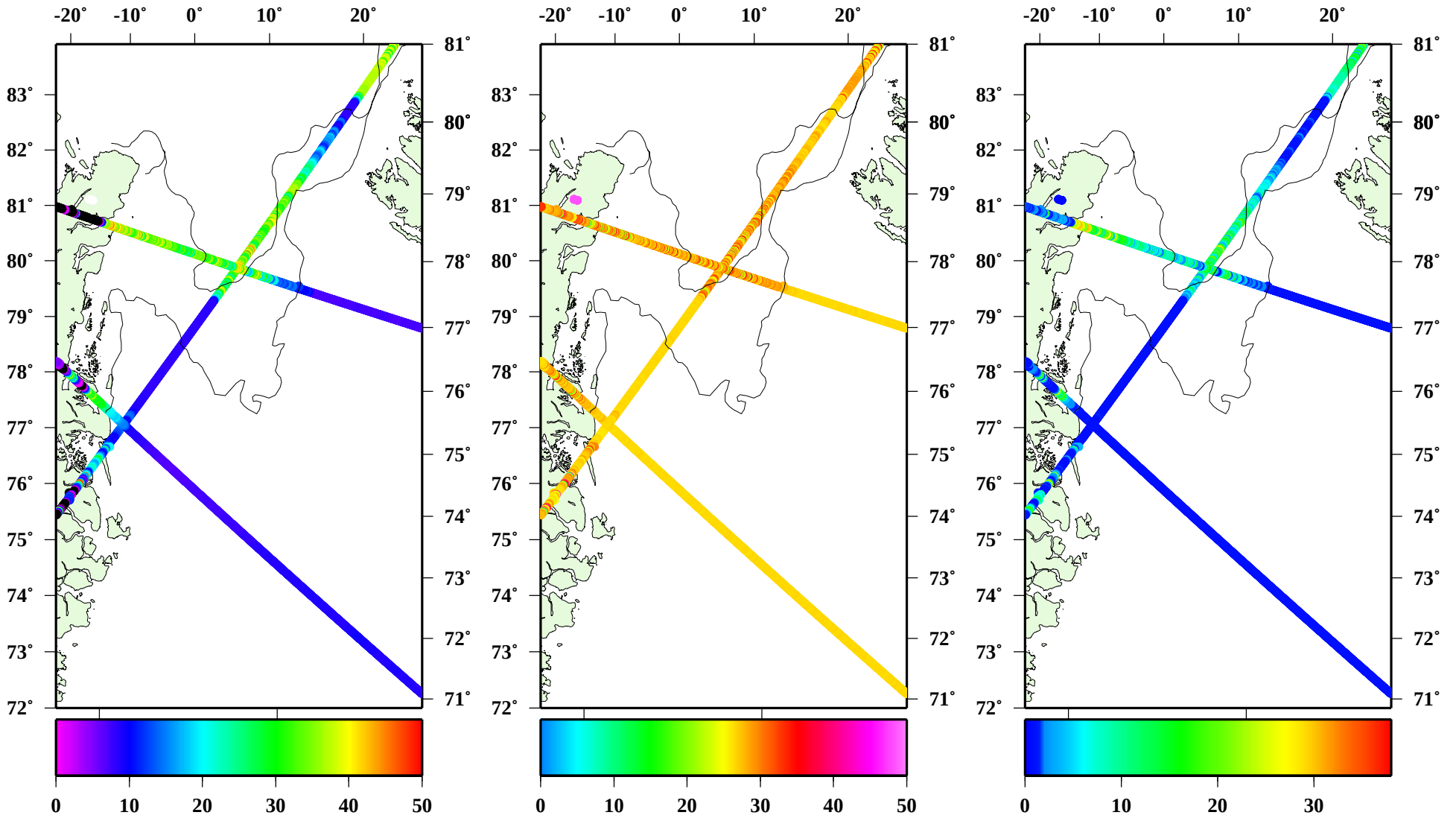

(a) Backscatter

(b) Peak Power

(c) Pulse Peakiness

Figure E.2: Groundtracks the 10th of October 2002. Ice analysis based on data from the 5th of October 2002

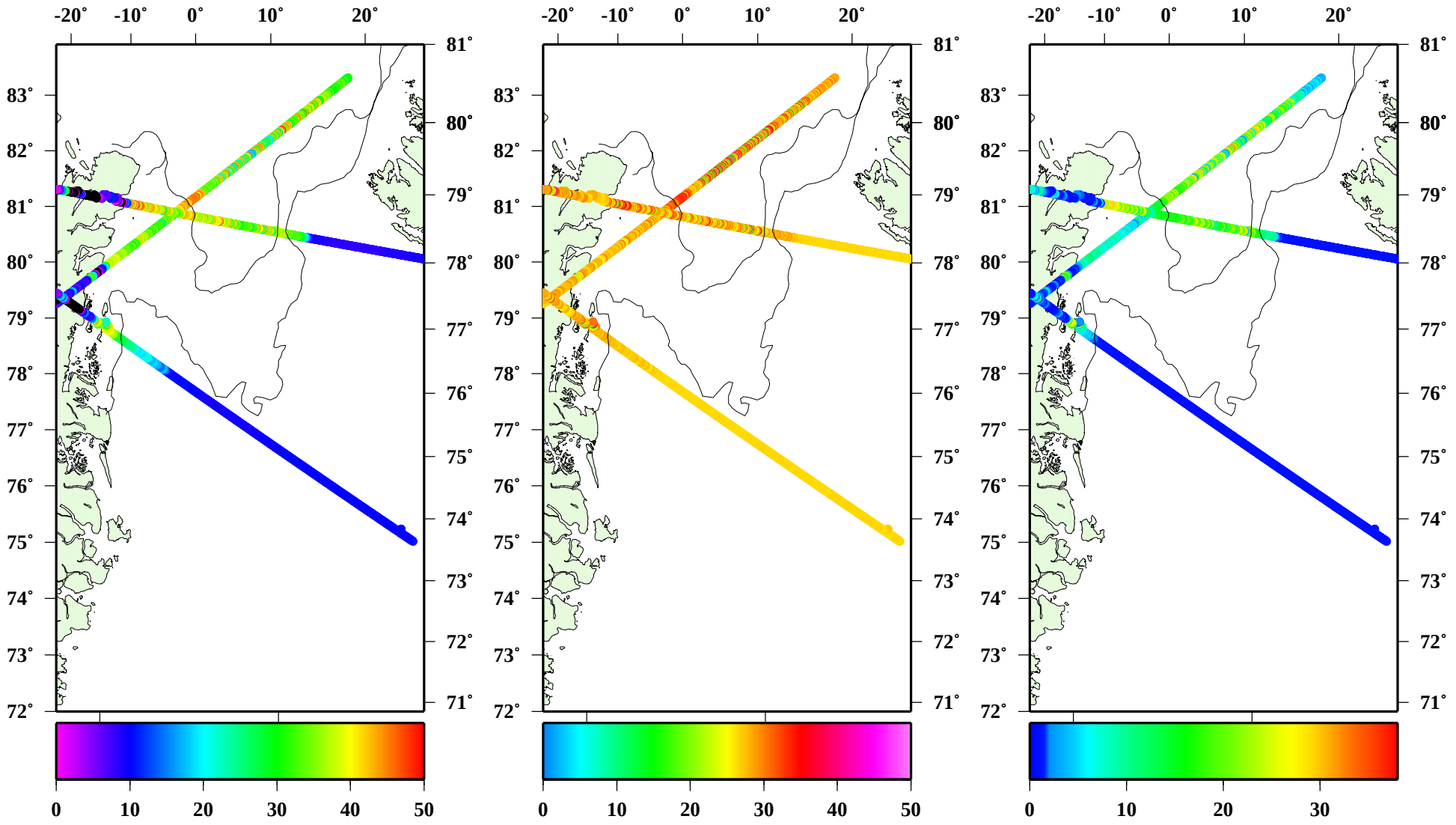

(a) Backscatter

(b) Peak Power

(c) Pulse Peakiness

Figure E.3: Groundtracks the 11th of October 2002. Ice analysis based on data from the 5th of October 2002

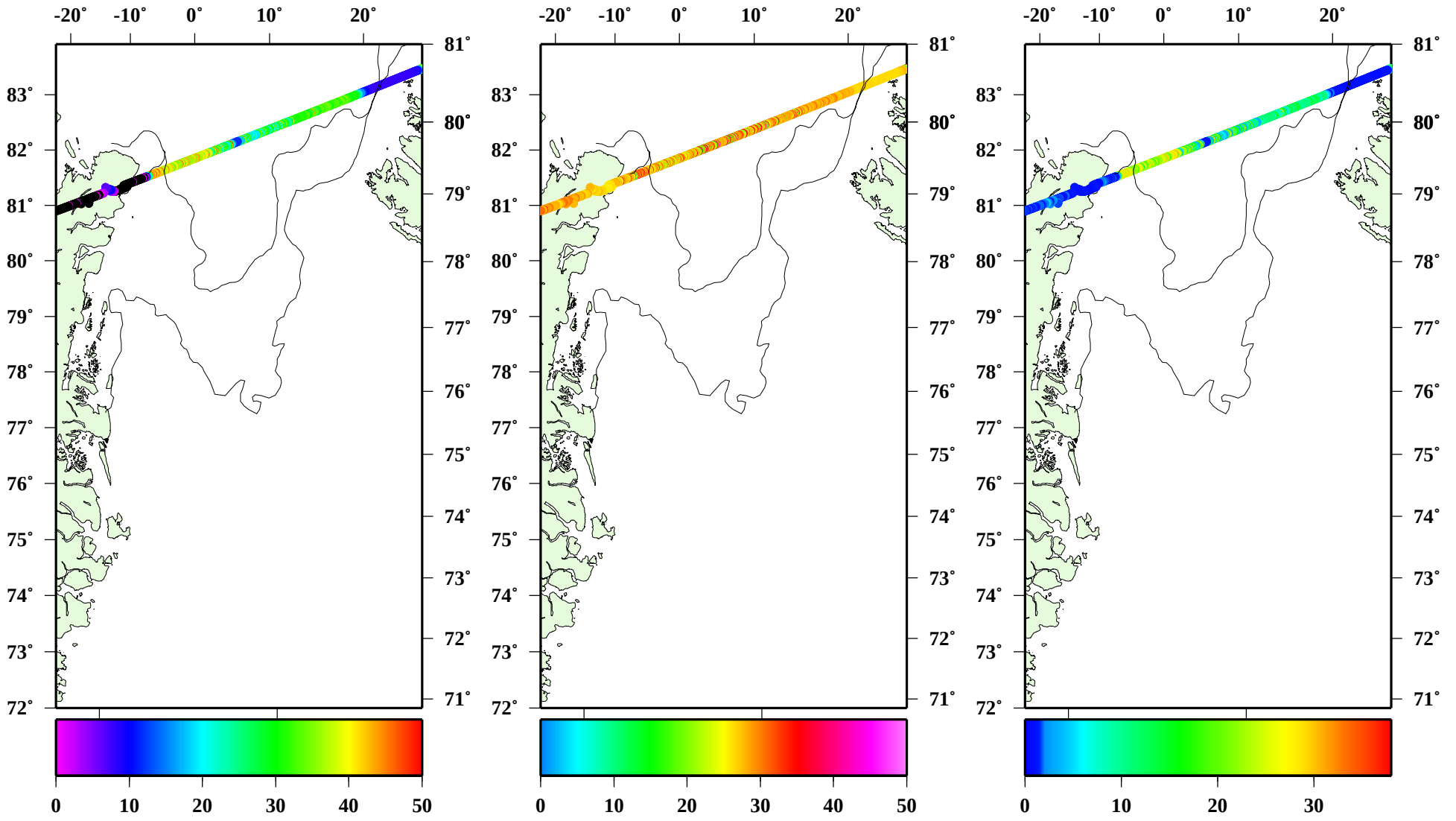

(a) Backscatter (b) Peak Power (c) Pulse Peakiness

Figure E.4: Groundtrack the 12th of October 2002. Ice analysis based on data from the 5th of October 2002

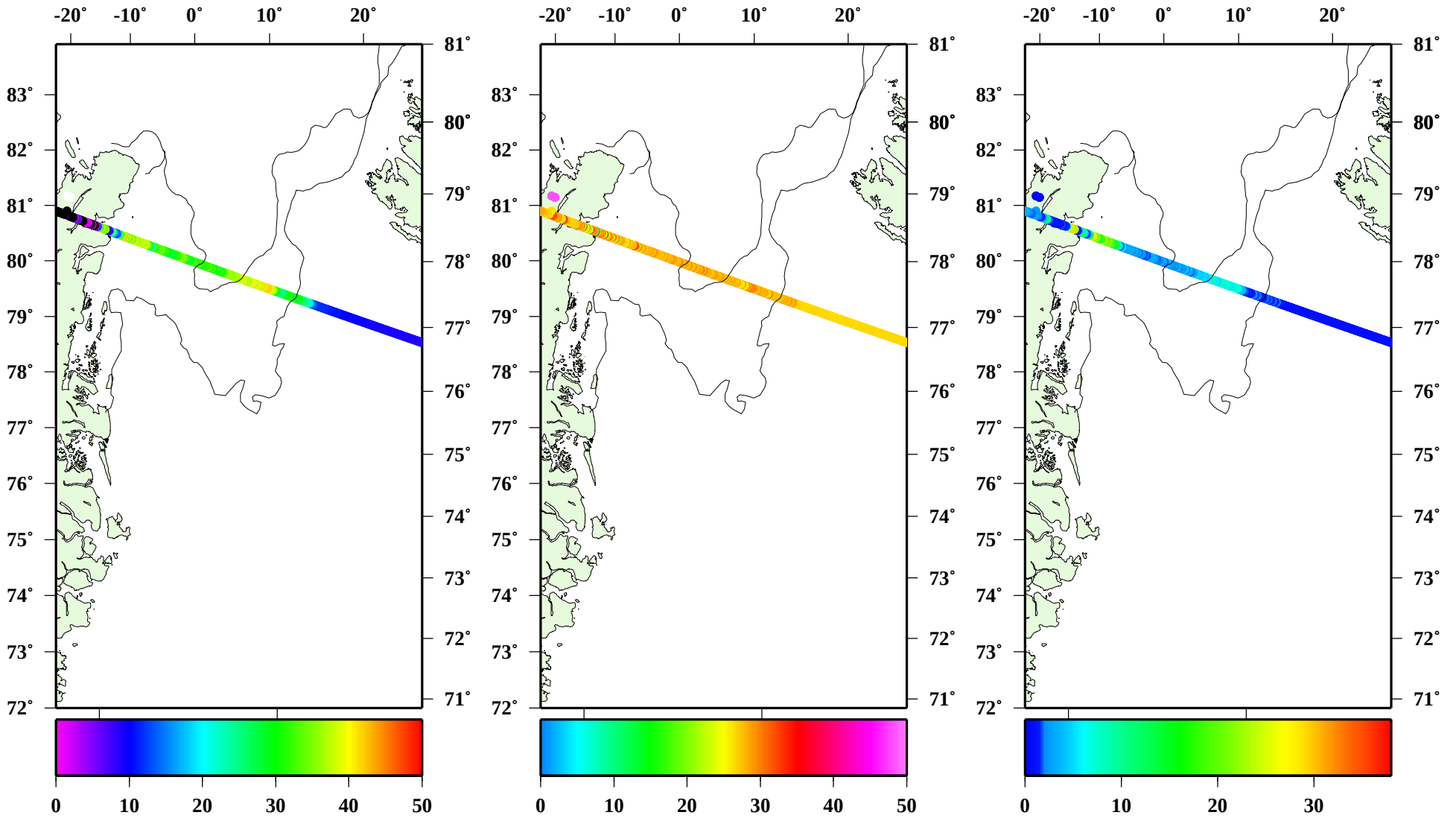

(a) Backscatter (b) Peak Power (c) Pulse Peakiness

Figure E.5: Groundtrack the 13th of October 2002. Ice analysis based on data from the 5th of October 2002

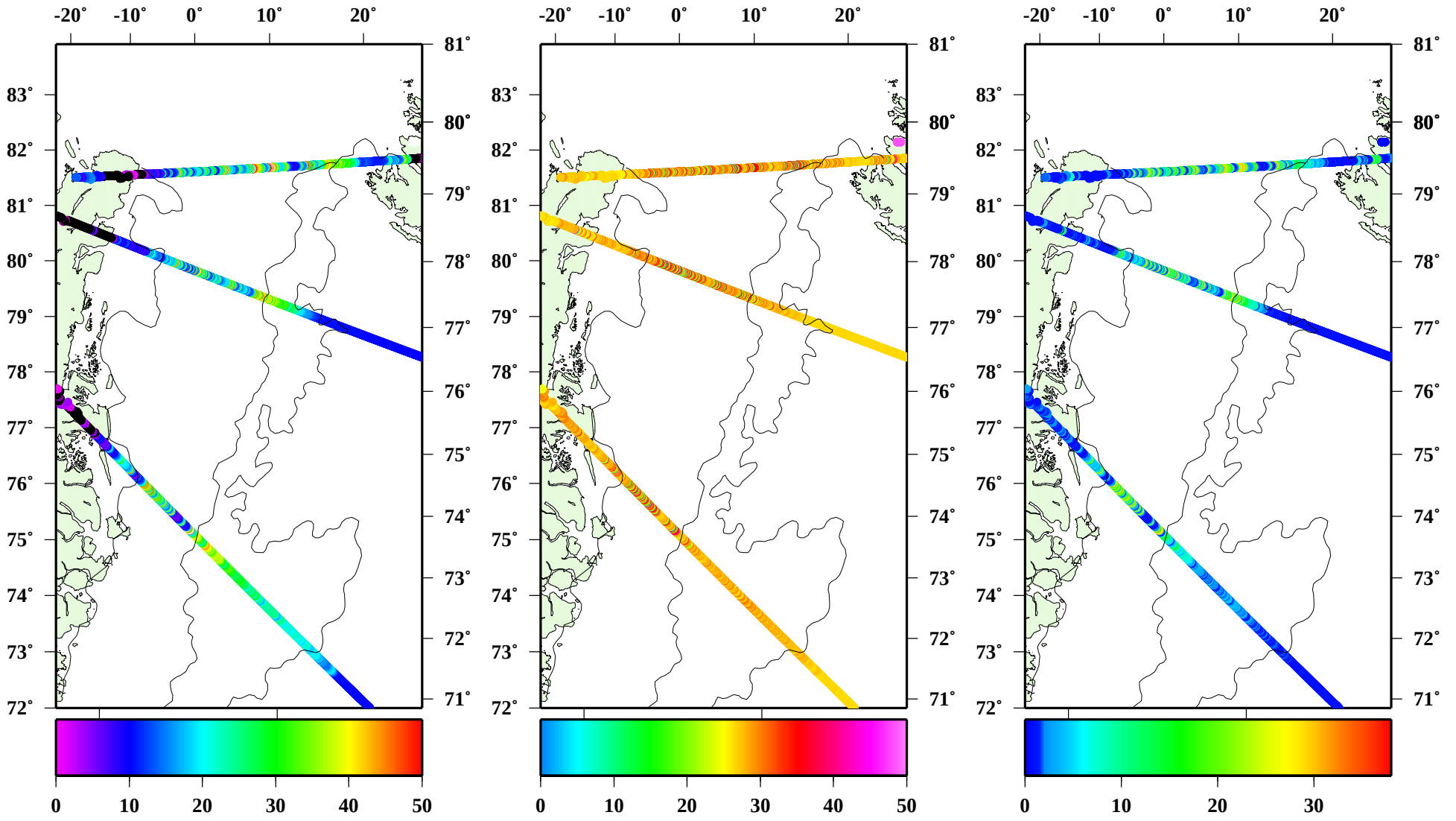

(a) Backscatter

(b) Peak Power

(c) Pulse Peakiness

Figure E.6: Groundtracks the 9th of April 2003. Ice analysis based on data from the 15th of April 2003

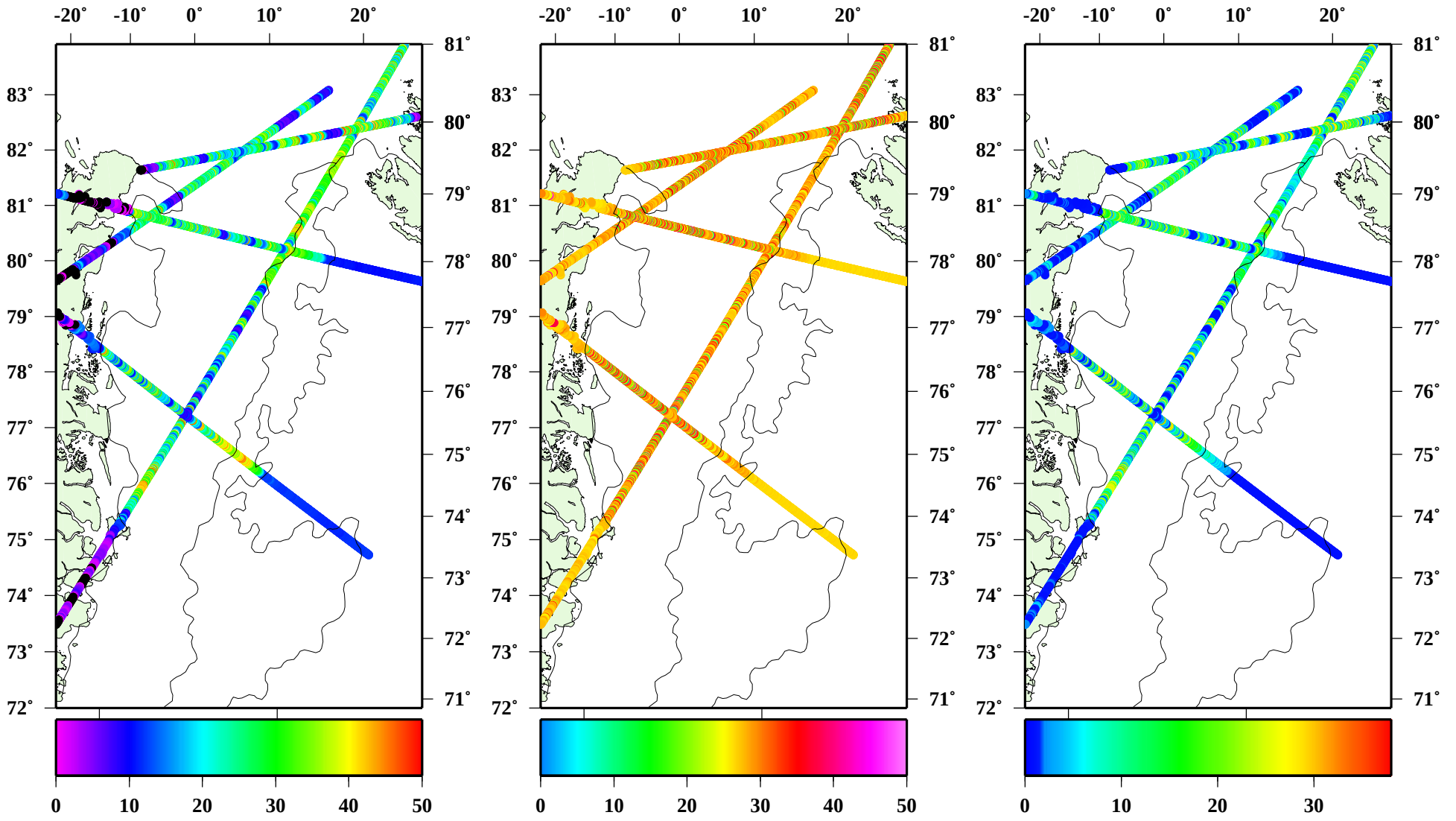

(a) Backscatter (b) Peak Power (c) Pulse Peakiness

Figure E.7: Groundtracks the 10th of April 2003. Ice analysis based on data from the 15th of April 2003

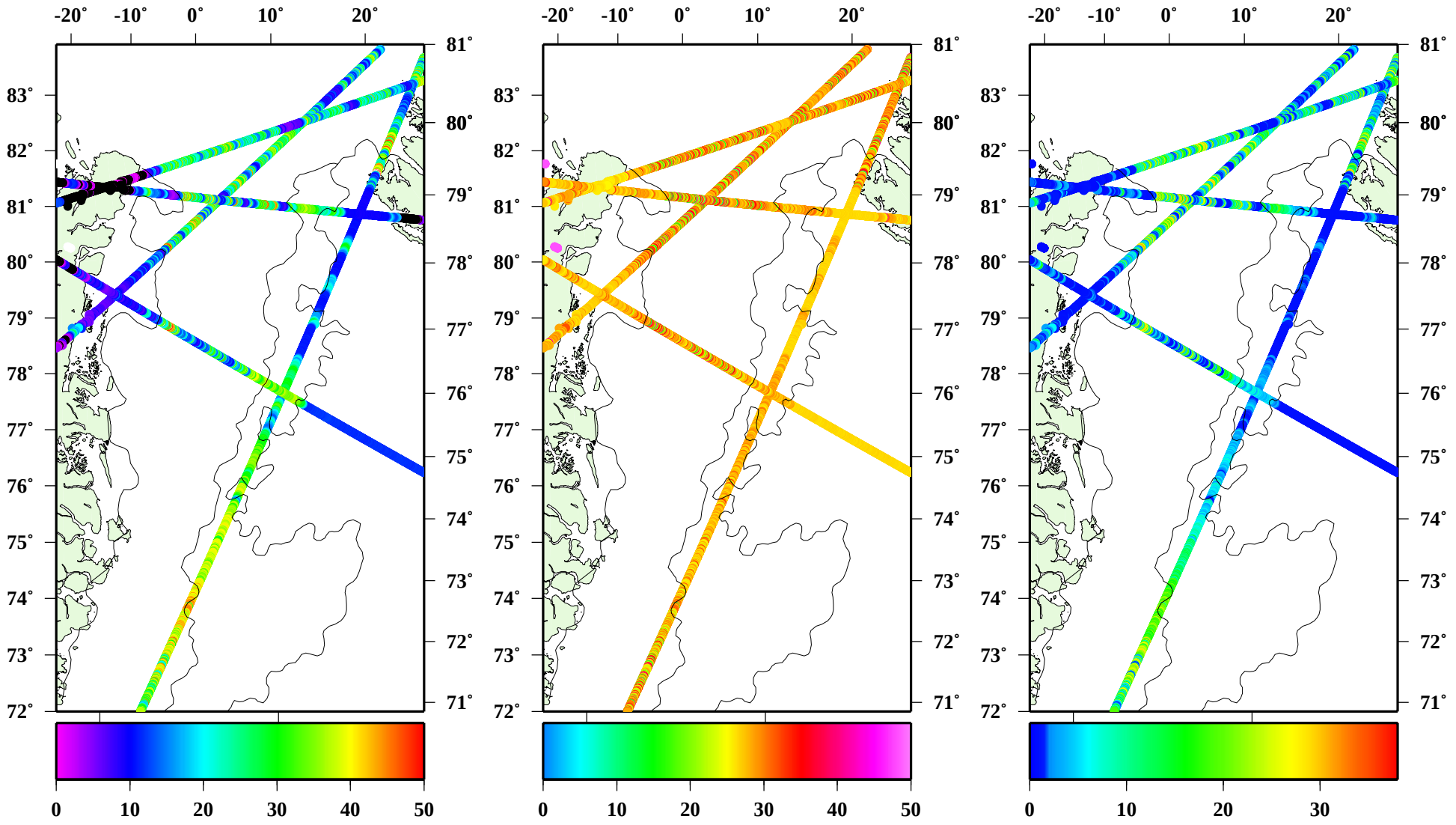

(a) Backscatter

(b) Peak Power

(c) Pulse Peakiness

Figure E.8: Groundtracks the 11th of April 2003. Ice analysis based on data from the 15th of April 2003

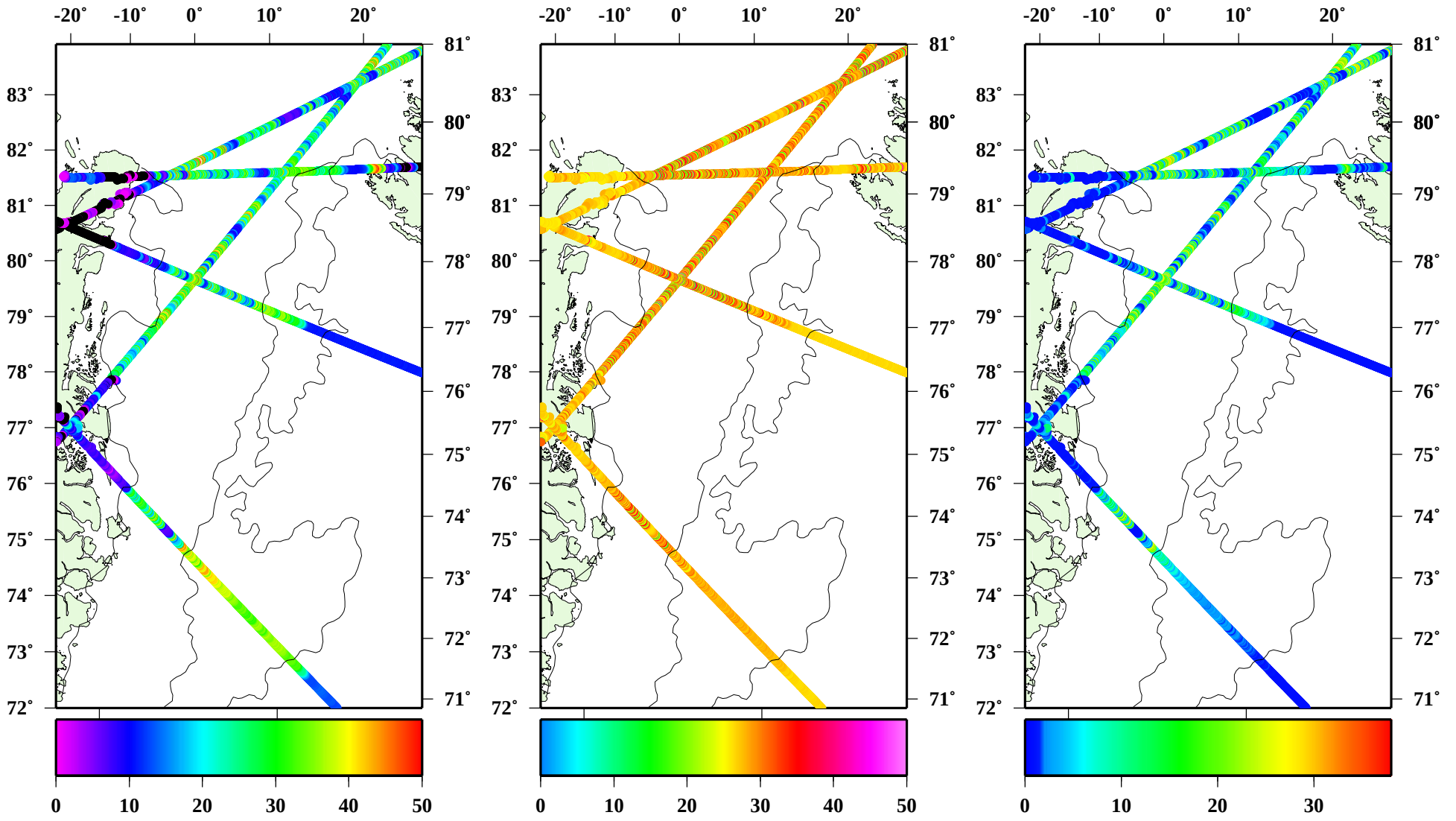

(a) Backscatter

(b) Peak Power

(c) Pulse Peakiness

Figure E.9: Groundtracks the 12th of April 2003. Ice analysis based on data from the 15th of April 2003

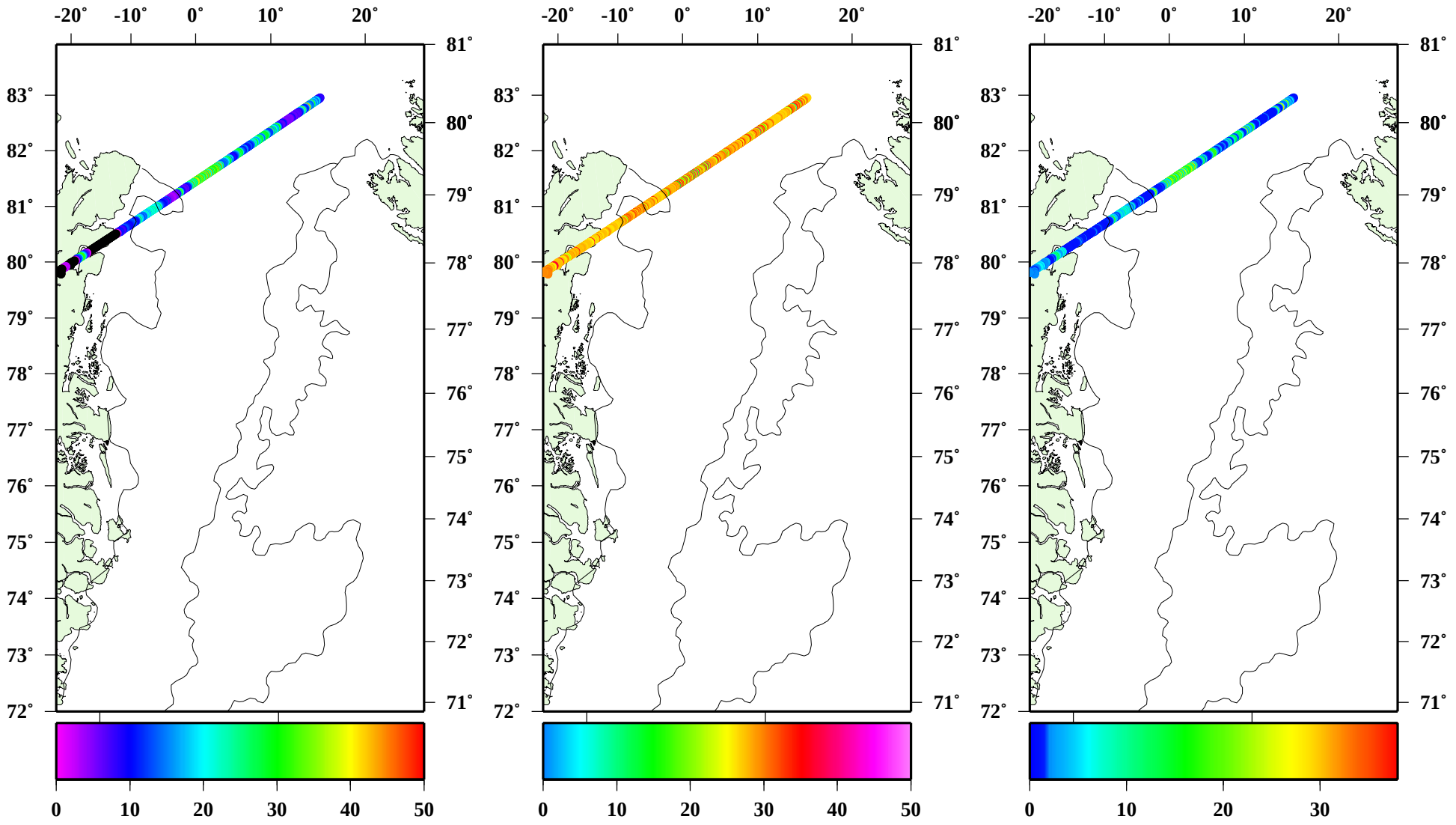

(a) Backscatter (b) Peak Power (c) Pulse Peakiness

Figure E.10: Groundtrack the 13th of April 2003. Ice analysis based on data from the 15th of April 2003

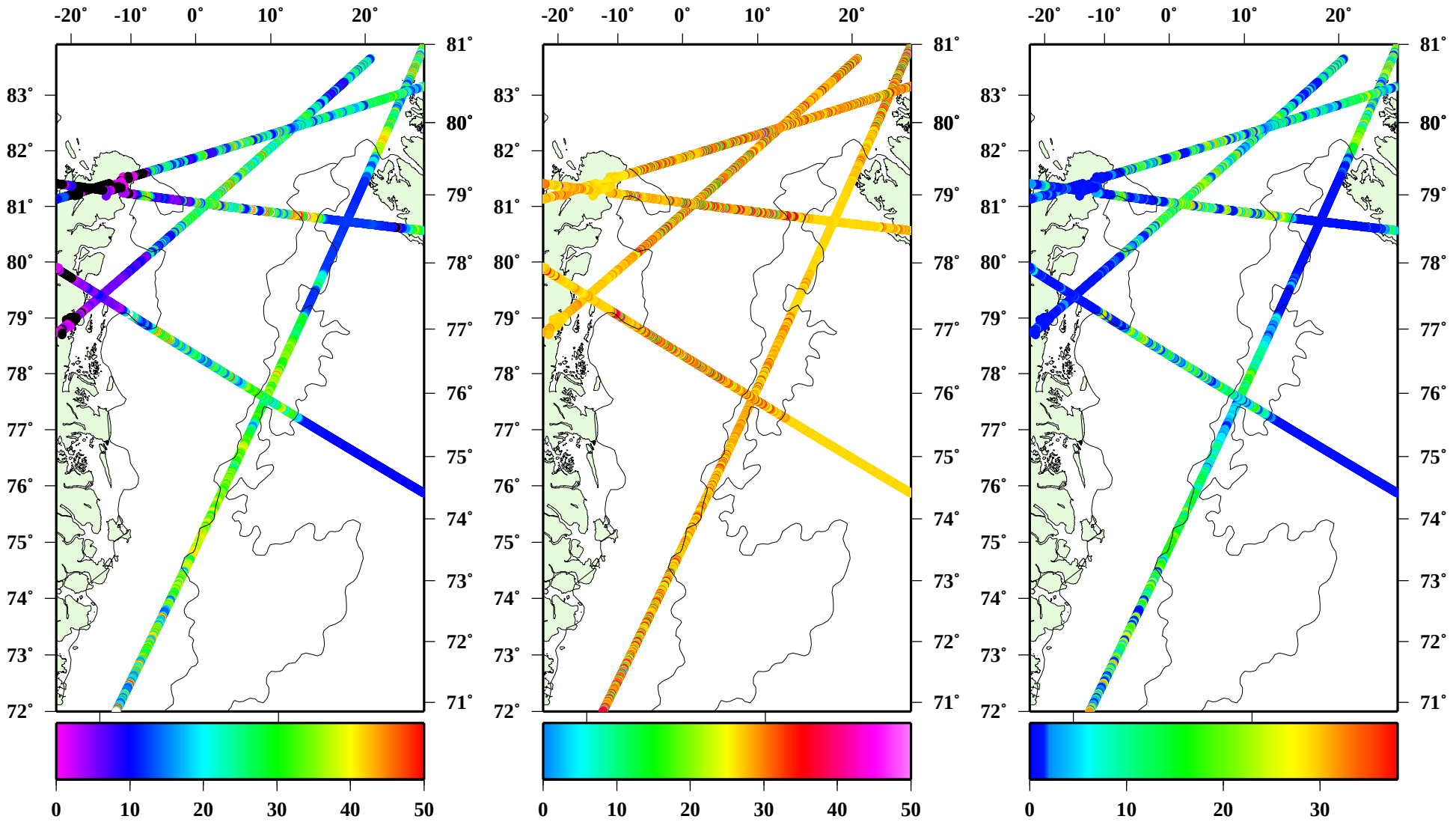

(a) Backscatter

(b) Peak Power

(c) Pulse Peakiness

Figure E.11: Groundtracks the 14th of April 2003. Ice analysis based on data from the 15th of April 2003

Appendix F

Test of Transponder

- **Description of Transponder**
- **Location - Rungsted, Denmark**
- **Interpretation**
- **Preparation For Future Operations**

Description of Transponder

A transponder receives, amplifies and retransmits the radar pulses emitted from the satellite borne altimeter and acts as a point reflector with amplification. Knowing the exact position of the transponder it can be used as a calibration "tool", either to find an exact height of the satellite or to define a reference surface, e.g. surfaces of ice sheets. The problems concerning ice sheets are that the upper layers is composed of uncompressed snow (firn). The radar signal will penetrate the surface and become dominated by volume scattering, which complicates the procedure to define the exact position of the surface. For further information see Haardeng-Pedersen et al. (1998).

The signal of the transponder is first observed in the waveform data after being received by a ground station and processed. The peak of the signal of the transponder will achieve a parabolic form, see figure F.1. The altimeter pulses transmitted have a pulse repetition frequency of 1800 Hz (ENVISAT). This frequency is amplified to provide an audible whistle during overflight. Due to the fact that the orbit velocity of the satellite is in the order of 7.5 km/s the whistle is of very short duration, about 3-4 seconds. During the time of overflight the satellite altimeter radiates approximately 7000 individual waveforms in the direction of the transponder, corresponding to 70 averaged waveforms.

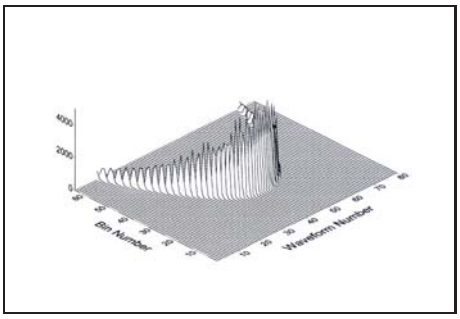

Figure F.1: The theoretical altimeter signature of the transponder has a characteristic parabolic form. (Haardeng-Pedersen et al., 1998)

Figure F.2: Transponder ready for operation. The sides can be upfolded to ease transportation. The weight is about 85 kg.

Location - Rungsted, Denmark

Orbit 380 was selected for the purpose to test the transponder belonging to the Department of Geophysics, University of Copenhagen. The orbit passes Rungsted Harbour, Denmark, in a descending mode resulting in the most steady return signal approaching the transponder from open water. The return signal above water is homogeneous, as it comprises a relatively plane surface compared to e.g. land surfaces.

Being in a sun synchronous orbit ENVISAT covers the same ground track every 35th day within 1 km of accuracy, see chapter 3.5. The return signal of three passes (April 20th, May 25th and June 29th 2003) from three successive cycles (15, 16 and 17) have been analyzed. Figure F.3 shows the ground tracks of the three passes used, in the region of Rungsted Harbour where the lower 'eye' represents the location of the transponder. The transponder was only operational on the 25th of May and on the 29th of June, and the altimeter onboard ENVISAT was only switched to the *preset loop output mode* at the time of passage the 29th of June. The *preset loop output mode* is a special mode used for transponders in order to gain maximum information of the transponder signal. In the ordinary mode the position of the range window moves as the surface changes to keep the return pulse within the window. In the *preset loop output mode* the position of the range window is set for each return pulse, such that the instrument does not follow the surface any more (Roca et al., 2002).

The location was inspected beforehand and seemed to be a reasonable choice. The exact position for the location of the transponder was measured by *Global Positioning System* (GPS), see appendix G.

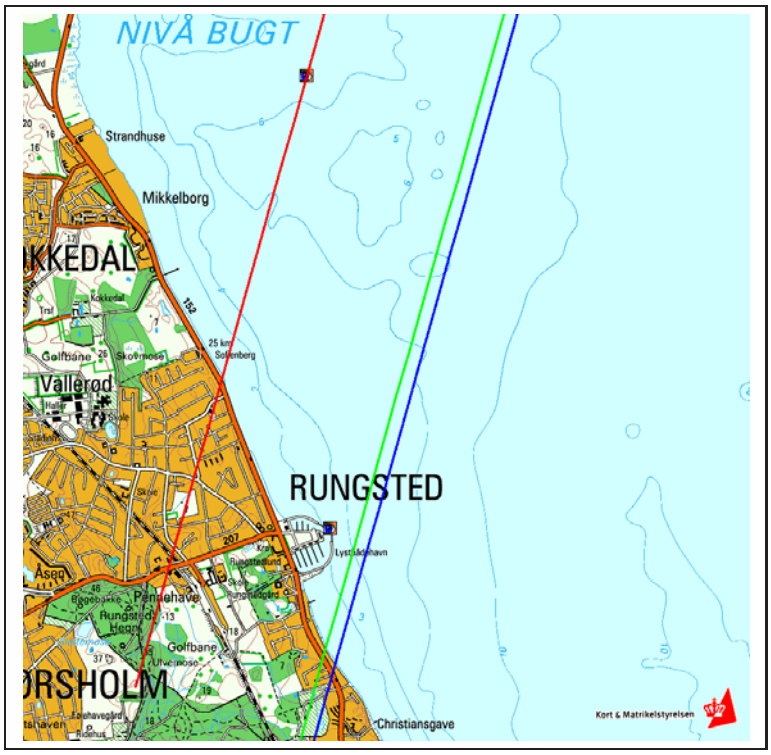

Figure F.3: Groundtrack 380 above Rungsted Harbour 2003. The red track is from the 20th of April, the blue track from the 25th of May and the green track from the 29th of June. The lower 'eye' represents the location of the transponder.

Interpretation

In the passes at the 25th of May and the 29th of June the transponder should be in range of the satellite as the closest distance of the ground track and the transponder is 340 m and 225 m respectively. The 29th of June the transponder whistled at the exact time of the passage of the satellite, at about 10.00 UTC. The whistle was not heard during the operation time of the transponder on the 25th of May. There is however a small possibility that the signal vanished in the background noise.

The return signals from the 25th of May and the 29th of June, see figure F.4 and F.5, take the characteristic parabolic form as if a point scatterer (such as a transponder) is present.

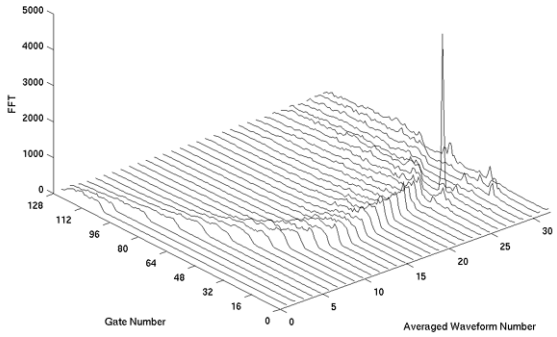

Figure F.4: Altimeter return signal orbit 380 over transponder located at Rungsted, 25th of May 2003.

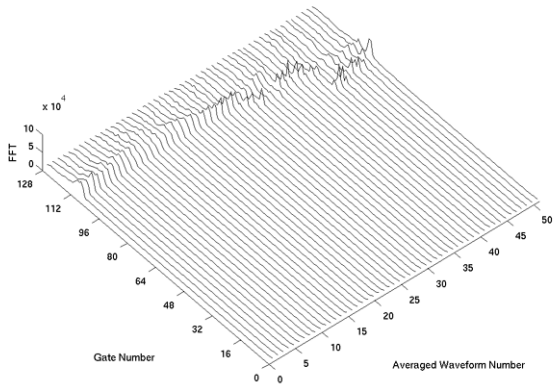

Figure F.5: Altimeter return signal orbit 380 over transponder located at Rungsted, 29th of June 2003. The transponder is in the *preset loop output mode*.

For comparison the return signal from the 20th of April has been investigated, see figure F.6. This pass follows a more northern track and is at the closest point 1,200 m from the transponder site. At this point the satellite is over land which makes it difficult to interpret the return signal. There is therefore a striking similarity in the return signal further north, at the position of the upper 'eye' in figure F.3, as the satellite approaches the coast and the return signals from the 25th of May and 29th of June. This may rise the question whether the signal in the two successive passes is a true transponder signal or a natural return signal characteristic for this area when the satellite changes from ocean to land signatures.

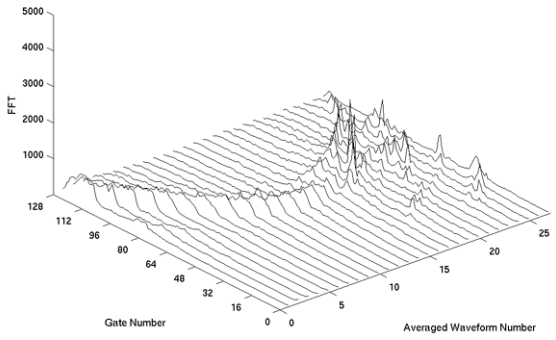

Figure F.6: Altimeter return signal orbit 380 over Rungsted, 20th of April 2003. The transponder is not present at the site.

Another case has been studied. In the Mediterranean Sea, south of Crete at an island called Gavdos, a transponder of a similar type like the transponder tested in this project is located. The waveforms from the descending pass 279 and the ascending pass 285 on June 22nd 2003, over Gavdos is shown in figure F.7. It is seen that the transponder signal is weak and almost vanishes in the waveforms generated by the open ocean.

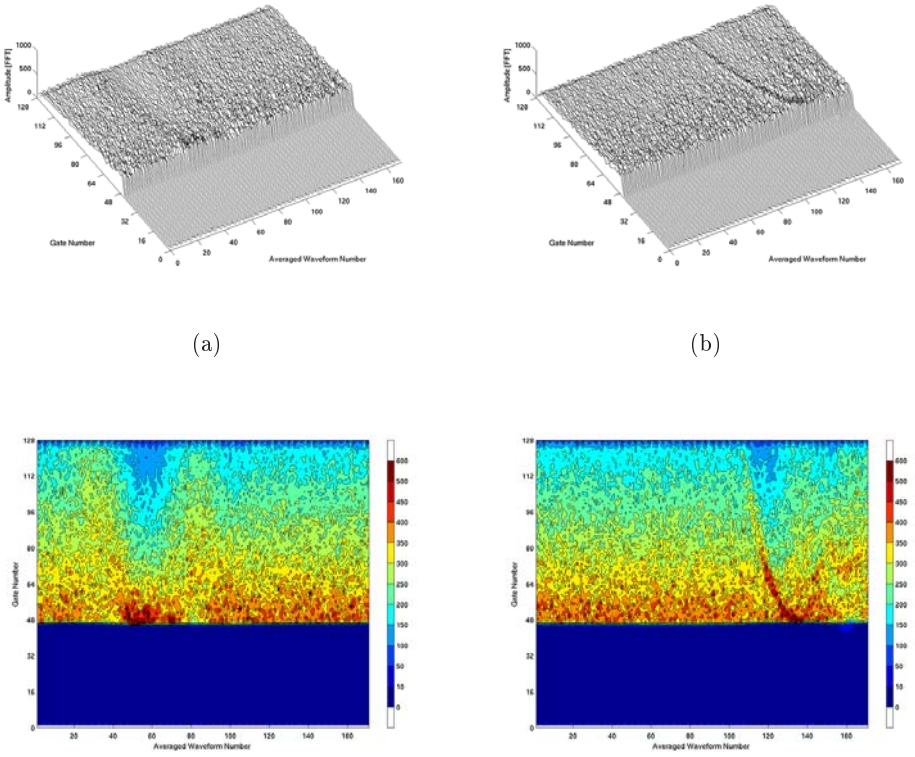

(a) (b)

(c) Orbit 279 (d) Orbit 285

Figure F.7: Altimeter return signals over transponder located at Gavdos, Greece, 22nd of June 2003. (a) and (b) shows the averaged waveforms stacked in the along track time domain. (c) and (d) contour plot of (a) and (b)

The difficulties in the interpretation of the altimeter signals over Rungsted may be due to the fact that Øresund is too narrow to achieve the characteristic open ocean waveforms, see figure F.8.

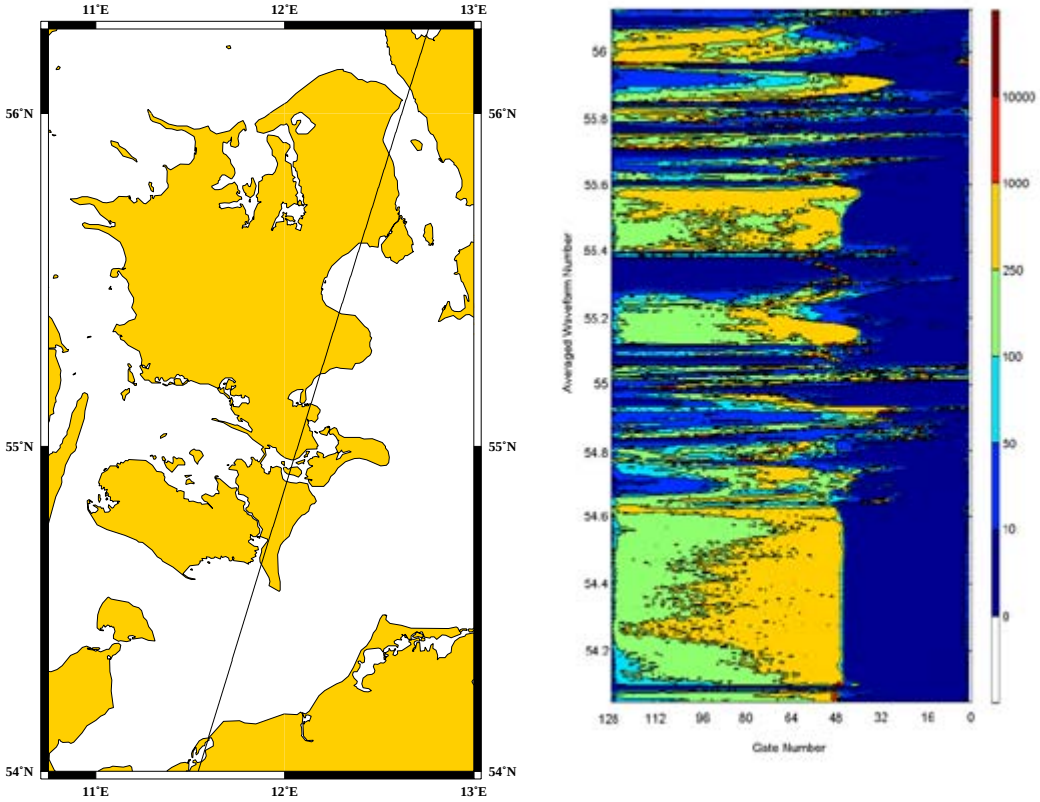

(a) Plot of ground track 380

(b) Contour plot of the averaged waveforms stacked in the along track time domain

Figure F.8: Altimeter return signal orbit 380, 29th of June 2003

Preparation For Future Operations

Before taking the transponder to Greenland it is recommended to make another test in an area of more homogeous surroundings, e.g. the island Anholt in the middle of Kattegat located below ground track 423, see figure F.9. And to compare the return signal to the return signal generated by the transponder located at Gavdos.

Prior to operation of the transponder it is important to inform European Space Agency (ESA) of the exact location of the transponder and the altitude above the reference ellipsoid in order to switch to the *preset loop output mode*.

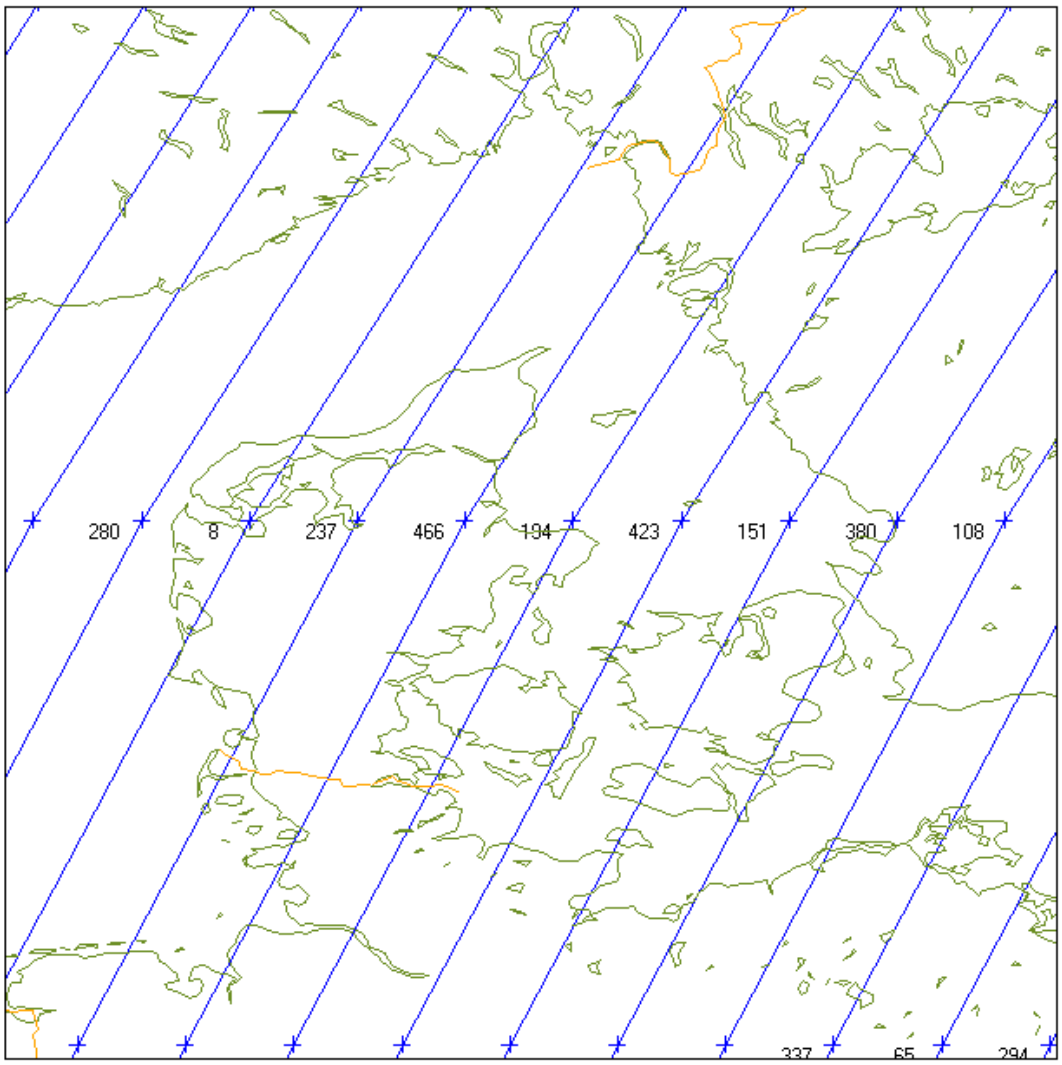

Figure F.9: Descending ground tracks of ENVISAT located above Denmark.

Appendix G

GPS Measurements

- **Position - Rungsted**
- **GPS log sheet**

Position - Rungsted

It is important to know the exact position and height above the reference ellipsoid (WGS84) of the transponder. A two frequency Trimble 5700 GPS receiver was used to find the position in Rungsted, Denmark. The cutoff value for the elevation (the position of the satellite above the horizon) was set to 15°and the limits selected for the DOPS is below 3. DOPS is a measure of the constellation of the satellites above the point of measurement. A large volume expanded by the satellites gives a good DOP and a small volume gives a bad DOP. The values of DOPS in the period of measurement were calculated by the Trimble Total Control software program.

Position of the transponder test area in Rungsted:

55°53' 10.30169" N
12°32' 58.40562" E
Ellipsoidheight: 37.53 m

Position of reference station, Department of Geophysics, Copenhagen:

55°41' 52.45869"N
12°33' 46.91758"E
Ellipsoidheight: 70.813 m

GPS Observation - Log Sheet		
Operator/Agency H. Skourup/gfy	Project Transponder 2003	Station/location name Rungsted
Session #1	Date (DD-MM-YYYY) 25-05-2003	Antenna setup sketch
Session start (UTC) 10:10	Session end (UTC) 10.30	
Final ant. height 87.1 cm	Used antenna height (illustrated in Antenna setup sketch) Zephyr Geodetic	
Receiver serial no. 0220266486	Receiver type/model Trimble 5700	Receiver loc. gfy 231

Appendix H

Software

EnviView EnviView is a free application that allows the user to open any ENVISAT data file and examine its contents. It is used to export the SGDR data to Hieracial Data Format (HDF) for use in MATLAB.

http://www.envisat.esa.int/services/enviview (Vers. 2.0.7)

ESOV The Earth observation Swath and Orbit Visualization tool is a small software program (23 Mb) which provides the user with the means to visualize the instrument swaths and ground tracks of the ERS-1/2, ENVISAT and Cryosat satellites. It is used in the planning phase for the transponder.

http://eop-cfi.esa.int/ESOV/index.html (Vers. 7.8.2)

GMT The Generic Mapping Tool is a collection of about 60 tools for manipulating geographic and cartesian data sets (including filtering, trend fitting, gridding, projecting, etc.) producing PostScript File (PS) illustrations ranging from simple x-y plots through contour maps to artificially illuminated surfaces and 3-D perspective views. GMT supports about 30 map projections and transformations and comes with support data such as coastlines, rivers, and political boundaries. It is used to map the parameters along the respective groundtracks.

http://gmt.soest.hawaii.edu/gmt.html

GEOIP Is used to add the geoid corrections to the height above the reference ellipsoid. The GRAVSOFT package consists of a number of FORTRAN programs and test data sets. GEOIP is a general purpose interpolation program grids -> point values. It may add/subtract values interpolated from grids by linear or spline interpolation. It may also be used to add or subtract two grids of different spacings, e.g. for restoring reference effects after an FFT prediction. The program may interpolate two grids at the same time (e.g. for deflections) or may be used for "sandwich interpolation" between two different levels (3D interpolation). GEOIP produces statistics of data reductions etc., and implements UTM grids fully.

http://manicoral.kms.dk/PK/gravsoft.htm

Appendix I

Source Code

- **Freeboard (calculate the freeboards)**
- **Functions**
  - Waveform (open the waveform)
  - Plotwvf (plot the waveform stacked in time domain)
  - Position (open the groundtrack positions)
  - Pekiness (calculate the pulse peakiness)

```
%*************************************************************************
% This program calculate the freeboard of sea ice:
%
%                       F = Altitude - Range - N
%
%
% F                     Freeboard
% Altitude              Satellites position above reference ellipsoid
% Range                 Altimeter to ground
% N                     Geoid height (ArcGP) above reference ellipsoid WGS 84
%*************************************************************************
file_name='20030411_1526_SGDR.hdf'
fileinfo = hdfinfo(file_name)
format long;

a=1289;                 % Start point of the subtrack
b=1650;                 % End point of the subtrack
i=1;                    % interval by which the waveforms shall be stacked


%*************************************************************************
% Open the HDF-file and reads data
%*************************************************************************
[data]=waveform(file_name);                         % Reads the waveforms
[latitude,longitude,no]=position(file_name);        % Reads the position of the groundtrack
latitude=latitude(a:b,:);
longitude=longitude(a:b,:);
[Z]=plotwvf(data,a,i,b);                            % plot of stacked averaged waveforms


%*************************************************************************
% Read geoid data (height)
%*************************************************************************
load geoide111526.dat
geoide=geoide111526;
 F=geoide(:,5);                                     % Freeboard


 %*************************************************************************
 % Plot the range and pulse peakiness against time
 %*************************************************************************
 F=F(a:b,:);
 [PP,pmax]=peakiness(data);          % Call the function peakiness to calculate the pulse peakiness
 PP=PP(a:b,:);
 pmax=pmax(a:b,:);

 y=repmat(1.8,[1 size(F,1)]);        % limit PP=1.8
 z=repmat(0,[1 size(F,1)]);          % Sea level 0
 x=[1:size(F,1)];

 figure(3)
 subplot(2,1,1);
 plot(x,F,'b')%,peaked,Fp,'ro')
 set(gca,'XDir','reverse')
 set(gca,'XLim',[0,size(F,1)]);
 ylabel('Freeboard [m]')
 subplot(2,1,2);
 plot(x,PP,'b',x,y,'g')
```

```
set(gca,'XDir','reverse')
set(gca,'XLim',[0,size(F,1)]);
xlabel('Averaged Waveform Number')
ylabel('PP')
legend('PP','PP=1.8')


%*************************************************************************
% Calculate the Freeboard of the peaked signals
%*************************************************************************
peaked=[1338 1370 1402 1426 1598 1616 1633 1643];
peaked=peaked-a;

n=1;
for m=1:size(peaked,2)
      p=peaked(:,m);
      Fp(n,:)=F(p,:);
       n=n+1;
end

Fpmin=min(Fp)
Fpmean=mean(Fp);


%*************************************************************************
% The corrigated range
%*************************************************************************
% Find the diffuse waveforms
diffuse=find(PP<=1.8);
for n=1:size(diffuse,1)
      Fd(n,:)=F(diffuse(n,:),:);
      latd(n,:)=latitude(diffuse(n,:),:);
      lond(n,:)=longitude(diffuse(n,:),:);
end

Fd=Fd-Fpmin
Fdmean=mean(Fd)
Fp=Fp-Fpmin
Fpmean=mean(Fp)

z=repmat(0,[1 size(F,1)]);
figure(4)
plot(diffuse,Fd,'b+',peaked,Fp,'ro',x,z)
set(gca,'XDir','reverse')
set(gca,'XLim',[0,size(F,1)]);
ylabel('Freeboard [m]')


% Filters the diffuse freeboards to larger than zero
Fdgtno=find(Fd>0);
for n=1:size(Fdgtno,1)
      Fdgt(n,:)=Fd(Fdgtno(n,:),:);
end
Fdgtmean=mean(Fdgt)


% Convert the freeboard to thickness
R=4.89;
```

```
Td=(1+R)*Fdgtmean
Tp=(1+R)*Fpmean

%*************************************************************************
% Prints data to dat-file
%*************************************************************************
latlonp=[lonp latp];
latlonp=latlonp';
fid=fopen('latlonp11.dat','w');
fprintf(fid,'%2.6f\t %2.6f\n',latlonp);
fclose(fid);

latlond=[lond latd];
latlond=latlond';
fid=fopen('latlond11.dat','w');
fprintf(fid,'%2.6f\t %2.6f\n',latlond);
fclose(fid);


%*************************************************************************
function [data]=waveform(file_name)
%
% Read from the Scientific Data Set Waveforms
%*************************************************************************
data=hdfread(file_name,'data_blk_info.ave_ku_wvforms_if', 'Index', {[],[],[]});
%the brackets {start,stride,edge}
data=permute(data,[3 2 1]);
data=double(data);  %changes dataformat from uint16 to double
data=reshape(data,size(data,1),size(data,2)*size(data,3));


%*************************************************************************
function [Z]=plotwvf(data,a,i,b)
%
% Plots figure of entire dataset
%*************************************************************************
Z=data(:,a:i:b);

x=[1:size(Z,2)];
y=[1:size(Z,1)]';
[xx,yy]=meshgrid(x,y);

figure(2000)
 plot3(xx,yy,Z,'k');
view(-30,45)
set(gca,'YLim',[0,128]);
set(gca,'YTick',[0:16:128]);
set(gca,'XDir','reverse')
set(gca,'XLim',[0,size(Z,2)]);
xlabel('Averaged Waveform Number');
 ylabel('Gate Number');
 zlabel('Amplitude [FFT]');



%*************************************************************************
function [latitude,longitude,no]=position(file_name)
%
```

```
% Read from the Vdata RA2_DATA_SET_FOR_LEVEL_2 (dsr_time, latitude and longitude)
%*************************************************************************
% Reads subset of dataset (Record Index, dsr_time, latitude and longitude)
GDR_data=hdfread(file_name,'RA2_DATA_SET_FOR_LEVEL_2','Fields',{'Record
Index','dsr_time','lat','lon'});
%format long;    % displays 15 digits in the command window
record_index=GDR_data{1,1}';
record_index=double(record_index);
LAT=GDR_data{3,1}';
LAT=double(LAT);
LON=GDR_data{4,1}';
LON=double(LON);
dsr_time=GDR_data{2,1}';


dlat=hdfread(file_name,'hz18_diff_1hz_lat', 'Index', {[],[],[]}); %the brackets {start,stride,edge}
dlon=hdfread(file_name,'hz18_diff_1hz_long', 'Index', {[],[],[]}); %the brackets {start,stride,edge}

dlat=dlat';
dlat=double(dlat);      %changes dataformat from uint16 to double
dlat=dlat/100000;
dlon=dlon';
dlon=double(dlon);      %changes dataformat from uint16 to double
dlon=dlon/100000;

m=1;
for n=1:size(dlat,2)
      latitude(:,m)=LAT(n,1)+dlat(:,n);
      longitude(:,m)=LON(n,1)+dlon(:,n);
      m=m+1;
end

latitude=reshape(latitude,size(latitude,1)*size(latitude,2),1);
longitude=reshape(longitude,size(longitude,1)*size(longitude,2),1);
no=(1:size(latitude,1))';
latlonno=[no latitude longitude];
latlonno=latlonno';
fid=fopen('posno.dat','w');
fprintf(fid,'%4.0f\t %2.5f\t %2.5f\n',latlonno);
fclose(fid);

latlon=[longitude latitude];
latlon=latlon';
fid=fopen('pos.dat','w');
fprintf(fid,'%2.5f\t %2.5f\n',latlon);
fclose(fid);


%*************************************************************************
function [PP,pmax]=peakiness(data)
%
% Calculate the peakiness parameter (PP)
%*************************************************************************
pmax=max(data);
PP=(44.5*pmax)./sum(data(10:end,:));
pmax=pmax';
pmax_db=10*log10(pmax);
PP=PP';
```